Three dimensional light fields in atomic state interferometry

SPHINX JED SVENSSON

Master of Physics in Physics
with specialisation in quantum optics

Submitted in fulfilment of the requirements for the
Degree of Doctor of Philosophy in Physics

School of Physics and Astronomy
College of Science and Engineering
University of Glasgow

Deposited to the Library in August 2025

abstract

This thesis is about the interaction of structured light with atoms in the presence of external magnetic fields. Both light and atoms can carry phase dependent structures, the expression of which often depends on the choice of quantisation axis. The most general type of spatial structure light can have manifests as polarisation patterns. This type of structure is quantified as the optical concurrence. Although polarisations are usually considered to be two-dimensional, light can also carry a longitudinal polarisation component, but it has not been directly measured before.

Atomic states can be altered by external electric and magnetic fields. These fields don't just alter the atom's charge density distribution, but the very state space that defines it. Additionally, it is possible to redefine atomic states as superpositions of one another in order to reveal hidden structures. Previously, the best theoretical models of structured light-matter interaction were only valid for special cases, but a generalised model can open new opportunities for describing, understanding, and ultimately measuring ambient electric and magnetic fields.

In this thesis, the energy shifts induced in atoms by strong magnetic fields have been utilised to visualise an atomic transition normally unavailable in the chosen configuration being driven by longitudinal light. At the same time, a generalised model of the atomic state interferometer is constructed, and shown to be capable of predicting new ways to measure magnetic fields and optical concurrence.

The atomic state interferometer requires only a single transmission image for these measurements, and its validity means that it is possible to look for other combinations of electric and magnetic fields that can reveal further symmetries within the atom. In addition to having a highly versatile and customisable device that can measure the interplay of electric and magnetic fields, this thesis demonstrates a spatially resolved way of investigating three-dimensional polarisation states.

Having unlocked access to a new type of polarisation, the next steps are to investigate properties of strongly focused beams that have previously been confined to the realm of theory. On the more practical side, the atomic state interferometer lends itself to sensing applications, such as the measurement of non-classical correlations between degrees of freedom in a beam. Currently, work is being done to build a miniaturised research magnetometer based on the same principles.

In short, atoms provide a good interface between classical and quantum world. Customising their available state space opens the way to a new generation of sensors.

table of contents

TABLE OF CONTENTS

list of figures

acknowledgements

There are many people who I would like to thank for getting me where I am.

First of all: Sonja Franke-Arnold, my primary supervisor and mentor, brilliant physicist and excellent teacher. Without you, none of this would have happened, and my life would be much worse for it.

Then Nic, my key collaborator and second supervisor. Both of you have probably shown me more patience than I deserve.

The coworkers who taught me and the coworkers I taught in turn: Jinwen Wang, Amy McWilliam, Claire Cisowski, Mustafa Al Khafaji, Kuntal Samanta, and Richard Aguiar Maduro.

My collaborators from all over the world (and in the building): Ifan Hughes, Danielle Pizzey, Clare Higgins, Zhujun Ye, Sebastiao Padua, and Sarah Croke.

My dear friends who kindly offered to proofread my thesis (some of whom even made good on it): Kieran Roberts, Abigail Thom, and Tom Smith.

And finally, my predecessors whose theseses were invaluable points of reference all throughout my PhD: Adam Selyem and Tom Clark.

I never know how to say these things. Thank you alll so much for your help and support.

LIST OF FIGURES

publications

available to read

Measuring the Optical Concurrence of Vector Beams with an Atomic-State Interferometer [1]

JINWEN WANG, SPHINX J. SVENSSON, THOMAS W. CLARK, CHEN YUN, MUSTAFA A. AL KHAFAJI, HONG GAO, NICLAS WESTERBERG AND SONJA FRANKE-ARNOLD

Physical Review Letters, May 2024

THIS PAPER SHOWED THE SINGLE SHOT MEASUREMENT OF OPTICAL CONCURRENCE USING AN ULTRACOLD ATOMIC STATE INTERFEROMETER. CONCURRENCE IS FIRST INTRODUCED IN CHAPTER 2.2.1, THE EXPERIMENTAL BACKGROUND IS DISCUSSED IN CHAPTER 7.3, AND THE PAPER'S FINDINGS ARE DISCUSSED IN CHAPTER 8.2.

Dynamic Mueller matrix polarimetry using generalized measurements [2]

AMY MCWILLIAM, MUSTAFA A. AL KHAFAJI, SPHINX J. SVENSSON, SEBASTIAO PÁDUA AND SONJA FRANKE-ARNOLD

Optics Express, May 2024

IN THIS PAPER, A MODIFIED SAGNAC INTERFEROMETER WAS USED IN ORDER TO MEASURE THE THE CHANGE IN A VECTOR BEAM INDUCED BY AN OPTICAL ELEMENT, AND CALCULATE ITS MUELLER MATRIX. THE FINDINGS OF THIS PAPER ARE THE SUBJECT OF CHAPTER 4.

Spatially-dependent dark states in cold atomic vapours

SPHINX J. SVENSSON, NICLAS WESTERBERG, KUNTAL SAMANTA AND SONJA FRANKE-ARNOLD

Conference: Complex Light and Optical Forces XVIII, March 2024

THIS CONFERENCE PAPER SHOWED PRELIMINARY RESULTS IN THE DEVELOPMENT OF A NEW THEORETICAL MODEL OF THE ATOMIC STATE INTERFEROMETER USING

PARTIALLY DRESSED STATES. AN UPDATED VERSION OF THE MODEL CAN BE FOUND IN CHAPTER 6.3.2.

as yet unpublished

Visualizing strongly focused 3D light fields in an atomic vapor [3]

SPHINX J. SVENSSON, CLARE R. HIGGINS, DANIELLE PIZZEY, IFAN G. HUGHES AND SONJA FRANKE-ARNOLD

Final editing stages.

THIS PAPER IS ABOUT THE FIRST EVER DIRECT MEASUREMENT OF THE LONGITUDINAL COMPONENT OF STRONGLY FOCUSSED LIGHT. IT USES ABSORPTION SPECTROSCOPY IN THE HYPERFINE PASCHEN-BACK REGIME (SEE CHAPTER 6.2) TO DRIVE A TRANSITION OTHERWISE UNAVAILABLE IN THE CHOSEN CONFIGURATION. THE FINDINGS ARE DISCUSSED IN DETAIL IN CHAPTER 9.

Atomic state interferometers for vector light

KUNTAL SAMANTA*, SPHINX J. SVENSSON*, NICLAS WESTERBERG AND SONJA FRANKE-ARNOLD

Writing stage. * these authors contributed equally.

THIS PAPER IS ABOUT THE FINAL GENERALISED PARTIALLY DRESSED STATE MODEL OF THE ATOMIC STATE INTERFEROMETER. THE MODEL IS FULLY DERIVED IN CHAPTER 6.3.2

.

declaration of the author

All work described in this thesis was done as part of my PhD under the supervision of Professor Sonja Franke-Arnold at School of Physics and Astronomy of the University of Glasgow. The work began in October 2021 and finished in April 2025.

I hereby declare that the work in this thesis is entirely my own, except where specific references are made. I have not submitted it in part or whole to any other university for a degree, nor do I intend to.

Author's Signature:

Sphinx J. Svensson
22/04/2025

DECLARATION

introduction

"How come everything is the way it is and not entirely different?"
-"You'd like that, wouldn't you. Have you washed your ears?"
- Tove Jansson

One of the most perplexing discoveries during the quantum revolution is that two orthogonal states can be in a superposition of one another, and that the resulting state is just as valid a state as its components. As a necessary consequence, this means that projective measurements determine how the processes within the system present - two effects thought to be distinct can turn out to be one and the same.

Any system with multiple orthogonal states can be mapped onto a state space with one state per axis. In the same way that a coordinate rotation is valid in any coordinate system, the geometry of a state space can be redefined to simplify the mathematical model or highlight a certain effect. This is called a dressed state picture, and highly useful in systems that show wavelike behaviour, as a basis change can help understand phase dependent behaviour. These states can exist in a variety of degrees of freedom, in the case of light this could be spatial position along the propagation axis, position in the tranverse plane, intensity, phase, or polarisation, to name a few. Two or more degrees of freedom can be correlated in order to give the beam a structure. The structure of light can be altered by optical elements, which can be mathematically described by Jones or Mueller matrices. Within the beam, the correlation of polarisation and position in the transverse plane is quantified as optical concurrence [4]. Elusive concepts like it often require interferometric or tomographical approaches to measurement using conventional detectors. Another effect that has gotten less attention than it deserves due to its inability to be measured directly by conventional detectors is the existence of longitudinally polarised light [5]. It is in situations like this that atom optics comes to shine.

Atoms provide an intuitive and natural interface between classical and quantum mechanics, to the extent that many university courses about "quantum physics" are specifically about semiclassical atom optics - this is how I got here. In the semiclassical limit, the wave is treated as a classical wave, while the atom is treated as a fully quantised object. This model is highly successful, and well suited for being experimentally tested. In the dipole approximation, the light is modelled as an oscillating electric field. Atoms are highly susceptible to external electric and magnetic fields (which themselves, too, are different presentations of the same effect). It is due to all these factors that atoms are so commonly used in detectors, such as atomic clocks [6], accelerometers [7], gyroscopes [8], gravimeters [9], and, of course, magnetometers [10]. But these are just the commercial applications, and as such only scratches

the surface of research in atom optics.

Sonja Franke-Arnold's lab at the University of Glasgow has long been investigating these types of properties. It was here that spatially dependent electromagnetically induced transparency was first shown [11], and in 2021, a new type of atomic magnetometer based on atom state interferometry was demonstrated [12]. Meanwhile, research was being done into the topological structure of beams [13] such as concurrence [14].

I started my PhD in October of 2021, disorganised and naive and bright eyed and excited to become a physicist. The project I had signed up for was to take over the cold atom experiment on which the atomic state interferometry was being investigated from Jinwen Wang. While the overlap period between students on this complicated experiment is normally close to half a PhD, mine was tragically cut short due to buerocratic reasons, and we only had time to collect a few sets of data before he left the country. While trying to catch up with teaching myself the technical details between lectures and progress reviews, I began work with Amy McWilliam on some side projects, one of which resulted in a new technique for single shot measurement of Mueller matrices homogeneous optical elements [2].

Part I of this thesis is all about structured light. In chapter 1, different notations of polarisation are introduced, alongside a discussion of each of their benefits for different situations. In chapter 2, different structures of beam are introduced. The transverse intensity distribution of a beam can change upon propagation, if it doesn't, the beam is considered to be an eigenmode of propagation. Superpositions of two or more such beams with the same polarisation can result in another eigenmode of propagation, superpositions of such beams with different polarisations can lead to the creation of a beam with a spatially dependent polarisation profile. If a beam is focused by a lens, it can obtain a longitudinal component. This is the subject of chapter 3, where the existence of such a component is mathematically derived. Finally, in chapter 4, it is shown that positive operator valued measurements (POVMs) can be applied to polarisation. The chapter culminates in my and Amy's findings regarding Mueller matrices using this method.

It is very easy for me to get side tracked, and as such I took on more side projects than I probably should have. Some of them lead nowhere, such as a proof of concept for using rotationally invariant vector beams as a basis for quantum communication, but others became integral parts of my research. One of these projects involved the creation of an improved theoretical model of the atomic state interferometer.

Part II of this thesis is about the underlying principles of the atom. Chapter 5 builds up a model of the atom starting from the definition of quantum numbers, and chapter 6 explains how the atom is changed by an external magnetic field. From there, a Hamiltonian operator describing the energies and hopping rates of the $F = 1 \rightarrow F' = 0$ transition of the D2 line of Rb-87, and how, with the correct choice of parameters, the atom can become locked into a single dark state.

As my understanding of the atomic state space grew, so did my skills as an experimentalist. My confidence grew, I started speaking at conferences, contributing to papers, helped with the training of new PhD students, and took on yet another experiment, one which would grow to become my main project. In a collaborative effort with the University of Durham, we were going to use atoms in a strong magnetic field in order to first directly measure the longitudinal component of light [3]. I remember the day our collaborators showed up to deliver parts of the experimental setup, including a 1.6 T permanent magnet (this reminds me, I still have to demagnetise my favourite

screw driver). Once again thrown in the deep end, I was better prepared this time, and began gathering data in such volumes that I had to cut multiple sections from this thesis because there wasn't enough time to properly analyse it all.

Part III of this thesis is dedicated to experimental atom optics. Chapter 7 is in essence an extended method section for the cold atom experiment, going over all the necessary key components to maintain the spontaneous force dark optical trap (SpOT) at the centre of the setup, and how experiments are run on it. Chapter 8 is about the data gathered using this experiment, especially in the context of the new model. It is in this chapter that the data I gathered with Jinwen can be found, when we measured the concurrence of a vector beam with a single transmission image [1]. However, my most important contribution to the field is found in chapter 9, where the method and data regarding the measurement of longitudinal polarisation is located.

It is in this part of the thesis that the heart of the thesis is located. I am, at my core, an experimental atomic physicist, and my thesis reflects that. There are multiple purposes that my writing here is meant to fulfill: First and formost, of course, it is intended to get me a doctorate (fingers crossed), but in the Optics group, it has become something of a tradition to use the theses of former students as textbooks for the next generations, so: Hi future student! I hope this work helps you.

I

a really long preface about light

Light has been central to physical research since the beginning, when it was still called natural philosophy. Records and archeological finds document the use of mirrors made from polished metal as early as 1900 BCE. Many of the philosophers in ancient Greece developed theories surrounding refraction, which they observed by filling glass vessels with water. At the time, it was thought that people emitted light from their eyes, and then interacted with a secondary source, such as fire or the sun, enabling sight [15]. This time period marks the popularisation of "burning glasses", focusing lenses used to start fires.

The Islamic golden age saw some major advances in the study of reflection and refraction, often with a focus on curved surfaces. One particular Scholar of note is Abu Sa'd al-'Ala Ibn Sahl, whose teachings, once translated into Latin, were instrumental in Europe's "rediscovery of Science" during the later middle ages, and lead to the invention of corrective lenses. The renaissance period was, too, a renaissance of the sciences. It was an age defined by polymaths, most of which, like Leonardo da Vinci, also dabbled in optics. Arguably, the biggest leap made during this time period was the shift from geocentricism to heliocentricism. This level of astronomy was of course made possible through the progress made in optics that enabled the invention of the telescope, as well as the microscope. In the following century, the law of refraction was finally centralised by W. Snell and R. Descartes. It was on the shoulders of these giants that I. Newton first demonstrated the splitting of white light into a spectrum of different colours [16].

Electromagnetism, previously considered entirely separate, was forever linked to optics when M. Faraday showed the effect of magnetic fields on polarisation (spoilers for chapter 6.1). This allowed J.C. Maxwell to centralise all behaviour of electromagnetic forces in just four equations. The big question at the time was whether light is a wave or a particle, with Newton being a staunch believer of the particle hypothesis. The definite proof that light travels in waves came from Young's double slit experiment, and the medium of said wave was thought to be the luminiferous ether. Finding out that it instead travels through space itself in the Michelson-Morley experiment directly lead to the discovery of the theory of relativity. Around the same time, the discovery of wave-particle duality lead to the birth of quantum mechanics.

Modern physics is still permeated by the study of light. Quantum optics, photonics, quantum information theory and quantum electrodynamics are all vast fields that lead to groundbreaking revelations on a regular basis. Light enables global communications, and is used in the definition of multiple SI units, most famously in the redefinition of the second using the caesium atomic clock.

While this thesis is primarily in the subject of atomic physics, it is clear that one must understand light in order to understand atoms. Therefore, let us begin with the fundamentals.

1 light as a wave

Light is famous for its wave-particle duality. It acts like a point particle when interacting with non-photon particles, like being absorbed or emitted, but when it propagates it acts like a wave and interferes with itself. A laser emits a beam of many identical photons, which preserves their wavelike nature, though interaction and therefore measurement are now classical as the amplitude can be reduced by arbitrary amounts. Laser light is of a single frequency. The uncertainty principle, and the nature of the Fourier transform, dictate that the wave extends infinitely along the propagation direction in both space and time.

For simplicity, light is often considered to be travelling in free space, i.e. a vacuum free of any ambient charges. Under these circumstances, **Maxwell's equations** can be written as [17]:

$$\nabla \cdot \vec{E} = 0 \tag{1.1}$$

$$\nabla \cdot \vec{B} = 0 \tag{1.2}$$

$$\nabla \times \vec{E} = -\frac{\partial \vec{B}}{\partial t} \tag{1.3}$$

$$\nabla \times \vec{B} = \mu_0 \varepsilon_0 \frac{\partial \vec{E}}{\partial t}, \tag{1.4}$$

where $\vec{E}$ is the electric field, $\vec{B}$ the magnetic field, and μ_0 and ε_0 are the permeability and permittivity of free space, respectively.

The propagation of light is a direct consequence of Maxwell's equation. Under the constraints mentioned earlier, the curl of equation 1.3 can be combined with equation 1.4 to yield a solution that describes a wave in the electric field [16]:

$$\nabla^2 \vec{E} - \frac{1}{c^2} \frac{\partial^2 \vec{E}}{\partial^2 t} = 0 \tag{1.5}$$

The time is t and the speed of light is $c = \frac{1}{\sqrt{\varepsilon_0 \mu_0}}$. This equation relates the temporal and spatial distributions of the electric field. The wave equation for a magnetic field strength $\vec{H}$ is derived alongside it, and very similar:

$$\nabla^2 \vec{H} - \frac{1}{c^2} \frac{\partial^2 \vec{H}}{\partial^2 t} = 0. \tag{1.6}$$

Its interpretation shows that, like the electric field, its temporal and spatial distributions are related.

A change in the electric field induces a magnetic field, and vice versa. An oscillation, a blip, a perturbation in the electric field will therefore induce a similar such peak in its orthogonal direction, which will in turn induce an electric field in the opposite direction to the first one - now the electric field, and therefore the magnetic field, is oscillating. Due to the spatiotemporal relation, this electromagnetic wave propagates in space! The solution of the above equations for a sinusoidal wave is known as the **plane wave equation**:

$$\vec{E}(\vec{r},t) = E(\vec{r})e^{i\phi(\vec{r},t)}\hat{e}(\vec{r}) \tag{1.7}$$

with the phase ϕ being defined as

$$\phi(\vec{r},t) = \vec{k}\cdot\vec{r} - \omega t + \phi_0(\vec{r}). \tag{1.8}$$

In the above equations, $\vec{r} = (x, y, z)$ is the three dimensional spatial coordinate. The phase can have an offset ϕ_0. The parameter $\hat{e}$ defines the direction of oscillation, or polarisation. The wave vector $\vec{k}$ depends on the wave number $k = \omega/c = 2\pi/\lambda$ and hence the wavelength λ. It points perpendicularly to the planes of equal phase, and ω is the angular frequency. Those final two parameters are related:

$$\left|\vec{k}\right| = \frac{\omega}{c} = \frac{2\pi}{\lambda} \tag{1.9}$$

For any given single optical frequency, a time independent version of the wave equation can be derived by substituting the plain wave equation into it. This form is known as the Helmholtz equation, and highlights the relationship of the wavevector to the electric field's gradient in an eigenvalue equation:

$$\nabla^2\vec{E}(\vec{r}) + k^2\vec{E}(\vec{r}) = 0 \tag{1.10}$$

This becomes even simpler if the electric field is only considered in one direction, making it a scalar rather than a vector:

$$(\nabla^2 + k^2)E(\vec{r}) = 0. \tag{1.11}$$

This form makes it possible to consider a beam of light with multiple frequencies and polarisations as the sum of its parts without losing generality or other information:

$$\vec{E}(z,t) = \sum_j E_{0j}(z)\exp[i(kz - \omega t + \phi_{0j}]\hat{e}_j, \tag{1.12}$$

where we are summing over the components j. Interference effects will become apparent once this sum is calculated.

When a photon is absorbed, the transition probability does not happen with its electric field but rather the electric field's magnitude squared, i.e the intensity I:

$$I = |E|^2. \tag{1.13}$$

This is not only relevant when studying light matter interaction, but also for the detection of the light itself - when a camera or photodiode or equivalent detects a

photon all phase and polarisation information is lost. This needs to be taken into account and sometimes worked around.

Orthogonal polarisations do not interfere but they do superpose. The relative phase is highly relevant for this. Multiple different notations have been developed in order to highlight different aspects of this. This chapter is intended to provide an overview of these different polarisation notations, as well as an intuitive and complete explanation of polarisation in classical optics.

1.1 polarised light

IN WHICH WE LAY THE GROUNDWORK FOR DISCUSSING POLARISATION

Light as described by the wave equation is transverse wave, which means its electric field oscillates in a direction that is perpendicular to the one it travels in (an oversimplification we will come to regret in chapter 3). This makes it a two dimensional object. Space, however, is three dimensional - for every given direction of propagation there are two possible orthogonal directions of oscillation, and all other polarisations can be expressed as a superposition of those two base polarisation states, and each of these states has a phase associated with it [18]. A commonly chosen basis of states is "horizontal" and "vertical", or $|H\rangle$ and $|V\rangle$, respectively.

The Dirac notation used throughout this thesis is borrowed from quantum mechanics, as all light considered here is classical. It is being used as a stand-in for the unit vectors here, in part to highlight the superposing nature of light, and in part for better compatibility once other, more quantum concepts are introduced.

Now, consider the wave equation for a single wavelength of light with an arbitrary polarisation, expressed in its horizontal and vertical components at a single point in space and time:

$$|E\rangle = E_{0,H} e^{i\phi_H} |H\rangle + E_{0,V} e^{i\phi_V} |V\rangle \,, \tag{1.14}$$

where $E_{0,H}$ and $E_{0,V}$ are the amplitudes of the horizontal and vertical polarisation states, and ϕ_H and ϕ_V are their respective phases.

The relative amplitude and phase of the components determine the final polarisation. If, say, $E_{0,H} = 0$ and $E_{0,V} = 1$, the beam is vertically polarised. If both components have the same amplitude, the relative phase becomes the sole determining factor: Figure 1.1 visualises that a phase difference $\delta\phi = \phi_V - \phi_H = 0$ leads to diagonally polarised light ($|D\rangle$) and a phase of $\pm\pi$ leads to antidiagonally polarised light ($|A\rangle$) [19]:

$$\frac{1}{\sqrt{2}} e^{i0} |H\rangle + \frac{1}{\sqrt{2}} e^{i0} |V\rangle = |D\rangle \tag{1.15}$$

$$\frac{1}{\sqrt{2}} e^{i0} |H\rangle + \frac{1}{\sqrt{2}} e^{i\pi} |V\rangle = |A\rangle \,. \tag{1.16}$$

However, these two phases present a special case where the peaks and troughs of both waves perfectly align. Other equal superpositions of horizontally and vertically polarised light will no longer result in linear polarisations.

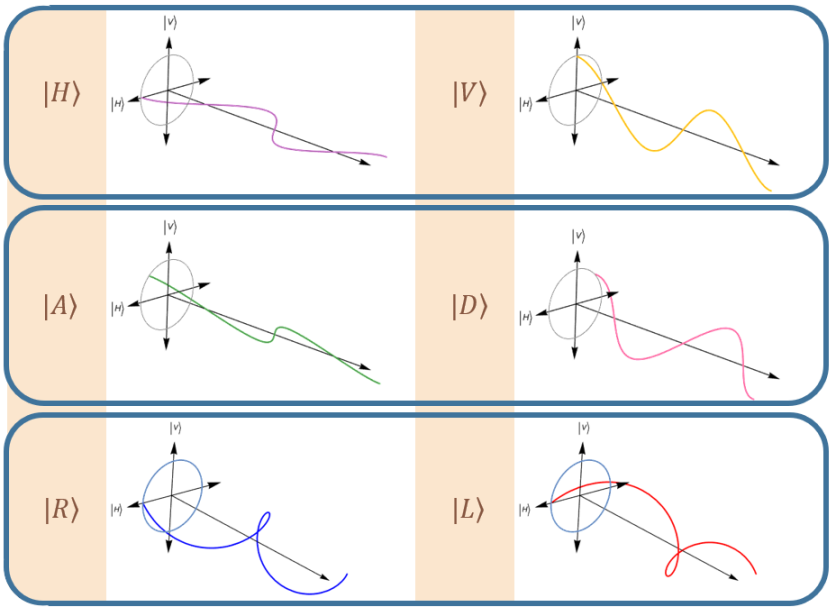

Figure 1.1: Three mutually unbiased sets of orthogonal polarisation basis states. Each set can be expressed in terms of an equal superposition between any other. This specific set of states is known as the Stokes basis states for reasons that will become apparent in chapter 1.4

1.1.1 circular polarisations and spin

Consider the beam from equation 1.14 with equal horizontal and vertical components, $E_{0,H} = E_{0,V}$ but with a relative phase of $\pm\frac{\pi}{2}$. Whenever one polarisation component reaches its maximum/minimum, the other goes to 0. This causes the electric and magnetic fields to take on a spiral structure as they propagate. A phase of $-\frac{\pi}{2}$ results in **"right-handed" polarisation** ($|R\rangle$), and a phase of $\frac{\pi}{2}$ in **"left-handed" polarisation** ($|L\rangle$) (see figure 1.1), so named after the curl of the fingers of the respective hand if the thumb points towards the light source.

$$\frac{1}{\sqrt{2}}e^{i0}\,|H\rangle + \frac{1}{\sqrt{2}}e^{-i\pi/2}\,|V\rangle = |R\rangle \tag{1.17}$$

$$\frac{1}{\sqrt{2}}e^{i0}\,|H\rangle + \frac{1}{\sqrt{2}}e^{+i\pi/2}\,|V\rangle = |L\rangle\,. \tag{1.18}$$

By definition, anything with a time dependent circular path carries angular momentum. Therefore, all circularly polarised light has an associated angular momentum as an intrinsic property of its spiralling magnetic field. In contrast to extrinsic angular momentum, which is further discussed in chapter 2.1.3, this is spin angular momentum (SAM), which is an inherent property of the photon, and is transferred when the photon is absorbed. Photons are bosonic, which means they carry integer spin. When projected onto the propagation axis, it is referred to as the photon's

helicity: $-\hbar$ for $|R\rangle$ and $+\hbar$ for $|L\rangle$ [20].

Of course, the direction of rotation in real space is just as important: A right circularly polarised beam propagating in the $+\hat{z}$ direction is, in the lab frame, rotating in the same direction as a left circularly polarised beam travelling in the $-\hat{z}$ direction. This concept is known as the photon's chirality.

The same way circular polarisations can be formed from phase shifted superpositions between the linear $|H\rangle$ and $|V\rangle$ basis states, superimposing equal and orthogonal, i.e. counter rotating, circularly polarised photons, will always lead to constructive interference along one linear axis and destructive interference along the other. This results in a linear polarisation, but its orientation depends on the relative phase between the circular components. Expressing all the concepts described by this with equation 1.14 will become very long very fast, so it is time to introduce some alternative notations.

1.2 Jones calculus

IN WHICH JONES VECTORS AND MATRICES ARE INTRODUCED

In equation 1.14, the beam is expressed in the orthogonal polarisation components $|H\rangle$ and $|V\rangle$. The total amplitude is often externalised, as the polarisation information is contained in the relative amplitude and phase, like in equation 1.7. Another more compact way to express the information contained therein is by using the 2-dimensional **Jones vector**:

$$\vec{E} = \begin{pmatrix} \tilde{E}_x \\ \tilde{E}_y \end{pmatrix} = \begin{pmatrix} E_{0x} e^{i\phi_x} \\ E_{0y} e^{i\phi_y} \end{pmatrix}. \tag{1.19}$$

This notation was developed in 1941 by R.C. Jones [21]. It is optimised for describing fully polarised and coherent light, and enables changes to the field to be written as matrix multiplications. Conventionally, the two orthogonal basis states are horizontal and vertical polarisations, but a selection of alternative basis choices is explored later, in chapter 1.5.1.

It is now possible to externalise global phase. This further simplifies the notation of beam propagation by separating the time dependent phase term into a global and relative component:

$$\begin{pmatrix} E_x(t) \\ E_y(t) \end{pmatrix} = \begin{pmatrix} E_{x0} e^{i(kz-\omega t+\phi_x)} \\ E_{y0} e^{i(kz-\omega t+\phi_y)} \end{pmatrix} = \begin{pmatrix} E_{x0} e^{i\phi_x} \\ E_{y0} e^{i\phi_y} \end{pmatrix} e^{i(kz-\omega t)}. \tag{1.20}$$

Global phase is generally not measurable (definitions may vary with circumstances) and can be safely discarded within the context of this thesis. As we have externalised spatiotemporal propagation effects as a global phase, this simplifies the Jones vector:

$$\vec{E} = \begin{pmatrix} E_{0x} \\ E_{0y} e^{i\Delta\phi} \end{pmatrix}. \tag{1.21}$$

This form of the Jones vector is what will be most commonly used from this point onward. It is now useful to revisit some concepts introduced in chapter 1.1:

To start, when calculating intensity from the Jones vector, both polarisation components need to be taken into account, so :

$$I = (E_x^*, E_y^*) \begin{pmatrix} E_x \\ E_y \end{pmatrix} \tag{1.22}$$

$$= |E_x|^2 + |E_y|^2. \tag{1.23}$$

In this equation we have taken $E_{x,y}$ to be complex numbers, containing both amplitude and relative phase. This is true regardless of basis state.

All polarisations shown earlier in figure 1.1 can be expressed in the form of a Jones vector:

$$|H\rangle = \begin{pmatrix} 1 \\ 0 \end{pmatrix} \qquad |V\rangle = \begin{pmatrix} 0 \\ 1 \end{pmatrix} \tag{1.24}$$

$$|A\rangle = \frac{1}{\sqrt{2}} \begin{pmatrix} 1 \\ -1 \end{pmatrix} \qquad |D\rangle = \frac{1}{\sqrt{2}} \begin{pmatrix} 1 \\ 1 \end{pmatrix} \tag{1.25}$$

$$|R\rangle = \frac{1}{\sqrt{2}} \begin{pmatrix} 1 \\ -i \end{pmatrix} \qquad |L\rangle = \frac{1}{\sqrt{2}} \begin{pmatrix} 1 \\ i \end{pmatrix}. \tag{1.26}$$

Here, any overall amplitude and phase are omitted - the normalised Jones vectors shown are analogous to unit vectors.

This octahedron of polarisations, three equally spaced and equally balanced orthogonal pairs of superpositions to one another, are central to the way optics is practised, and will come back quite a few times in this thesis - most notably in chapter 1.4, but also in chapter 2.3, when it is revealed that these states lay the basis of the most common form of polarimetry.

1.2.1 Jones matrices

Polarisation can be altered by **optical elements**. This process can be simulated on the Jones vector by the use of complex 2x2 matrices. These **Jones matrices** act on the relative amplitude and phase of each polarisation component [22]:

$$\begin{pmatrix} E_x \\ E_y \end{pmatrix} = \begin{pmatrix} J_{11} & J_{12} \\ J_{21} & J_{22} \end{pmatrix} \begin{pmatrix} E_{x0} \\ E_{y0} \end{pmatrix}. \tag{1.27}$$

The diagonal elements J_{11} and J_{22} conserve parts of the polarisation in each basis state, though potentially with an added phase shift, whereas the off-diagonal elements J_{21} and J_{12} partially or fully shift one of the polarisation components to the other, also potentially with an added phase. Let's consider a few examples.

Birefringent media have refractive indexes along different directions - the ordinary refractive index n_o and the extraordinary refractive index n_e. The direction of the extraordinary refractive index is called the fast axis. Light polarised along the fast axis will emerge with a different phase shift to light along the slow axis. As all

polarised light can be expressed in orthogonal linear bases, birefringent media can alter the polarisation of a beam.

Linear wave retarders are birefringent optical devices used to alter the polarisation of a beam without affecting its shape or path. They are commonly made from quartz, and wavelength specific (though there are broad spectrum equivalents, e.g. Fresnel rhombs). As a general rule, these wave plates have two key parameters: Fast axis angle, and relative phase shift. In most cases, the devices are manufactured so that the phase shift corresponds to a particular fraction of the wavelength, e.g. $\frac{\lambda}{2}$ or $\frac{\lambda}{4}$.

A **quarter wave plate** (QWP), sometimes also referred to as a $\frac{\lambda}{4}$-plate is a linearly birefringent optical device that induces a phase shift of $\frac{\pi}{2}$ between two orthogonal polarisation bases [23]. Its Jones matrix is

$$\hat{J}_{\mathrm{QWP}} = \begin{pmatrix} \cos^2\theta + i\sin^2\theta & (1-i)\sin\theta\cos\theta \\ (1-i)\sin\theta\cos\theta & i\cos^2\theta + \sin^2\theta \end{pmatrix}, \tag{1.28}$$

where θ is the angle of the fast axis. If the axis is horizontal or vertical, the expression simplifies:

$$\hat{J}_{\text{QWP, horizontal}} = \begin{pmatrix} 1 & 0 \\ 0 & i \end{pmatrix} \tag{1.29}$$

$$\hat{J}_{\text{QWP, vertical}} = \begin{pmatrix} 1 & 0 \\ 0 & -i \end{pmatrix}. \tag{1.30}$$

A **half wave plate** (HWP), or $\frac{\lambda}{2}$ plate, similarly induces a phase shift of π between the orthogonal linear polarisation components:

$$\hat{J}_{\mathrm{HWP}} = \begin{pmatrix} \cos 2\theta & \sin 2\theta \\ \sin 2\theta & -\cos 2\theta \end{pmatrix}. \tag{1.31}$$

This equation is significantly simpler than that of a QWP, and its solution for different fast axis angles trivial, and therefore omitted.

However, not all optical elements are uniform: A **q-plate**, for example, is a liquid crystal device that acts like a HWP with a spatially dependent fast axis in azimuthal periodicity. It is characterised by its topological charge number m [24, 25]:

$$\hat{J}_{\mathrm{qp}}(m) = \begin{pmatrix} \cos(2m\theta) & \sin(2m\theta) \\ \sin(2m\theta) & -\cos(2m\theta) \end{pmatrix}. \tag{1.32}$$

The topological charge of the q-plate can be inverted by rotating the component in the setup. The full effect of a q-plate on the beam is discussed in chapter 2.2.

Phase plates are by far not the only optical element that can be described by a Jones matrix. Another commonly used optical component is the **polariser**, which projects the beam into a single polarisation state. A linear polariser once again has a rotation angle θ which is aligned with the electric field of the linear polarisation that can pass through [17]

$$\hat{J}_{\mathsf{LP}} = \begin{pmatrix} \cos^2\theta & \cos\theta\sin\theta \\ \cos\theta\sin\theta & \sin^2\theta \end{pmatrix}. \tag{1.33}$$

Even a **mirror** is an optical element, and can be described by a Jones matrix. In fact, there is quite a lot of literature about them (sources). For the purpose of this thesis, the following approximations are made: There are only perfect mirrors, which are perfectly vertical in the lab frame, i.e. with a tilt confined to the horizontal axis. Such a mirror's Jones matrix is simplified to its base components:

$$\hat{J}_{\mathsf{mirror}} = \begin{pmatrix} -1 & 0 \\ 0 & 1 \end{pmatrix}. \tag{1.34}$$

Note that even a perfect mirror alters the polarisation: all superpositions of $|H\rangle$ and $|V\rangle$ stay the same in the lab frame, and are therefore flipped in the frame of the propagation axis, e.g. $|R\rangle$ becomes $|L\rangle$, and $|D\rangle$ becomes $|A\rangle$.

Of course, it is unrealistic to achieve perfect alignment like this, and even small uncertainties can quickly add up. Real mirrors often also absorb small parts of the beam, and can induce small phase shifts. The material and coating of the mirror should be considered carefully when building an experimental setup [17].

Not all optical elements work in the linear basis, **optical rotators**, for example, are circularly birefringent [23] (a concept that is discussed in detail in chapter 5.2.2) and can be expressed as

$$\hat{J}_{\mathsf{rot}}(\theta) = \begin{pmatrix} \cos\theta & \sin\theta \\ -\sin\theta & \cos\theta \end{pmatrix}. \tag{1.35}$$

This type of component acts on the chirality of the beam, rather than its helicity. This means that it isn't unitary, which makes it the basis of the Faraday isolator: if the beam is rotated 45° from $|V\rangle$ to $|A\rangle$ and then reflected straight back, it will rotate a further 45° to $|H\rangle$. If now a $|V\rangle$ selective polariser is placed in front of the rotator, and one for $|A\rangle$ after, then all light is blocked from returning to the source. Series of optical components like this can be described by multiplying all Jones matrices by the initial polarisation in reverse order, making it possible to describe a larger optical system or even an entire experiment in a single matrix:

$$\vec{E}_{\mathsf{out}} = \hat{J}_n \hat{J}_{n-1} ... \hat{J}_2 \hat{J}_1 \vec{E}_{\mathsf{in}}. \tag{1.36}$$

This section has so far ignored all global phase shifts. It is possible to induce a global phase shift without altering the polarisation or beam path by inserting a slide of glass or monorefringent quartz. This is sometimes used in interferometry, as demonstrated later, in chapter 4.

Jones calculus is very useful for expressing all information relating to the polarisation in one small vector, but it does not relate very well to measurement. All measurement is inherently projective (see chapter 4), which means the phase information is lost. As will be found in chapter 2.3, full tomography can not be done with just one set of orthogonal basis states. In order to fully reconstruct the polarisation, additional measurements have to be performed - enough to define the polarisation state space.

1.3 the Poincaré sphere and the polarisation ellipse

IN WHICH THE POINCARÉ SPHERE AND THE POLARISATION ELLIPSE NOTATION ARE INTRODUCED

So far in this chapter, the focus has been on three pairs of orthogonal polarisation states: $|H\rangle$ and $|V\rangle$, $|A\rangle$ and $|D\rangle$, $|R\rangle$ and $|L\rangle$. Each of these pairs is a set of mutually unbiased basis, and can be expressed as an equal superposition of any other pair. This means any state has the same overlap with any state from another pair. In the Jones basis in particular, it becomes intuitive to picture $|A\rangle$, $|D\rangle$, $|R\rangle$ and $|L\rangle$ as four points on a circle of all possible equal superpositions of $|H\rangle$ and $|V\rangle$. In fact, this can be generalised even further: for a beam of a given intensity, here normalised to 1, the relative electric field amplitudes, too can be expressed as an angle. In other words, any given polarisation state can be expressed as a point on the surface of a sphere.

Another way to picture this is that the three sets of basis states form a three dimensional coordinate system. Any polarised state can now be pictured as a vector from the origin with a fixed radius given by the intensity. All possible angles of this vector once again form the surface of a sphere - the **Poincaré sphere** [26].

It makes sense to consider the Poincaré sphere in polar spherical coordinates: the ellipticity angle χ and the orientation angle ψ. Figure 1.2 shows that the equator is formed of the linear polarisations, while the circular polarisations form the poles. In this notation, the six Stokes basis states can be expressed like this [27]:

$$E_{0,H} - E_{0,V} = E_0 \times \sin 2\chi \cos 2\psi \tag{1.37}$$
$$E_{0,D} - E_{0,A} = E_0 \times \sin 2\chi \sin 2\psi \tag{1.38}$$
$$E_{0,R} - E_{0,L} = E_0 \times \cos 2\chi. \tag{1.39}$$

This is a direct consequence of the orthogonal components sitting on opposite axes of the Poincaré sphere. This property forms the basis of the Stokes notation introduced in chapter 1.4, but the angles also relate to the polarisation in a much more direct way.

1.3.1 the polarisation ellipse

When re-expressed in spherical coordinates, the position on the Poincaré sphere directly gives information about the polarisation ellipse: We assume $|H\rangle$ as the initial position for the inclination, and $|R\rangle$ to be the initial ellipticity.

As a general statement, any polarisation state takes the form of an ellipse, characterised by **orientation** and **ellipticity**. Linear and circular polarisations are special cases of this - in all linear polarisations have 0 ellipticity and are entirely described by their orientation, whereas circular polarisation states are rotationally invariant, and described entirely by their ellipticity. Figure 1.3 demonstrates that these two parameters directly correspond to the angles on the Poincaré sphere. The angles on the Poincaré sphere are doubled because adding π to either angle simply results in the same polarisation with a phase shift.

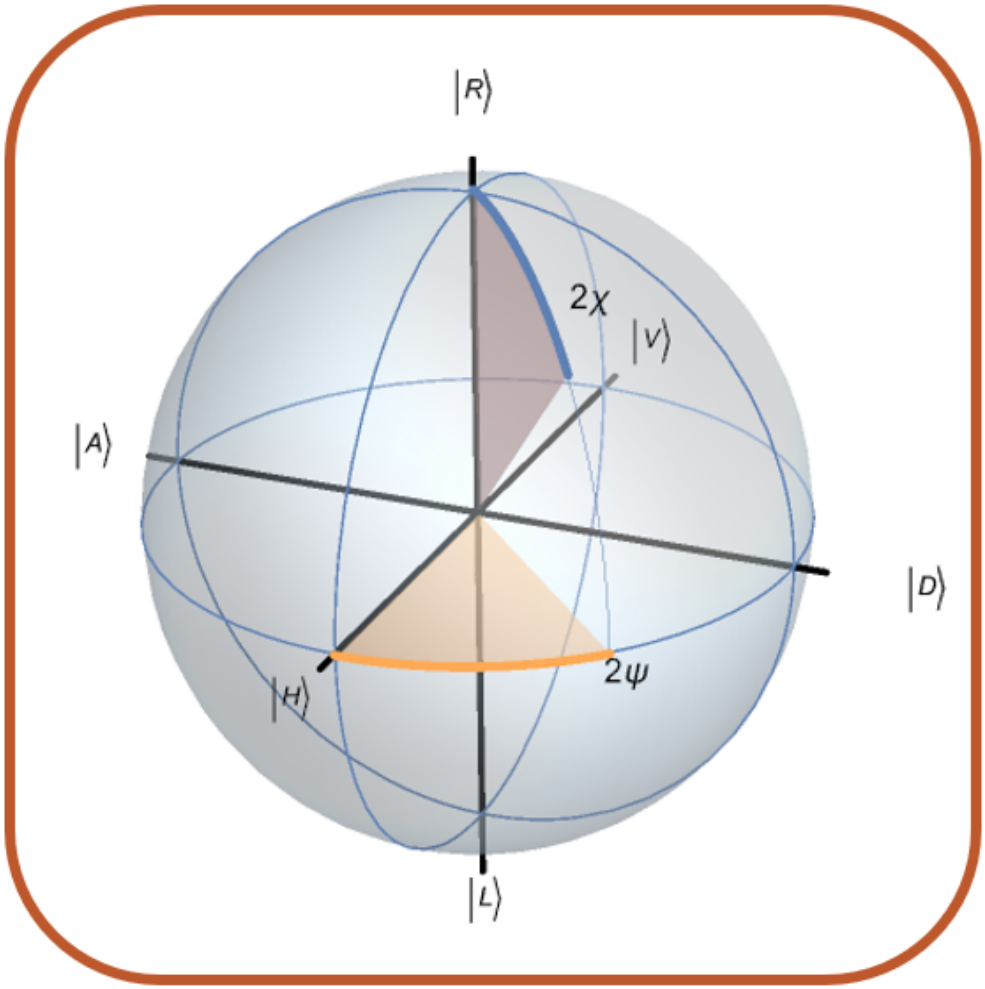

Figure 1.2: The Poincaré sphere is one way to map the possible state space that polarisation can occupy. Any polarisation can be expressed as a point on its surface in spherical polar coordinates 2χ and 2ψ. Linear polarisations are mapped to the equator, while circular polarisations form the poles.

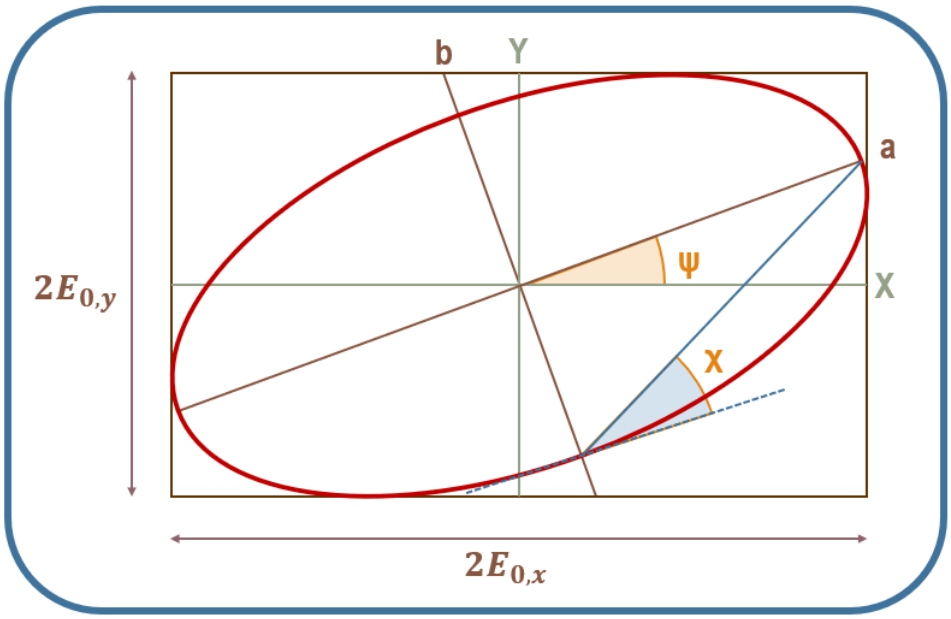

Figure 1.3: The angles on the Poincaré sphere are good for describing any arbitrary polarisation in more ways than one - as both circles and lines are technically special cases of ellipses, they can be used to describe the parameters of the elliptically varying electric fields directly. ψ forms an angle between the horizontal plane and the ellipse's vertex, and χ forms an angle between the line connecting the axes of the ellipse and its tangent.

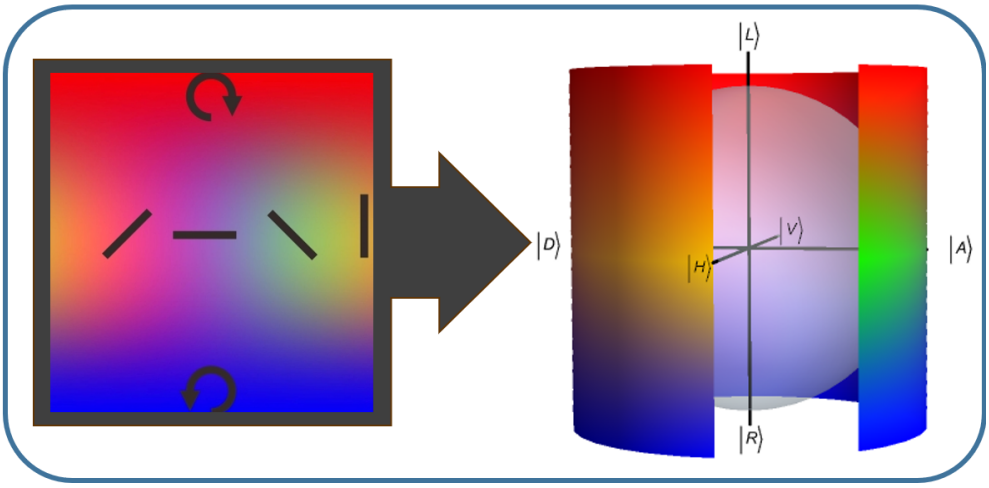

Figure 1.4: The polarisation colour map is the Mercator projection of the Poincaré sphere and will be used to denote polarisation from this point on. The ellipses on the map show the ellipticity and orientation of the polarisation at the specific point, i.e the polarisation is indicated by both colour and line.

The polarisation ellipse notation does not see very much use, but becomes very useful in situations in which no clear basis state emerges. Such a case will be considered very closely in chapter 6.3.2. Like Jones, the polarisation ellipse notation is incapable of describing unpolarised light. As of writing this thesis, the most common way to describe changes to the polarisation due to optical elements is by transforming the ellipse into an alternative notation and then back again.

It is also of note that there are multiple conflicting conventions for how the angles on the Poincaré sphere should be defined. The convention displayed in this section is consistently used throughout this thesis, but in other works, χ and ψ may be defined differently.

1.3.2 the polarisation colour map

The Poincaré sphere also directly relates to the colour coding of polarisation used throughout this thesis, as well as all of the newer works carried out by and under Professor S. Franke-Arnold [28, 29]. Shown in figure 1.4 in its Mercator projection, each point on the Poincaré sphere relates to a unique colour, with the local intensity dictating the colour's brightness, with white representing zero intensity. Additionally, the local ellipticity and orientation are indicated by a corresponding ellipse plotted on top of the colour scheme. This colourmap efficiently displays multiple degrees of freedom within one image. Examples of beams with spatially varying polarisation can be found later in figure 2.6 of chapter 2.2.

1.4 Stokes vectors

WHICH INTRODUCES STOKES VECTORS AND MUELLER MATRICES AS A FORM OF POLARISATION NOTATION, AND EXPLAINS THE SIGNIFICANCE OF THE STOKES BASIS

STATES.

As stated previously in chapter 1.2, Jones vectors are great at describing the polarisation in minimal terms, defined in relation to one pair of orthogonal basis states. However, phases are not directly measurable, making Jones vectors difficult to derive from experimental data. **Stokes vectors**, in contrast, are optimised to consist only of real parameters that come from three sets of mutually unbiased basis states. Two sets of vectors are considered mutually unbiased if each vector from one set can be expressed as an equal superposition of all vectors in the other, and vice versa.

The Stokes bases, which have been used as examples in all sections so far, are named for G.G. Stokes, as they formed the base of the polarisation notation he invented in 1852 [30]. In this form, the polarisation is expressed in a form of a four-dimensional vector - one element expressing the overall intensity, and the other three containing the relative weighting of the three basis pairs:

$$S_0 = I_H + I_V = I_A + I_D = I_R + I_L \tag{1.40}$$
$$S_1 = I_H - I_V \tag{1.41}$$
$$S_2 = I_D - I_A \tag{1.42}$$
$$S_3 = I_R - I_L. \tag{1.43}$$

with $S_{0,1,2,3}$ being the elements within the Stokes vector $\vec{S}$. This notation has one major benefit over the ones previously discussed: The intensity parameter S_0 enables it to express unpolarised or partially polarised light.

Each of the normalised Stokes basis states has the following Stokes vector:

$$|H\rangle \hat{=} \begin{pmatrix} 1 \\ 1 \\ 0 \\ 0 \end{pmatrix} \qquad |V\rangle \hat{=} \begin{pmatrix} 1 \\ -1 \\ 0 \\ 0 \end{pmatrix} \tag{1.44}$$
$$|A\rangle \hat{=} \begin{pmatrix} 1 \\ 0 \\ 1 \\ 0 \end{pmatrix} \qquad |D\rangle \hat{=} \begin{pmatrix} 1 \\ 0 \\ -1 \\ 0 \end{pmatrix} \tag{1.45}$$
$$|R\rangle \hat{=} \begin{pmatrix} 1 \\ 0 \\ 0 \\ 1 \end{pmatrix} \qquad |L\rangle \hat{=} \begin{pmatrix} 1 \\ 0 \\ 0 \\ -1 \end{pmatrix}. \tag{1.46}$$

Stokes vectors provide an immediate and very detailed view of the local polarisation structure that is legible on first sight. The Stokes basis states are used in the most common form of polarimetry (see chapter 2.3), and hence are useful for data interpretation. As such, Stokes notation is very popular in polarisation optics. The downside is that the elements of the vector aren't orthogonal, as information about orthogonal basis states is always contained in a single parameter, and hence the

Stokes parameters on their own aren't really useful in equations. This, however, did not prevent it from being used.

1.4.1 Mueller matrices

Optical elements can be represented by 4x4 **Mueller matrices**, the Stokes equivalent to the Jones matrices introduced in chapter 1.2.1. A Mueller matrix takes the form:

$$\hat{M} = \begin{pmatrix} M_{00} & M_{01} & M_{02} & M_{03} \\ M_{10} & M_{11} & M_{12} & M_{13} \\ M_{20} & M_{21} & M_{22} & M_{23} \\ M_{30} & M_{32} & M_{32} & M_{33} \end{pmatrix}. \tag{1.47}$$

Just like Stokes vectors are more general than Jones vectors, Mueller matrices are more general than Jones matrices, as they can include decoherent processes or depolarising elements.

As the Stokes vector separates the descriptors of intensity and polarisation, the Mueller matrix does the same: components that act on the intensity work differently from those that alter the polarisation. Any optical element that preserves the overall intensity will have $M_{00} = 1$, and $M_{10}, M_{20}, M_{30}, M_{01}, M_{02}$, and $M_{03} = 0$. All other elements describe the phase shifts that alter the polarisation. but some rules apply: There is nothing inherent to the matrices that prevents a resulting Stokes vector from describing a polarisation that doesn't exist, e.g. a higher value in S_{123} than in S_0, so the matrices have to be configured in such a way that a matrix with a change in one parameter also has the corresponding changes in the others.

For illustrative purposes, it makes sense to revisit the examples given for Jones matrices in chapter 1.2.1, which begun with the QWP. Its Mueller matrix form looks like this [17]:

$$\hat{M}_{\text{QWP}} = \begin{pmatrix} 1 & 0 & 0 & 0 \\ 0 & \cos^2 2\theta & \cos 2\theta \sin 2\theta & \sin 2\theta \\ 0 & \cos 2\theta \sin 2\theta & \sin^2 2\theta & -\cos 2\theta \\ 0 & -\sin 2\theta & \cos 2\theta & 0 \end{pmatrix}. \tag{1.48}$$

The special cases of horizontal or vertical fast axis alignment simplify here also:

$$\hat{M}_{\text{QWP,horizontal}} = \begin{pmatrix} 1 & 0 & 0 & 0 \\ 0 & 1 & 0 & 0 \\ 0 & 0 & 0 & 1 \\ 0 & 0 & -1 & 0 \end{pmatrix} \tag{1.49}$$

$$\hat{M}_{\text{QWP,vertical}} = \begin{pmatrix} 1 & 0 & 0 & 0 \\ 0 & 1 & 0 & 0 \\ 0 & 0 & 0 & -1 \\ 0 & 0 & 1 & 0 \end{pmatrix}. \tag{1.50}$$

Now it becomes visible that in these special cases, the wave plate effectively "swaps" S2 and S3.

Like with Jones, the Mueller matrix for a HWP is more simple:

$$\hat{M}_{\text{HWP}} = \begin{pmatrix} 1 & 0 & 0 & 0 \\ 0 & \cos 4\theta & \sin 4\theta & 0 \\ 0 & \sin 4\theta & -\cos 4\theta & 0 \\ 0 & 0 & 0 & -1 \end{pmatrix}. \tag{1.51}$$

The Mueller matrix for linear polarisers highlights the removal of all circular components:

$$\hat{M}_{\text{LP}} = \frac{1}{2} \begin{pmatrix} 1 & \cos 2\theta & \sin 2\theta & 0 \\ \cos 2\theta & \cos^2 2\theta & \cos 2\theta \sin 2\theta & 0 \\ \sin 2\theta & \cos 2\theta \sin 2\theta & \sin^2 2\theta & 0 \\ 0 & 0 & 0 & 0 \end{pmatrix}. \tag{1.52}$$

This is also the first optical element considered in this section that alters the intensity.

When considering mirrors, the same assumptions are made as in the section on Jones matrices: the mirror is fully vertical in the lab frame with a tilt only in the horizontal direction, and perfect reflectivity. An ideal mirror like this has the following Mueller matrix:

$$\hat{M}_{\text{mirror}} = \begin{pmatrix} 1 & 0 & 0 & 0 \\ 0 & 1 & 0 & 0 \\ 0 & 0 & -1 & 0 \\ 0 & 0 & 0 & -1 \end{pmatrix}. \tag{1.53}$$

This is another good example of the improved legibility of Stokes/Mueller calculus, as this form highlights that polarisations at an angle to the tilt axis get inverted.

The Mueller matrix for the optical rotator similarly illustrates that the effect is confined to linear polarisations [31]:

$$\hat{M}_{\text{rot}}(2\theta) = \begin{pmatrix} 1 & 0 & 0 & 0 \\ 0 & \cos 2\theta & \sin 2\theta & 0 \\ 0 & -\sin 2\theta & \cos 2\theta & 0 \\ 0 & 0 & 0 & 1 \end{pmatrix}. \tag{1.54}$$

S_3 is conserved in this equation, which shows that this is an effect from circular birefringence.

A system with multiple optical elements can be described by a series of Mueller matrices acting on the initial Stokes vector in reverse order of propagation:

$$\vec{S}_{\text{out}} = \hat{M}_{\text{n}} \hat{M}_{n-1} ... \hat{M}_2 \hat{M}_1 \vec{S}_{\text{in}}. \tag{1.55}$$

In this section, many comparisons have been made between the different forms of notation, and it has been highlighted each has different strengths and weaknesses.

1.5 conversion between polarisation notations

WHICH ESTABLISHES WIDELY USED METHODS FOR THE CONVERSION BETWEEN THE PREVIOUSLY DISCUSSED POLARISATION NOTATIONS

Throughout this chapter, three different polarisation notation, each with their own strengths and weaknesses have been introduced. Jones notation is very simple and intuitive, as long as the interpretation is centered around linear basis states. Polarisation ellipse notation doesn't have this problem, as it is not based on an underlying assumption of default states, but its generality and legibility do not mean it sees much use. It has no clear convention, no standardised analog for optical components, its obscurity makes people often choose other bases in in favour of it, and, importantly, there is no direct way to measure it. This is the aspect where the Stokes vector comes to shine - it relates directly to the most common method of polarimetry (details in chapter 2.3) and is very easy to interpret at first glance. However, its parameters aren't orthogonal, making it difficult and unintuitive to use in theoretical work, as its components can not be easily separated from one another. However it is the only notation introduced so far that is capable of describing unpolarised or partially polarised light. In other words, the optimal polarisation notation depends on the context, and it is useful to be able to freely switch between them.

The majority of the work in this thesis concerns itself with fully polarised light (or experimental approximations thereof). In this limit, the three notations become interchangeable. They relate to each other as follows for a normalised beam:

$$S_0 = I \qquad = |\tilde{E}_x|^2 + |\tilde{E}_y|^2 \tag{1.56}$$

$$S_1 = I \sin 2\chi \cos 2\psi = |\tilde{E}_x|^2 - |\tilde{E}_y|^2 \tag{1.57}$$

$$S_2 = I \sin 2\chi \sin 2\psi = 2\mathsf{Re}[\tilde{E}_x \tilde{E}_y^*] \tag{1.58}$$

$$S_3 = I \cos 2\chi \qquad = -2\mathsf{Im}[\tilde{E}_x \tilde{E}_y^*]. \tag{1.59}$$

The transformation between the Stokes parameters and the polarisation ellipse is no more than a change between Cartesian coordinates and spherical polar coordinates. Therefore, Stokes notation and the polarisation ellipse are sometimes treated as two versions of the same theoretical model. The code generating the colourmap introduced in chapter 1.3.2 uses this conversion when interpreting experimental data.

Conversion between notation is not limited to polarisation vectors: Jones matrices can be easily transformed into Mueller matrices [17][32]:

$$\hat{M} = \hat{A}(\hat{J} \otimes \hat{J}^*)\hat{A}^{-1}. \tag{1.60}$$

with the transformation operator $\hat{A}$

$$\hat{A} = \begin{pmatrix} 1 & 0 & 0 & 1 \\ 1 & 0 & 0 & -1 \\ 0 & 1 & 1 & 0 \\ 0 & i & -i & 0 \end{pmatrix}. \tag{1.61}$$

The inverse transformation is often deemed impossible, as Mueller matrices can contain depolarising elements which cannot be described by Jones matrices.

1.5.1 alternative Jones bases

When the Jones vector was first introduced in chapter 1.2, it was mentioned that $\tilde{E}_x$ and $\tilde{E}_y$ are usually taken to mean $\tilde{E}_H$ and $\tilde{E}_V$, though this does not have to be the case - $\tilde{E}_x$ and $\tilde{E}_y$ just means any linear orthogonal bases. To illustrate this, consider the diagonal-antidiagonal basis by performing a coordinate rotation:

$$\tilde{E}_A = \frac{1}{\sqrt{2}}(\tilde{E}_H - \tilde{E}_V) \tag{1.62}$$

$$\tilde{E}_D = \frac{1}{\sqrt{2}}(\tilde{E}_H + \tilde{E}_V), \tag{1.63}$$

so the Jones vector in this new basis can now be written as:

$$\vec{E} = \begin{pmatrix} \tilde{E}_A \\ \tilde{E}_D \end{pmatrix}. \tag{1.64}$$

This is equivalent to tilting your head, or the laser and/or camera by 45 degrees, and hence sort of trivial.

However, it doesn't have to be a linear basis: A beam can also be expressed in terms of its right and left circular electric fields u_+ and u_- and their relative phase. Their naming convention is different from the linear bases as a nod to atomic physics, a context in which this basis sees much use (see chapter 6.3.1). This basis change is calculated as follows:

$$u_- = \frac{1}{\sqrt{2}}(\tilde{E}_H - i\tilde{E}_V) \tag{1.65}$$

$$u_+ = \frac{1}{\sqrt{2}}(\tilde{E}_H + i\tilde{E}_V). \tag{1.66}$$

The Jones vector in the circular basis stats can now be written as:

$$\vec{E} = \begin{pmatrix} u_+ \\ u_- \end{pmatrix}. \tag{1.67}$$

There is a pattern to all of these states: as the coordinate system of the Poincaré has orthogonal bases on opposite ends of each axis, a Jones vector has the sole constraint that the two basis polarisations have to be on opposite sides of the Poincaré sphere - otherwise any possible angles can be chosen. Such coordinate rotations in state space is known in some areas of physics as a dressed state picture. The general intent between such redefinitions of the coordinate system is to simplify the maths, or the interpretation. Optics concerns itself with the wavelike nature of light, so in this context this is not simply a mathematical tool, but an equally valid description of the electric field. As will be found later in chapter 6.3.2, this technique and interpretation is valid for other, quantum mechanical objects too.

Though it gets even stranger: basis states don't have to stick to a single pair of points on the Poincaré sphere, they can be spatially dependent. In order to explore this, one needs to consider the macroscopic intensity structure of the beam, and familiarise oneself with spatial polarisation structures. This idea will be revisited in chapter 3.1 and introduce one final set of Jones bases - alongside a type of polarisation that has gone previously undiscussed.

2 the structure of light

Consider the plane wave introduced in equation 1.7 of the last chapter: A sine function describing an electric field, oscillating into infinity in both directions along the propagation axis. Consider trying to focus this beam with a lens. Now, all the electric field converges to a single point at the focus. However, a point has no area - our beam now has infinite intensity. This can't be right.

Such was the reasoning behind the initial disproving of ray optics, and its subsequent replacement with Gaussian optics. The latter still makes some assumptions about the beam, like the paraxial approximation (which will be dealt in later on in this thesis) but introduces several new concepts, like the waist, which is the radius of the beam at the focus, or the Gouy phase. It concerns itself with solutions to the Helmholtz equation. Solutions to the Helmholtz equation keep the same transverse shape as they propagate, they are known as eigenmodes of propagation, or just modes. Higher order modes interfere with themselves. Superimposing multiple higher order modes can lead to the creation of further modes still.

Of course, for interference to happen, the polarisation has to be the same. Superimposing beams with different intensity structure and different polarisation can cause both of them to interfere and make a beam with spatially varying polarisation.

By the end of this section, much of the groundwork for the optical work in this thesis will have been lain. It aims to provide an overview of structured light in both the experimental and the theoretical realm.

2.1 modes of propagation

AN INTRODUCTION TO THE EIGENMODES OF PROPAGATION IN GAUSSIAN OPTICS, WITH A FOCUS ON GAUSSIAN, HERMITE-GAUSSIAN, AND LAGUERRE-GAUSSIAN BEAMS, THEIR GENERATION AND CONVERSION, AS WELL AS ORBITAL ANGULAR MOMENTUM IN OPTICS.

Laser modes, or eigenmodes of propagation, are beams that do not change shape when propagating through free space or a homogeneous medium. This is because they are plane wave solutions to the Helmholtz equation.

The Helmholtz equation is a partial differential eigenvalue equation that describes a time independent form of the wave equation 1.7

$$\nabla^2 A = -k^2 A, \tag{2.1}$$

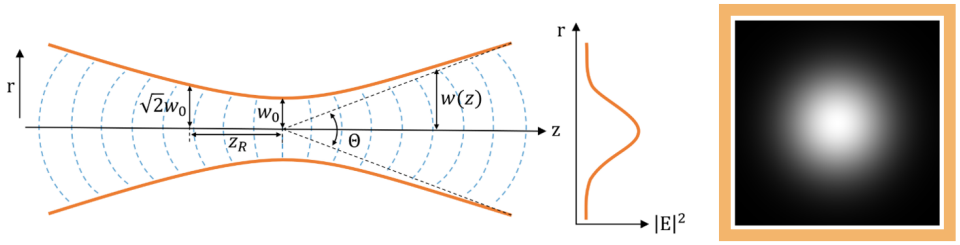

Figure 2.1: The characteristics of a Gaussian beam are its waist, its intensity distribution, and its curved phase front. On the right in the orange box is the intensity distribution in the transverse plane. It is the same in all planes of propagation. Sourced from [17]

.

where ∇^2 is the divergence in two orthogonal variables, ie the Laplace operator, k is the eigenvalue, and $A = u(\vec{r})e^{ikz}$ is the spatial wave function in question.

As discussed previously, the plane wave assumes the beam to extend infinitely in the transverse plane. However, when interacting with the universe, this is unrealistic. A more applicable solution can be coaxed from the Helmholtz equation by making the paraxial approximation, i.e. assuming that the electric field is always perfectly transverse to the propagation direction. This approximation is valid in systems where all surfaces are flat or portions of a sphere [33].

In 1841 a whole field sprung up around this principle, championed by C.F. Gauss [16]. It is called Gaussian optics, though sometimes also called paraxial optics or first order optics. At its centre lies one of the simplest paraxial solutions of the Helmholtz equation: the **Gaussian beam**.

2.1.1 the Gaussian beam

The Gaussian beam has a Gaussian distribution of intensity in the transverse plane. This means the electric field is still present everywhere, though it tends towards 0 as the transverse radius $r = \sqrt{x^2 + y^2}$ goes to infinity. To characterise its distribution, the **beam waist** w is introduced. It describes the transverse radius at which the intensity falls below $1/e^2$ of the on axis value. For now, consider the beam to propagate through free space along the z direction [33]:

$$\tilde{E}(r,z) = E_0 \frac{w_0}{w(z)} \exp\left(-\frac{r^2}{w(z)^2}\right) \exp\left(-i\left(kz + k\frac{r^2}{2R(z)} - \psi(z)\right)\right), \quad (2.2)$$

where $\tilde{E}(r,z)$ is the complex electic field at transverse radius r and distance z from the focus, k is the wave number, E_0 is the amplitude, and the propagation dependent beam waist $w(z)$ reaches its minimum $w(0) = w_0$ at the focus. The distance in the propagation direction from the focus is crucial to this beam in more

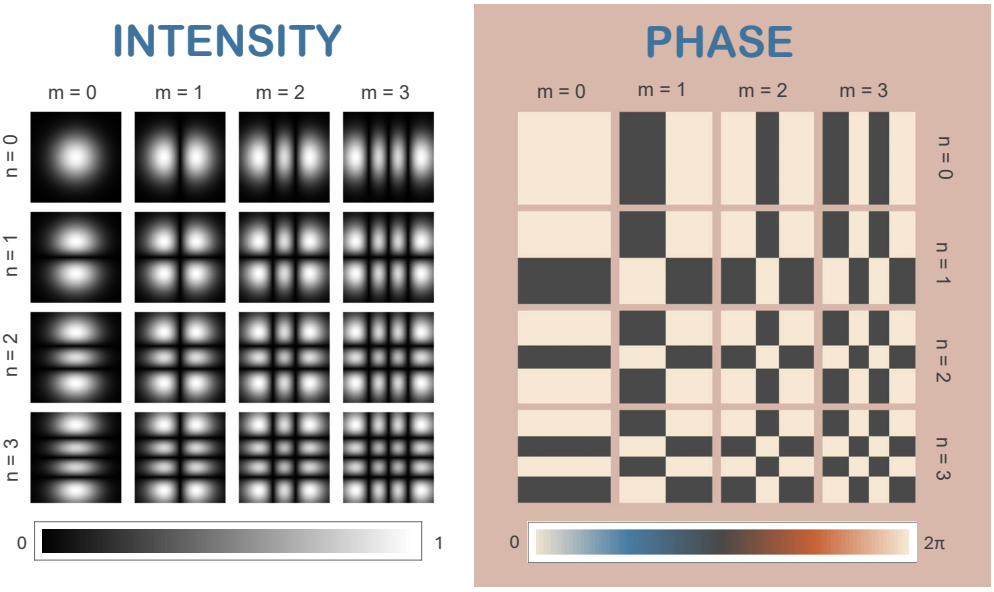

Figure 2.2: Simulated HG modes with polynomial orders m and n each ranging from 0 to 3, in columns and rows, respectively. Their intensity profiles are displayed on the left and their phase structures on the right. Note the phase changes occur at points of 0 amplitude.

than one way, as the waist is the only place in which the beam has a flat phase profile. Due to diffraction, its phase fronts gain curvature with distance from the focus, as described by the Gouy phase

$$\psi(z) = \arctan\left(\frac{z}{z_R}\right), \tag{2.3}$$

which in turn depends on the Rayleigh range $z_R = \pi\omega_0^2/\lambda$, which also determines the radius of curvature of the wavefronts [34]:

$$R(z) = z\left[1 + \left(\frac{z_R}{z}\right)^2\right]. \tag{2.4}$$

One important aspect of the Gaussian beam is that its transverse intensity profile remains constant regardless of position and time. This property makes it an **eigenmode of propagation**.

All of these parameters are illustrated in figure 2.1, alongside its transverse intensity profile. The Gaussian beam is sometimes also called TEM_{00}, which stands for transverse electric and magnetic. The 00 indicates the absence of nodes in the transverse plane [33]. Of course, this notation implies the existence of a beam with nodes in the transverse plane. Higher order solutions for the paraxial Helmholtz equations begin to depend on the very coordinate system that is used to solve them. In the next portion of this chapter, two different types of solution will be discussed.

2.1.2 Hermite Gaussian mode

Solving the paraxial wave equation in a Cartesian coordinate system yields a set of solutions dependent on a **Hermite polynomial** in each orthogonal spatial direction of independent orders m and n, where m and n are positive integers. Beams of this form are known as Hermite-Gauss (HG) modes, as their curved phase structure mirrors that of the Gaussian beam (equations 2.2-2.4). Like the Gaussian beam, all HG beams are eigenmodes of propagation. The complex electric field of any HG beam is described by the following equations [17]

$$\begin{aligned} HG_{nm}(x,y,z) =& E_0\sqrt{\frac{2^{1-m-n}}{m!n!\pi}}\frac{w_0}{w(z)} \times H_m\left(\frac{\sqrt{2}x}{w(z)}\right) \times H_n\left(\frac{\sqrt{2}y}{w(z)}\right) \\ & \times \exp\left[-\frac{x^2+y^2}{w(z)^2}\right] \times \exp\left[-ik\left(z+\frac{x^2+y^2}{2R(z)}\right)\right] \\ & \times \exp\left[i(n+m+1)\psi(z)\right], \end{aligned} \tag{2.5}$$

where H_m and H_n are the eponymous Hermite polynomials. As shown in figure 2.2, these beams consist of a number of distinct spots of high intensity arranged in a grid pattern, with $n+1$ rows and $m+1$ columns. Between any two spots there is always a phase shift of π at the point of zero intensity, in fact, these points are caused by the destructive interference from the phase shift. The order of the mode, or mode number, is the sum of the polynomial orders:

$$N = m + n. \tag{2.6}$$

Beams with the same mode number always have the same Gouy phase. Note that if $m = n = N = 0$, the equation simplifies to TEM_{00} - the Gaussian beam. However as mentioned previously, the available solutions depend on the coordinate system used. Consider instead, for example, a polar coordinate system.

2.1.3 Laguerre Gaussian mode

If the paraxial wave equation is solved in a cylindrical coordinate system, another set of solutions is derived. This time, they take the form of Laguerre polynomials, which are characterised by the radial order p and the azimuthal order ℓ. The resulting Laguerre-Gaussian (LG) modes share the curved phase structure of Gaussian and HG beams. Their complex amplitude is given by the following equation:

$$\begin{aligned} LG_p^{\ell}(r,\phi,z) =& \sqrt{\frac{2p!}{\pi(p+|\ell|)!}} \times \frac{w_0}{w(z)}(\sqrt{2}\frac{r}{w(z)})^{|\ell|}\exp\left(-\frac{r^2}{w(z)^2}\right)L_p^{|\ell|}(\frac{2r^2}{w(z)^2}) \\ & \times \exp\left(-ik\frac{r^2}{2R(z)}\right)\exp(i\ell\phi)\exp[i(2p+|\ell|+1)\psi(z)], \end{aligned} \tag{2.7}$$

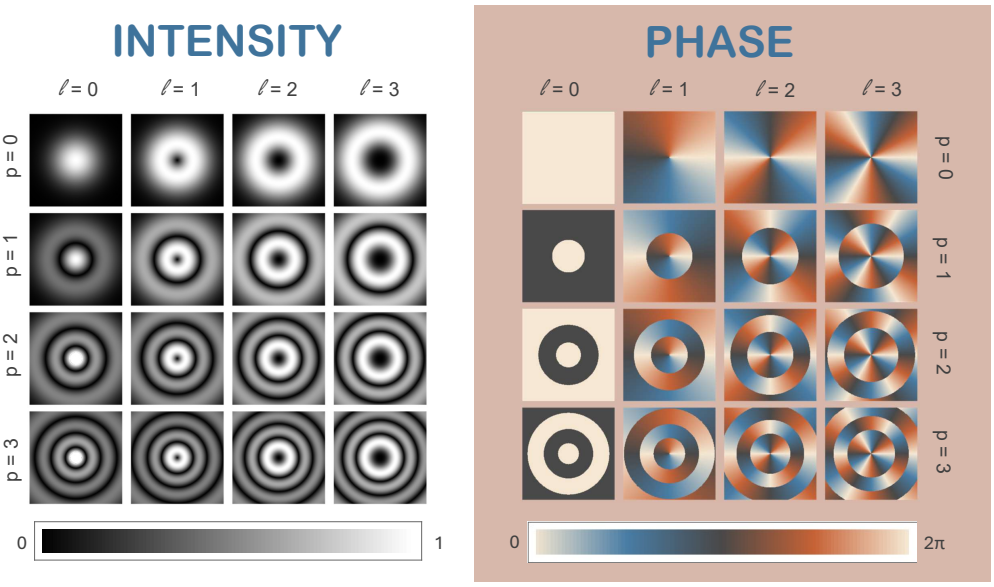

Figure 2.3: Simulated LG modes with polynomial orders ℓ and p each ranging from 0 to 3, in columns and rows, respectively. Their intensity profiles are displayed on the left and their phase structures on the right. The azimuthal order ℓ changes the beam's number of equal phase fronts. Phase changes of π occur at zero intensity.

where $L_p^{|\ell|}$ is the associated Laguerre polynomial. In another analogue to HG beams, the mode number of an LG beam is:

$$N = 2p + |\ell|. \tag{2.8}$$

Once again, if $\ell = p = N = 0$, the solution becomes a Gaussian beam. Figure 2.3 shows LG beams for a selection of ℓ and p values, their intensity structure taking the form of concentric rings. While p works very similarly to m and n of the HG mode, its value confined to positive integers. These integers dictate the number of phase shifts of π, and hence the number of rings = $p + 1$. The parameter ℓ is different to anything discussed so far in this thesis - its effect presents in the continuous spiral phase structure across the azimuth of the beam. The higher the magnitude of ℓ, the more often the phase pattern repeats. However, ℓ can take any integer value, and for negative ℓ, the phase structure inverts, and the phase spirals into the opposite direction. This spiral phase structure has additional meaning.

orbital angular momentum

A spiralling phase means something is rotating. Where there is rotation, there is angular momentum. In other words, the azimuthal number ℓ also describes the amount of **orbital angular momentum** (OAM) contained in the beam [35].

Take a step back. What does this mean?

Light can carry two separate forms of angular momentum: Intrinsic spin was introduced in chapter 1.1.1 and is carried in the rotation of the electric field of circularly polarised light. In contrast, OAM is carried by the phase structure of the beam. It is a global and extrinsic property, and it was not known that it could be carried by laser

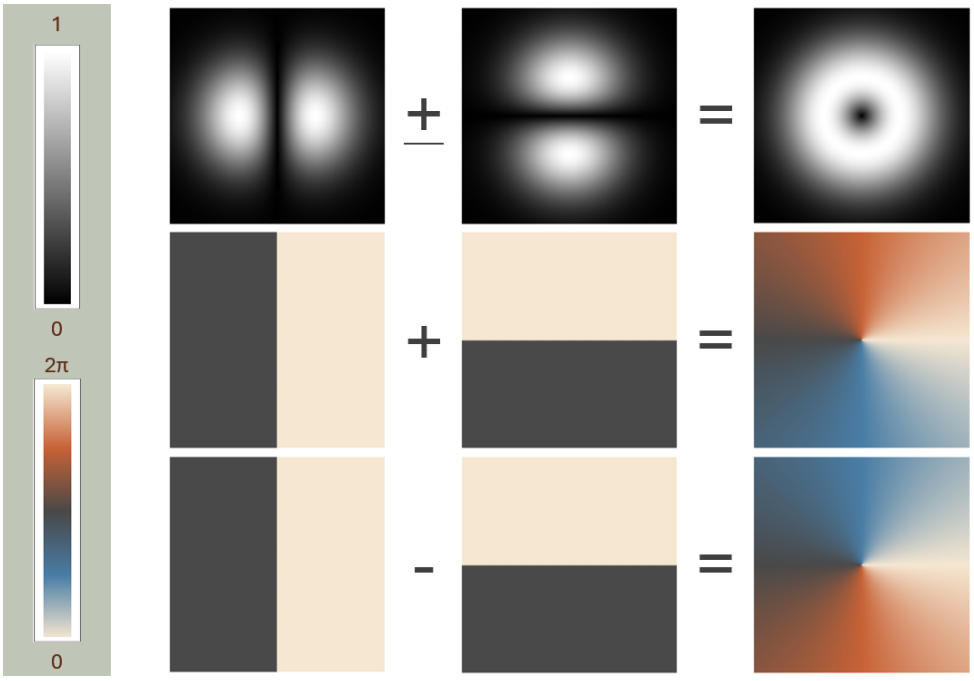

Figure 2.4: Generating a $LG_0^{\pm 1}$ beam via superposition of a $HG_{0,1}$ and $HG_{1.0}$ beam. The intensity pattern always gains the same shape, but the phase profile depends on the relative phase between the HG components.

modes until 1992 [36]. The value of OAM per photon is ℓh, this means that ℓ takes on the additional meaning of topological charge. Sometimes it is useful to consider the total angular momentum $\hbar(\ell + \sigma)$ of a photon [37].

OAM is not exclusive to LG modes. Other beams, such as Bessel beams [38], can also carry helical phase fronts, though this thesis largely concerns itself with eigenmodes of propagation.

2.1.4 conversion between modes via superposition

LG modes and HG modes are solutions to the Helmholtz equation in polar and Cartesian coordinate systems, respectively. An HG mode should therefore still be a solution when expressed in polar coordinates and vice versa, albeit a more complicated one.

The way this presents is as a series of superpositions. Consider a $HG_{0,1}$ mode. It consists of two intensity lobes of opposite phase. A $HG_{1,0}$ mode consists of the same two intensity lobes but at ninety degrees to the first one. If these two beams (both of the same polarisation) are superimposed, they will interfere based on relative amplitude and phase. The phase between the lobes matters as much as the phase between the beams - figure 2.4 shows that the resulting intensity profile will be a ring for a phase difference of $\pm\pi/2$, however the ℓ number of the resulting LG mode depends on the phase.

This process also works the other way: LG modes can be added to yield a HG

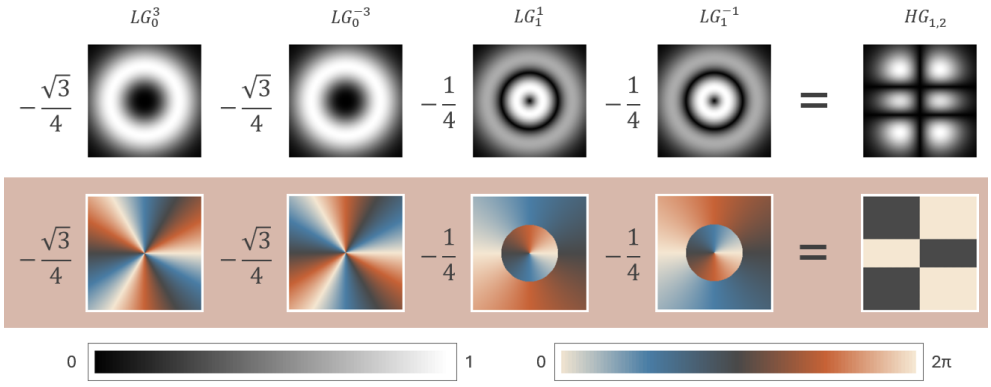

Figure 2.5: Generation of a $HG_{1,2}$ beam via superposition of LG modes. Interference in the spiralling phase structures causes the lobed intensity distribution.

mode. Two LG modes with opposite ℓ will see constructive and destructive interference along the azimuth and take on a lobed structure - the positions of which depend on the relative phase. This highlights the arbitrary nature of the choice in xy-basis, and provides a way of rotating the coordinate system of HG modes (though plain superposition of flat phased HG modes should also do the trick).

There is a rule for converting the beams both ways: Any HG or LG beam with mode number N can be created by superimposing N+1 specific beams from the other mode family, where each must also have mode number N. Generally, this set of beams is symmetric - the maximum m and n are the same, and for each mode with ℓ there is one with corresponding $-\ell$ [17, 39, 40]. Examples of such conversions can be found in figure 2.5.

There is another family of solutions to the paraxial wave equation using Ince polynomials and elliptical coordinates. They are known as Ince-Gaussian (IG) beams. Ince polynomials are ruled by their ellipticity parameter ε, and at its limits $\varepsilon = 0$ and $\varepsilon = \infty$ they simplify to HG and LG modes, respectively, providing an intermediate stage between them [41].

Eigenmodes of propagation are core to the majority of the work presented in the rest of this thesis. They are highly useful for experimental setups, as their intensity does not change during propagation. Any superposition of higher order modes with the same mode number has a matched Gouy phase, so it will not change either. The following section exploits this principle to create beams with spatially varying polarisation structure that does not change during propagation.

2.2 polarisaton structures

WHICH INTRODUCES VECTOR BEAMS, THEIR METHODS OF CREATION, AND THEIR QUANTIFICATION VIA OPTICAL CONCURRENCE

Chapter 1.1 was about how superimposing two beams, each with a different po-

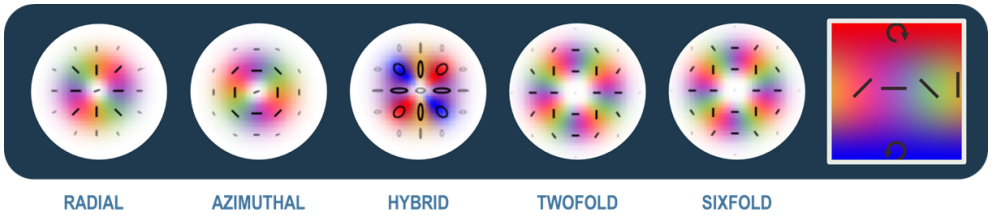

Figure 2.6: Five different structured beams created from the superposition of eigenmodes of propagation. Radial, azimuthal, and hybrid beams are created from beams with mode number 1, whereas twofold and sixfold beams are made from beams with mode number 2.

larisation leads to interference of polarisation. The result is a beam with a third polarisation, determined by the component polarisations, and their relative phase and amplitude. Chapter 2.1.4 was about superimposing different eigenmodes of propagation with the same polarisation but different spatial intensity and phase structures to transform them into a different mode.

The next question is obvious: What beam results from a superposition of different modes with different polarisations? At any given point in space the polarisations will interfere, depending on the local amplitude and phase of both component beams. The result is a beam with a spatially varying polarisation structure [39]. Examples of such beams can be seen in figure 2.6. This type of polarisation structured beam is sometimes referred to as a vector beam (the definition of which will be further discussed in chapter 2.2.1).

Consider the previous example from chapter 2.1.4: Adding an LG_0^1 and LG_0^{-1} mode right circular polarisation results in a $HG_{0,1}$ mode of the same polarisation. Adding instead a $LG_0^1 |R\rangle$ and $LG_0^{-1} |L\rangle$ beam with no phase shift between them instead results in what is commonly referred to as a **radial beam**, or $|\varrho\rangle$, as the polarisation is always aligned with a vector pointing away from the propagation axis in the transverse plane. This beam once again has a flat phase front. The same beam can be derived from opposite HG modes also, by adding a $HG_{1,0} |H\rangle$ and $HG_{0,1} |V\rangle$ beam, again with no phase change:

$$|\varrho\rangle = \frac{1}{\sqrt{2}} \left(LG_0^1 |R\rangle + LG_0^{-1} |L\rangle \right) = \frac{1}{\sqrt{2}} \left(HG_{1,0} |H\rangle + HG_{0,1} |V\rangle \right). \tag{2.9}$$

Vector modes can be orthogonal to one another. A beam that is orthogonal to the radial beam is the **azimuthal beam** $|\varphi\rangle$. If expressed in terms of LG modes it is exactly the same, but with a phase difference of π. However if expressed in HG modes, one can see that the modes (or polarisations) have swapped:

$$|\varphi\rangle = \frac{1}{\sqrt{2}} \left(LG_0^1 |R\rangle - LG_0^{-1} |L\rangle \right) = \frac{1}{\sqrt{2}} \left(HG_{0,1} |H\rangle + HG_{1,0} |V\rangle \right). \tag{2.10}$$

These beams are radially homogeneous, as their component modes all have

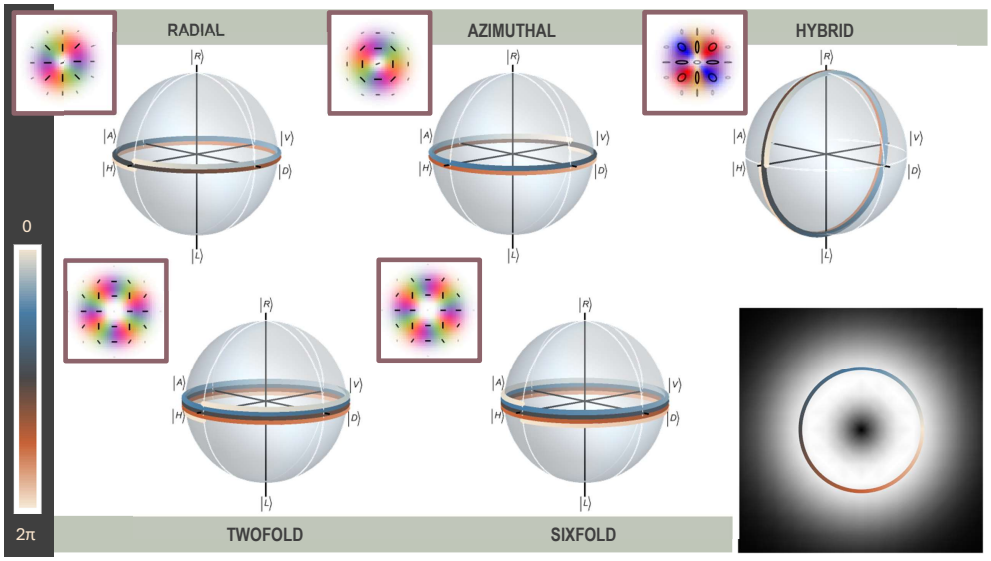

Figure 2.7: A radial beam spans a grand circle on the Poincaré sphere along the equator, correlating the polarisation angle ψ with the spatial angle φ. An azimuthal beam does too, but there is a phase shift of π between spatial and polarisation angle. A beam consisting of LG modes with higher ℓ wraps around the Poincaré sphere multiple times (shown here are beams generated from $LG_0^{\pm 2}$ beams). The signs of the ℓs do not affect the polarisations featured, but change the symmetry of the beam - note the twofold beam and sixfold beam wrap around the Poincaré sphere in opposite directions. Hybrid beams feature spatially varying ellipticity, and so their φ correlates to χ.

consistent radii. Their polarisation structure can be mapped onto the Poincaré sphere, drawing a line on its surface. Beams that have intensity structure in both the azimuthal and radial direction will instead display as a surface area wrapping around the Poincaré sphere. In the case of a radial or azimuthal beam, each linear polarisation is featured twice, so the line wraps around the equator of the Poincaré sphere two times. Beams generated from higher order modes might wrap the Poincaré sphere more often, in the case of equal and opposite LG modes this is proportional to $|\ell|$. Beams featuring elliptical or circular polarisations have trajectories other than the equator. Some examples of this are highlighted in figure 2.7. Note that the direction and starting point are as impactful to the beam structure as the polarisations covered.

In chapter 2.1.3 it was discussed that LG modes carry OAM. If two LG modes with equal and opposite OAM interfere, it cancels out. Because of this, all vector beams discussed in this thesis have flat phase fronts at the focus, and a uniform phase profile throughout. The relationship of ℓ and the circular polarisation of each component beam also dictates the direction of the vector beam's trajectory around the Poincaré sphere, as seen in the second row of figure 2.7, and later in figure 2.9. This change in symmetry has topological implications [13, 28].

Vector beams are of scientific interest for two reasons: One lies in the topology discussed so far. Much information is to be found in how light interacts with itself, and it is often an accessible analogue for the behaviour of other waves and particles.

It has also been observed that the polarisation structure can affect the focal waist of a beam [42], though focusing a beam also induces an otherwise unattainable polarisation state, as will be shown in chapter 3. The other reason lies in their applicability. Structured beams can be rotationally invariant, making them useful for optical communications between moving objects like satellites, and they have multiple additional degrees of freedom to encode information. If used as a probe in an experiment, they are capable to probe with many if not all polarisations at the same time (a theme that will continue to come up in this thesis).

If such a beam is created from non-orthogonal modes, it will no longer span a grand circle on the Poincaré sphere, meaning the correlation lessens. It can therefore be useful to define the degree of correlation between polarisation and spatial position, if one is investigating the topological properties of the beam.

2.2.1 optical concurrence

Concurrence is a word borrowed from quantum theory, where it serves as a measure of entanglement. In optics, it takes on the meaning of classical nonseparability, which is mathematically indistinguishable from true quantum entanglement - with the caveat that classical concurrence relates correlation between different degrees of freedom, whereas quantum entanglement describes the same degree of freedom being related across multiple particles. Both can be described the following way [43]:

$$|\Psi\rangle = |\psi_1\rangle\,|\hat{e}_1\rangle + |\psi_2\rangle\,|\hat{e}_2\rangle\,, \tag{2.11}$$

where Ψ is a generic wavefunction, $\psi_{1,2}$ are its component wavefunctions, and $\hat{e}$ is the local polarisation vector, with $\hat{e}_1, \hat{e}_2$ being orthogonal. Note the nonseparability of the wavefunction and polarisation. When applied to a vector beam, concurrence is sometimes called "vector quality factor", as it describes the nonseparability, or correlation between two degrees of freedom: spatial position and polarisation.

Concurrence is measured on a unitless scale from 0 to 1, where 0 describes a uniformly polarised beam, and 1 describes any vector beam featuring orthogonal polarisations in different areas. In addition to being a classical analogue to Bell states, it also directly relates to the beam's trajectory on the Poincaré sphere: A uniformly polarised beam only occupies a single point, whereas a vector beam spans a grand circle, as was previously seen and discussed in chapter 2.2, specifically figure 2.7. Consider, for now, a beam consisting of two LG modes with opposite ℓ and opposite circular polarisation:

$$|\Psi\rangle = LG_0^{\ell}\,|R\rangle + e^{i\delta\phi} LG_0^{-\ell}\,|L\rangle\,, \tag{2.12}$$

where $E_{0,R,L}$ is the respective amplitude of each component, LG_p^{ℓ} is the LG mode, and $\delta\phi$ is the relative phase between the beams. It is clear how this equation fills the form of the nonseparability condition in equation 2.11. When reexpressing this in polarisation ellipse notation from chapter 1.3, it becomes more obvious that this nonseparability is conditional on the relative amplitude [14]:

$$|\Psi\rangle = LG_0^{\ell}\cos\chi\,|R\rangle + e^{i\delta\phi} LG_0^{-\ell}\sin\chi\,|L\rangle\,, \tag{2.13}$$

where χ is the latitudinal coordinate on the Poincaré sphere. As the superposition of $LG_0^{\ell}|R\rangle$ and $LG_0^{-\ell}|L\rangle$ will cover all values of ψ on the Poincaré sphere, the concurrence becomes solely dependent on χ [1]:

$$C = \sin(2\chi). \tag{2.14}$$

This is of course a special case, though it can be easily adapted to any other polarisation basis.

Because optical concurrence is a mathematical analogue to quantum entanglement, it can be used to investigate this concept without having to actually generate entanglement or deal with any of the other problems that come from quantum measurement, which will be touched upon in chapter 4. But to measure the concurrence of a beam, a vector beam must first be created.

From a theoretical perspective, this has been a fairly comprehensive overview of the generation and properties of vector beams. But this is an experimental thesis. It is time to take this to the lab.

2.2.2 how to structure a beam

Most lasers generate a homogeneously polarised Gaussian beam. To turn it into a vector beam, its spatial intensity and polarisation distribution need to be altered. All methods of doing this can be loosely sorted into two camps: static devices that turn a Gaussian beam into the desired vector beam, and dynamic, programmable devices, which separately shape beams of orthogonal polarisations into different modes of propagation that are then combined.

The most notable device in the former category is the q-plate [24, 25], or vortex retarder, whose Jones matrix was shown as an example in equation 1.32 of chapter 1.2. It functions like a HWP with spatially varying orientation. The periodicity is given by the q-plate's characteristic m number. The beam generated by the q-plate depends on the input polarisation: an $|R\rangle$ or $|L\rangle$ polarised Gaussian mode will become a LG_0^1 or LG_0^-1 beam after transmission through a m=1 q-plate, respectively. Any linear polarisation is an equal superposition of $|R\rangle$ and $|L\rangle$, with the orientation given by the relative phase. Therefore, any linearly polarised Gaussian mode must be turned into a vector beam by the same q-plate. Vertically polarised light yields a radial beam, and horizontally polarised light an azimuthal one. Q-plates with higher m generate higher order LG modes, with $|\ell| = |\mathrm{m}|$. Reversing the q-plate inverts the m number and therefore the relationship between circular basis and ℓ sign.

There are other devices in this category, such as the Fresnel cone [44], or metasurfaces [45, 46], but they will not be discussed in this thesis. The advantage of this type of device is its ease of use and its high conversion efficiency, but it comes at the cost of it only being able to generate a very limited selection of beams.

The latter method does not have such problems. It makes use of programmable light shaping devices like spatial light modulators (SLM) or digital micromirror devices (DMD) [47, 48]. Expanded Gaussian beams of orthogonal polarisation bases independently interact with a multiplexed hologram on the element's screen, which functions as a programmable grating, and independently shapes the orthogonal components of the beam into the shape of the desired mode. Small differences in reflection angle allow the orthogonal beams to be combined, and the vector beam to be

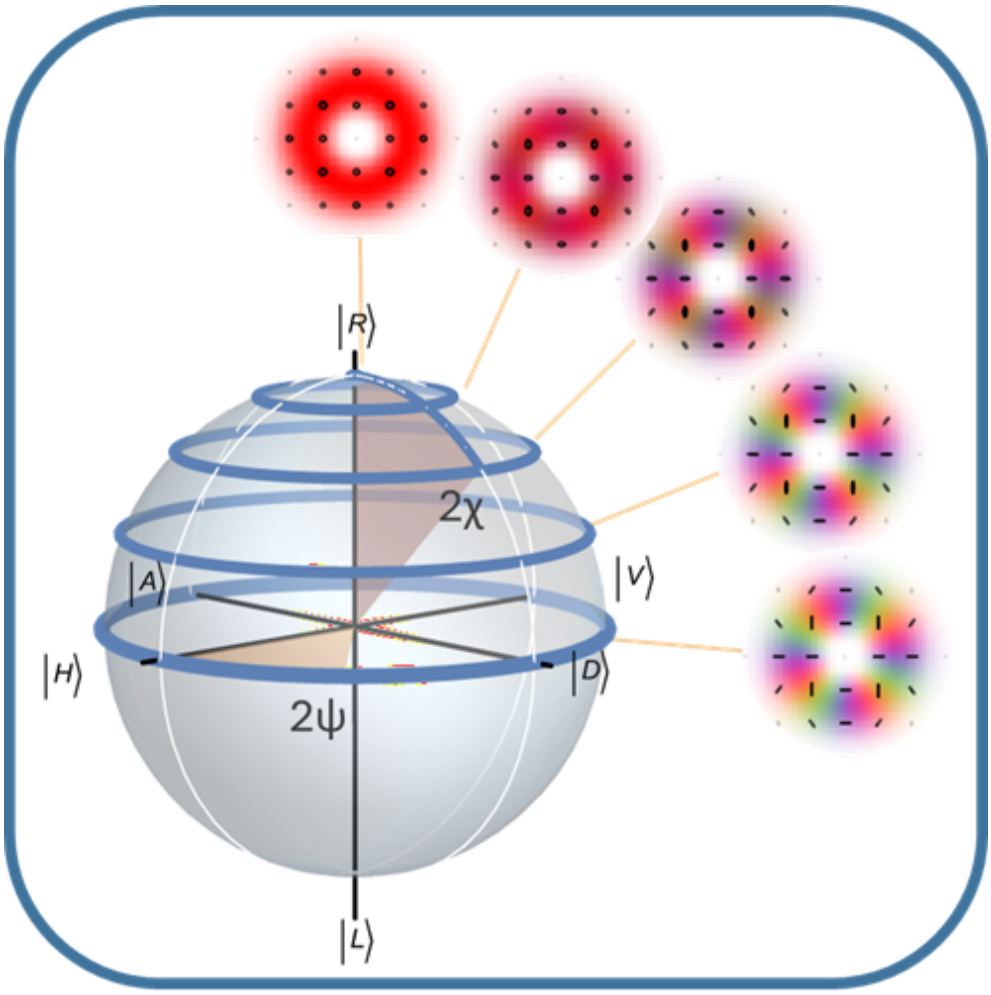

Figure 2.8: Trajectories of vector beams on the Poincaré sphere. The size of the circle directly corresponds to the correlation between azimuthal angle φ and polarisation state. Due to the choice of beams, it also correlates to the polar angle χ.

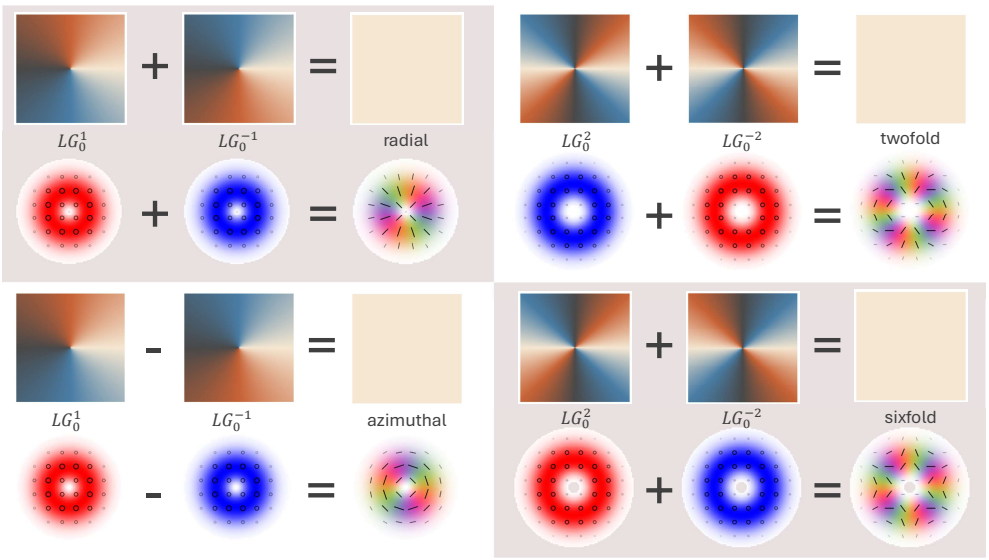

Figure 2.9: Creating structured beams from circularly polarised LG modes with opposite OAM. Note that the relative phase between the modes matters, as well as the sign for the OAM of each beam. The structured beams have uniform phase and no longer carry OAM.

generated. The obvious advantage of this approach is the generality - any shape of beam can be created, it is not even limited to the eigenmodes of propagation, but light shaping devices are often difficult to align and incredibly lossy, with efficiencies usually lower than 10% [49]. The best method therefore depends on the context of its use.

Once the beam has been generated, it can be measured. Though this, too, isn't straightforward.

2.3 Stokes polarimetry

IN WHICH AN OVERVIEW OF THE CONCEPT AND METHODS OF THE MOST COMMON FORM OF POLARIMETRY IS PROVIDED, ALSO MUELLER MATRIX MEASUREMENTS

So far, a lot of discussion has gone into the creation of different structures of light beams, but nothing about their measurement. As polarisation is a phase dependent property, a single measurement won't suffice. Instead, series of measurements will have to be performed. The Stokes vector contains all necessary information to recreate the coordinates on the Poincaré sphere, and an experimental Stokes vector can be calculated from measurements in each of the Stokes bases. If the beam in ques-

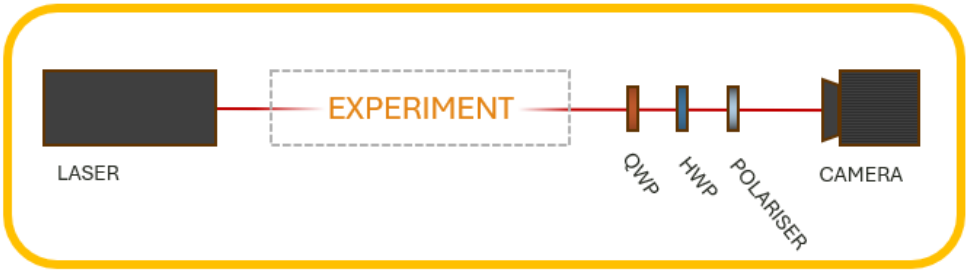

Figure 2.10: Experimental setup for Stokes polarimetry. The polariser is always vertical, while the wave plates are altered. Using a camera makes it possible to calculate a Stokes vector for each pixel.

tion is spatially structured, the measurements can be performed with a camera, and a Stokes vector evaluated for each pixel. Stokes polarimetry can be achieved in multiple ways:

1. Spatial splitting: The beam is split into six paths, separating the stokes bases and measuring them with separate detectors, e.g. different photodiodes or different areas of a camera [17, 50]. This method leads to issues at low beam intensities but has the advantage of the measurements being simultaneous. An unconventional approach to this is the subject of chapter 4.

2. Temporal modulation: Projective measurements into each of the stokes bases are performed in succession, usually with the same photodetector or camera. This approach is very common. Figure 2.10 shows the rotating wave plate approach, which is a popular setup for achieving this - variations thereof are used in nearly every experimental chapter of this thesis [51]. The wave plates change the bases of the beam, so that the polariser can project the beam into every basis, using the following fast axis alignments [17]:

	$\|H\rangle$	$\|R\rangle$	$\|V\rangle$	$\|L\rangle$	$\|A\rangle$	$\|D\rangle$
QWP	0°	0°	0°	0°	45°	45°
HWP	0°	22.5°	45°	67.5°	67.5°	22.5°

This approach is very good for data analysis, because the beam does not significantly move on the camera if the waveplates are properly aligned, so a Stokes vector can be calculated for each pixel. It is therefore the most commonly used variant of the work in this thesis.

Other approaches encode information into other degrees of freedom, such as wavelength, making it possible to carry out multiple stokes measurements simultaneously. Further methods still rely on known spatial dependence [17, 44, 52–56].

Of course, Stokes measurements measure the beam the way it arrives at the camera. But if the initial beam is known (most lasers produce a vertically polarised Gaussian beam), and the final beam is known, it can be possible to reconstruct how it has been altered. Especially with the relationship between the Stokes vector and the Mueller matrix, it is possible to gain some information about the system in the process.

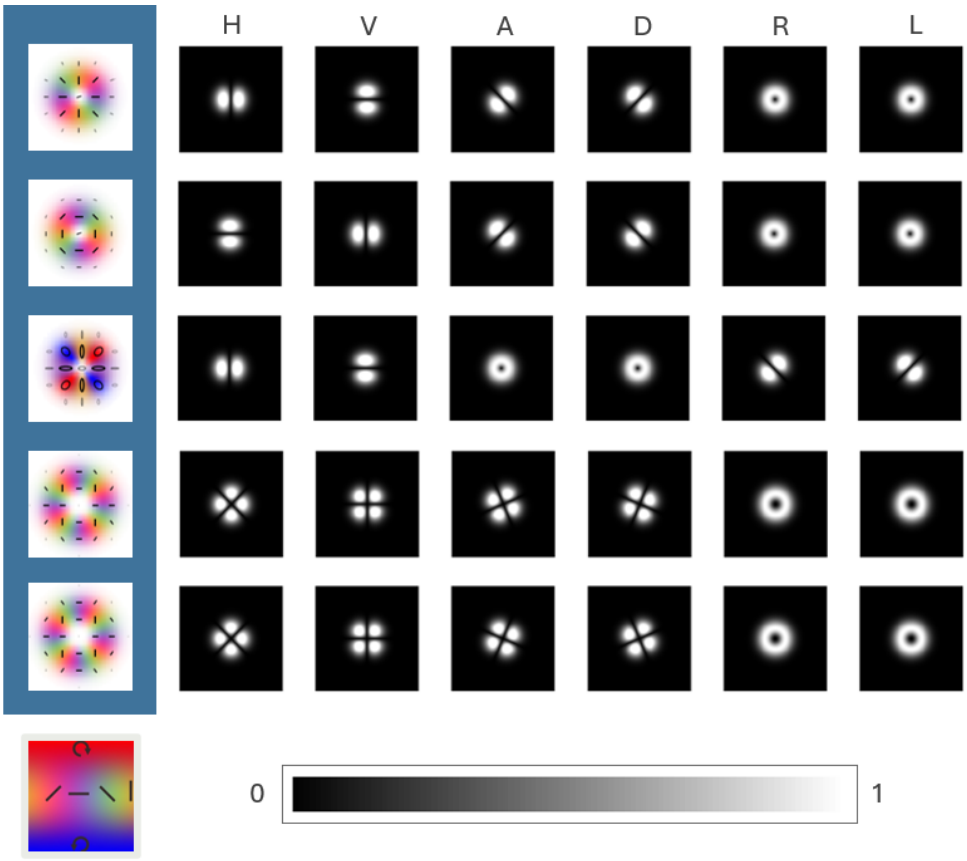

Figure 2.11: Stokes bases of a selection of structured beams. From top to bottom, the beams are: radial, azimuthal. hybrid, twofold, sixfold. On the left is the overall polarisation structure, displayed in the polarisation colour map (bottom left). In each column on the right is the simulated projection of the beam in the indicated polarisation basis state. The greyscale colour bar is used to visualise the spatially dependent intensity.

2.3.1 Mueller matrix polarimetry

An optical element is defined as anything that alters the beam's intensity, phase, frequency, timing, or polarisation. Any optical element can be described as a Mueller matrix. The Mueller matrices of most commonly used optical devices are well known, and a selection can be found in chapter 1.4.1, though if investigating the optical properties of an unknown object such as a biological sample [57–60], the Mueller matrix becomes what the experiment seeks to measure.

In order to fully understand how the element in question interacts with polarisation, one might think to probe it with a beam of each Stokes basis state, and then measure how it has been altered with a Stokes measurement [42, 61]. This process requires 32 consecutive measurements - twice as many as elements in the matrix! So 16 measurements should suffice, theoretically.

In the process of reducing the number of measurements, one might consider whether the sample is optically homogeneous. If it is, then it is possible to probe it with multiple polarisations at the same time. A vector beam with spatial polarisation structure lends itself to this, particularly one that features every polarisation on the Poincaré sphere [62]. In that case, the number of necessary measurements has been reduced to a single set of Stokes measurements. The absolute minimum of necessary camera images, however, will be discussed in chapter 4.3 - after a necessary detour over measurement theory.

3 longitudinal polarisation states

As mentioned in chapter 2, the plane wave does not exist. A beam does not extend infinitely into space. To deal with this, the Gaussian beam was introduced, which brought with it the curved phase fronts of the Gouy phase, but these just highlight another problem: Polarisation is not confined to the xy-plane.

Consider once again a beam focussed by a lens. The propagation axis of the beam is unaltered, but the local $\vec{k}$ vectors become spatially dependent, they now all point towards the focus. The further from the propagation axis, the stronger the tilt. The oscillation of the electric field is still transverse, but to the local wave vector $\vec{k}$. If the local polarisation is azimuthal, that is to mean transverse to the vector pointing out radially from the propagation axis (see chapter 2.2), the electric field will continue to be transverse. However, if the local polarisation is radial, the electric field is now partially aligned with the propagation axis. It has gained a longitudinal component [5].

This might not come as a surprise to some areas of optics - in some media, e.g. optical fibres, longitudinal polarisation is the norm [63]. This, however, is longitudinally polarised light in free space.

This change to the electromagnetic field distribution changes its very shape, to the point where it alters the focussing properties of the beam [64–69], the strong longitudinal polarisation component of a previously radial beam as described in chapter 2 allows it to be focused beyond the conventional diffraction limit [**youngworth2000focusing**, 70]. These properties give it many applications, including superresolution imaging, [71, 72], the generation of optical chains or needles [57, 73], as well as using them to investigate chiral materials [74] and nano-plasmonics [75, 76].

But to understand longitudinally polarised light, one must first shift into a suitable basis. Much theoretical work has been done surrounding three dimensional polarisation since the initial work by Richards and Wolf using vectorial diffraction theory [5], investigating various aspects of the fields [77–79]. It was learned that longitudinal polarisation can lead to light acquiring SAM in the tranverse direction [80–82], or that a potential state space can be mapped onto a generalised Poincaré sphere, which is also capable of describing effects like the directional emission by arbitrarily oriented molecules [83]. The latter, while being a very detailed and complete model, requires the use of an eight-dimensional Stokes vector analogue. For the purpose of the work presented here, it is better to work in its Jones vector equivalent.

3.1 even more Jones vectors

IN WHICH THE FINAL JONES BASIS AND THE THIRD JONES PARAMETER ARE INTRO-

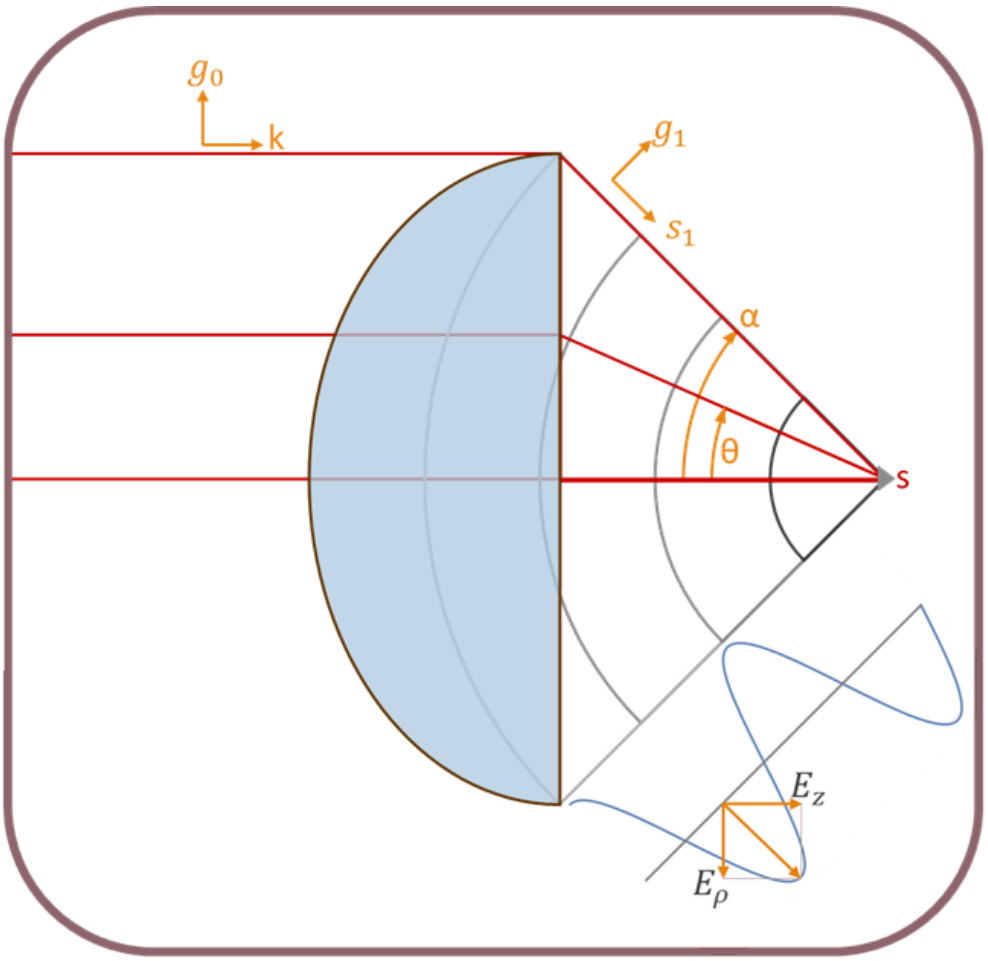

Figure 3.1: Focusing a beam with a lens tilts the phase fronts of the electric field toward the propagation axis, leading it to gain a longitudinal component. As the radius of the beam increases, the tilt becomes stronger. This is best expressed in spherical polar coordinates, with the focus at the centre. Here, g_0 and g_1 are the directions of electric field (assuming an initial radially polarised beam), s_1 points to the focus, θ is the polar angle in spherical polar coordinates, with a maximum of α which is the focusing angle of the beam, and given by the numerical aperture.

DUCED

In chapter 1.5.1, alternative Jones bases were introduced. Any set of orthogonal polarisations can serve as a Jones basis. It is now time to reveal the final set of basis states used in this thesis: radial and azimuthal. These bases are spatially dependent, but orthogonal at each point in space and as a whole.

This becomes more clear when a focussed beam is considered: If the lens is properly aligned, the propagation direction is unaltered, but the local wave vector is not, the beam shape changes, it becomes smaller, the wave vector points towards the focus, and the wave vector is what the polarisation is perpendicular to. Radial and azimuthal beams have been introduced in chapter 2, and the fact that they are orthogonal comes to fruition here. Now, the azimuthal polarisation angle matters a great deal because if the local polarisation is azimuthal, it will remain transverse to the propagation axis, like you'd think it would, but if the local polarisation is radial, the electric wave will tilt inward towards the focus - it gains a longitudinal component. Therefore it makes sense to move into an unusual basis for this consideration. Any polarised beam can be decomposed into its radial and azimuthal components. This can be done as follows:

$$E_\varphi(z) = \cos\varphi_s E_y(z) - \sin\varphi_s E_x(z) \tag{3.1}$$
$$E_\varrho(z) = \cos\varphi_s E_x(z) - \sin\varphi_s E_y(z), \tag{3.2}$$

where z is the propagation direction, x and y are the coordinates in the transverse plane, $\varphi = \tan^{-1}(y/x)$ is the polar azimuthal angle and so E_φ and E_ϱ are the azimuthal and radial electric fields, respectively. The radius ϱ that would complete the polar coordinates is omitted here, as the beam is assumed to be radially symmetric.

When the Jones vector was initially introduced in chapter 1.2, only the transverse components were considered, as this chapter was working in the plane wave approximation. Now it is time to add the longitudinal E_z back into the vector:

$$\vec{E} = \begin{pmatrix} \tilde{E}_x \\ \tilde{E}_y \\ \tilde{E}_z \end{pmatrix} \tag{3.3}$$

or

$$\vec{E} = \begin{pmatrix} \tilde{E}_\varrho \\ \tilde{E}_\varphi \\ \tilde{E}_z \end{pmatrix}. \tag{3.4}$$

Of course, in the paraxial limit, $E_z \approx 0$, and can be safely omitted. This notation should provide a sufficient toolkit for the next step on the path to creating longitudinally polarised light.

3.2 strongly focused light

IN WHICH LIGHT IS PUT THROUGH A LENS, AS DESCRIBED BY RICHARDS AND WOLF IN [5], AND EXPANDED ON BY YOUNGWORTH ET AL IN [84]

One final parameter needs to be introduced before the beam can be put through a lens: the unit vector $\vec{g}$, which points radially outward from the optical axis:

$$\vec{g}_0 = \cos\varphi\,|H\rangle + \sin\varphi\,|V\rangle\,. \tag{3.5}$$

By definition, azimuthally polarised light has an electric field in the direction $\vec{g}\times\vec{k}$, so the beam can now also be written as

$$\vec{E}_0 = l_0[E_\varrho^{(0)}\vec{g}_0 + E_\phi^{(0)}(\vec{g}_0 \times \hat{\vec{k}})]. \tag{3.6}$$

In their 1959 paper [5], Richards and Wolf showed that the electric field of a focused beam can be expressed via a diffraction integral over the vector field amplitude $\vec{a}_i$. To best represent this, a change of coordinate system is necessary: The beam is now considered to sit in a spherical polar coordinate system characterised by radius s, polar angle θ and azimuthal angle φ, with the origin being at the focus. The beam can now be visualised to occupy a circular segment of a sphere, and, if the beam is azimuthally symmetric in intensity (like an LG mode) its radius is given by a constant θ, i.e. its area becomes smaller as it is focussed. Note that the φ has the same meaning here as it did before, it describes the azimuthal angle on the beam. See figure 3.1 for an illustration of these angles. In this configuration, the equation for the electric field is as follows:

$$\begin{pmatrix} E_x(s) \\ E_y(s) \\ E_z(s) \end{pmatrix} = -\frac{iA}{\pi}\int_0^\alpha\int_0^{2\pi} E_0(\theta)\sin\theta\sqrt{\cos\theta} \\ \exp[ik(z_s\cos\theta + \varrho_s\sin\theta\cos(\varphi-\varphi_s)]\begin{pmatrix}\cos\theta\cos\varphi\\ \cos\theta\sin\varphi\\ \sin\theta\end{pmatrix} d\phi d\theta. \tag{3.7}$$

The Cartesian components can now be transformed into the radial-azimuthal basis using equation 3.1. As mentioned in the introduction of this chapter, the azimuthal component will not be affected by focusing, so it can be safely discarded for now. Setting it to 0 is equivalent to using a radially polarised beam. Consider now the full form of the radial and longitudinal component [84]:

$$E_\varrho(s) = -\frac{iA}{\pi}\int_0^\alpha\int_0^{2\pi} l_0(\theta)\sin\theta\sqrt{\cos\theta}\cos\theta\cos(\phi-\phi_s) \exp[ik(z_s\cos\theta+\varrho_s\sin\theta\cos(\phi-\phi_s)]d\phi d\theta \tag{3.8}$$

$$E_z(s) = -\frac{iA}{\pi}\int_0^\alpha\int_0^{2\pi} l_0(\theta)\sin\theta\sqrt{\cos\theta} \exp[ik(z_s\cos\theta+\varrho_s\sin\theta\cos(\phi-\phi_s)]d\phi d\theta. \tag{3.9}$$

Various papers have analytically carried out partial integration over φ, but solutions using ϱ and θ have to be done numerically [83]. In this thesis all theoretical results come from numerical simulations. Of particular interest here is the effect of beams with a spatially dependent radial component - at the focus, the intensity distribution between longitudinal and transverse polarisation components becomes spatially dependent. This leads to especially interesting structures when viewed in more traditional bases, like shown in figure 3.2.

A problem with longitudinally polarised light is that despite its many applications, it cannot be picked up by traditional cameras, or even photodetectors. All previous attempts of measuring it relied on indirect methods, such as suppressing the forward scattering when gold nanoparticles were illuminated by radially polarised light [85], using the fluorescence patterns of single molecules with fixed absorption dipole moments to infer the scattering [86, 87], interaction with molecular monolayers [88], or using Mie scattering of microscopic particles to reconstruct the 3D light field [89, 90].

The first direct measurement of the E_z component can be found in chapter 9 of this thesis.

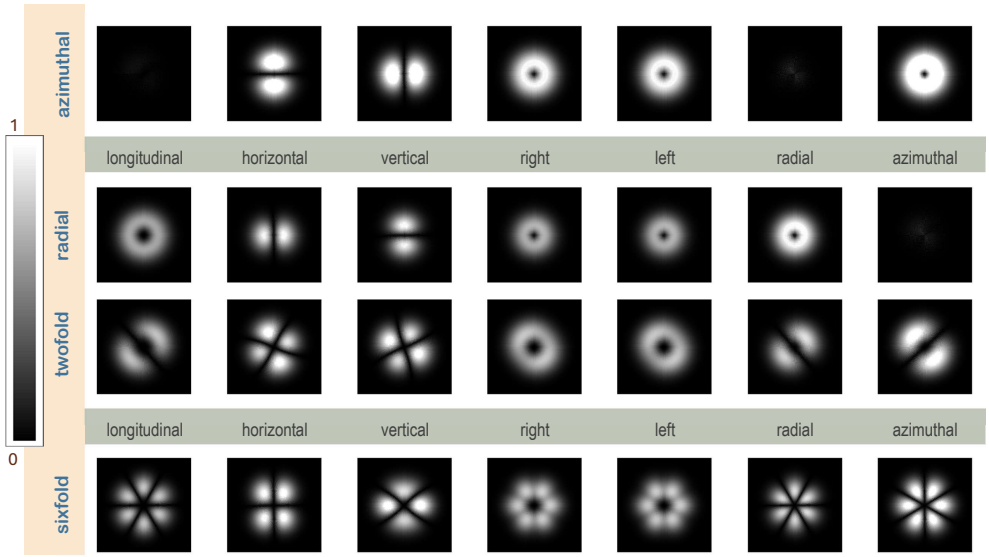

Figure 3.2: Using different bases to describe the three dimensional polarisation structure of a strongly focused beam. On the left is the longitudinal polarisation, the rest are orthogonal paraxial bases in pairs: horizontal and vertical, right and left, radial ad azimuthal. The relative benefits become apparent depending on the use case: horizontal-vertical is the most conventional and intuitive basis, while radial-azimuthal is most visibly related to the longitudinal component, and right-left is useful here to show that they are linearly polarised beams, but also useful later, as they are the other eigenstates of the medium that will measure the longitudinal component in chapter 9.

4 POVMs: measurements and information

Cameras and photodetectors measure transverse intensity. This throws a wrench into any measurement of non-paraxial polarisations (so one has to result to methods like the one described in chapter 9), but it also makes it difficult to measure paraxial polarisations. The smallest amount of parameters that can be used to describe a paraxial beam of light are its amplitude in two orthogonal directions as well as a relative phase, so a single measurement does not suffice. In chapter 2.3, the Stokes measurement was introduced to solve this issue: A measurement taken in 6 basis states, forming three pairs of mutually unbiased pairs of orthogonal states ($|H\rangle, |V\rangle, |A\rangle, |D\rangle, |R\rangle$ and $|L\rangle$) allows for full reconstruction of the Stokes vector. But what is it that makes this kind of measurement work? And what are the alternatives?

4.1 measurement theory

WHICH CONCERNS ITSELF WITH THE PROCESSES OF MEASUREMENT, AND IS TAKING HEAVILY FROM [91], PROVIDING AN IMPORTANT STEP ON OUR QUEST TO SINGLE SHOT POLARIMETRY.

To find an answer, one must turn to quantum theory. **Projective measurements** destroy the information being measured to obtain specific data - "are you one thing or not? Do you have this characteristic?" They can only ask yes or no questions [92]. Superposition states yield probabilistic results, though in measuring many individual particles classical behaviour can be observed once again. The process of projective measurement can be described by an eigenvalue equation, as discovered by J. Von Neumann in 1955 [93]:

$$\hat{A}\,|\lambda_i\rangle = \lambda_i\,|\lambda_i\rangle\,, \tag{4.1}$$

with the operator $\hat{A}$ being the projective operator, and the outcomes λ_i are eigenvalues describing the probabilities that correspond to the eigenstates $|\lambda_i\rangle$. The probability distribution P comes from the density operator $\hat{\rho}$:

$$P(\lambda_i) = Tr(\hat{\rho}\hat{P}_i) \tag{4.2}$$

The **density operator**, or density matrix, is a n$\times$n matrix holding the probability distribution of a n dimensional state space. For a 2 level system, it looks like this:

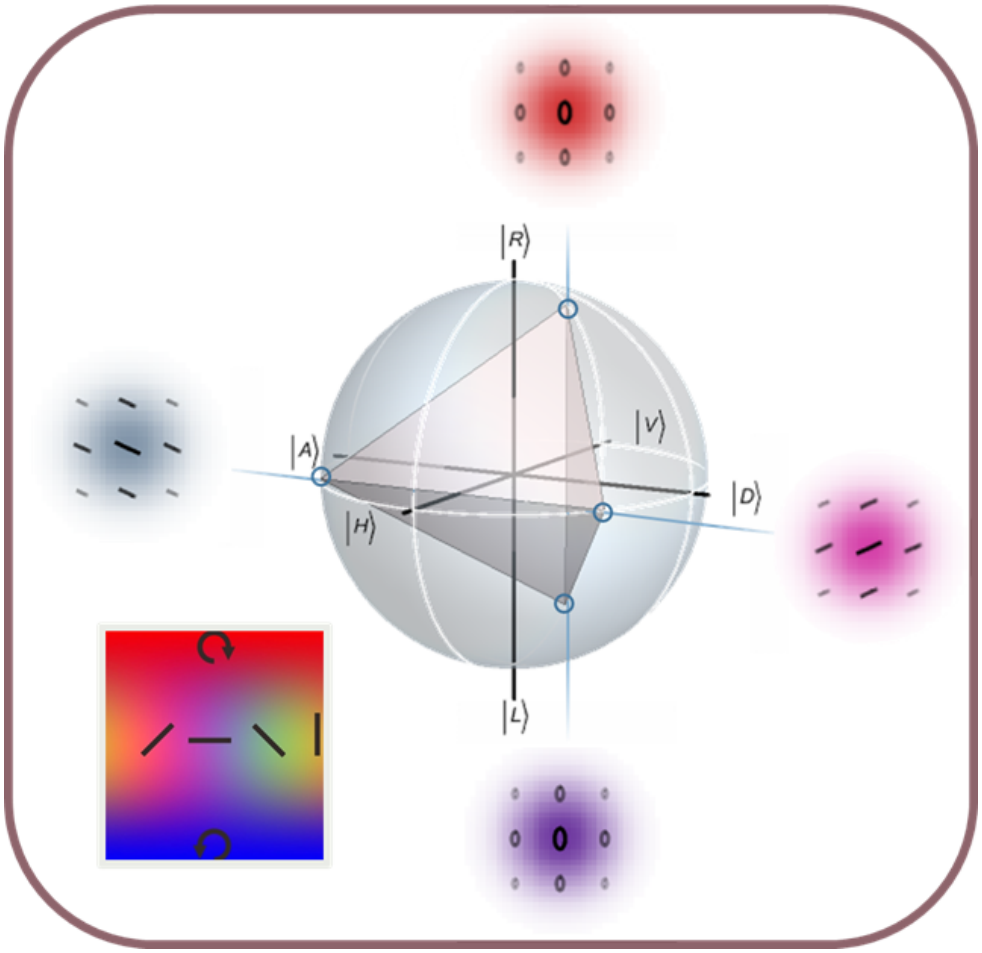

Figure 4.1: POVM states on the Poincaré sphere form a tetrahedron. Two states are linearly polarised and sit on the equator, while the remaining two are points on an orthogonal grand circle. these two states share an orientation but have opposite ellipticity.

$$\hat{\rho} = \begin{pmatrix} \rho_{11} & \rho_{12} \\ \rho_{21} & \rho_{22} \end{pmatrix}. \tag{4.3}$$

This operator is generally time and spatially dependent. Its diagonal elements ρ_{11} and ρ_{22} describe the probabilities of the object being in state 1 or 2 respectively, and $\rho_{12} = \rho_{21}^*$ the complex probability amplitude of hopping between the states. The density operator will be revisited in chapter 6.3.2.

The probability operator from equation 4.2 can be described as a set of projectors

$$\hat{P}_i = |\lambda_i\rangle \langle\lambda_i| . \tag{4.4}$$

Projectors by definition need to be Hermitian, positive, complete, and orthonormal [91]. The reasoning behind this is as follows: projectors represent observables, and are therefore naturally hermitian ($\hat{P}_n^\dagger = \hat{P}_n$). Probabilities are scalars and therefore positive, hence $\hat{P}_n \geq 0$. Probabilities also cannot sum to numbers greater than one, so the set of projectors has to be complete: $\sum_n \hat{P}_n = \hat{I}$. A choice of orthonormal measurement states ensures intuitive interpretability, as the the states are defined to be mutually exclusive, so $\hat{P}_i\hat{P}_j = \hat{P}_i\delta_{ij}$, where δ_{ij} is the Kronecker delta. Two sets, each containing two orthogonal projectors, are considered to be a mutually unbiased basis (MUB) if any projector can be expressed as an equal superposition of the other pair [17].

It is easy to see that a Stokes measurement fulfils all of these criteria - the first three emerge naturally, and each Stokes parameter is calculated from a set of MUBs. The Poincaré sphere does not correspond to physical 3D space, instead orthogonal basis pairs are found on the opposite ends of each axis. In this space, the six Stokes vectors form the corners of an octahedron, more than enough to define it: A state in a Hilbert space with d dimensions requires d^2 measurements to be fully reconstructed, so in this case four should be enough [94]. Much like any two-dimensional surface can be defined by three points on it, a three-dimensional space, or even a sphere can be defined by four points. Four measurements should suffice. [95–97]

POVM stands for **positive operator value measurement**. Theoretically, it is an umbrella term that includes projective measurements, but it is colloquially used to refer to measurements using non orthogonal basis states. The three natural rules of projective measurements still apply, POVMs have to be Hermitian, positive, and complete, but of course orthonormality is no longer a condition [91]. This loosens restrictions on the number of measurements, their minimum being the smallest number necessary to characterise the Hilbert space [92]. POVM operators are denoted as $\hat{\pi}$.

4.1.1 POVM on the Poincaré sphere

Four distinct polarisation states correspond to four points on the surface of the Poincaré sphere. As a sphere can be defined by any four distinct points on its surface, these polarisations could theoretically be chosen arbitrarily, but the closer they are to one another, the more vulnerable measurements become to noise. Areas of the Poincaré sphere with fewer states on them will always have bigger uncertainties than those with more states in proximity, so the most general configurations sees all states with equal distances to one another [98].

When evenly spaced out, the four states necessary to define the Poincaré sphere form a tetrahedron [99, 100]. Each of its corners corresponds to a polarisation, the measurement of all four constitutes full tomography. The orientation of the tetrahedron is arbitrary. To optimise for convenience and interpretability, states were chosen that depend on the parameters a and b:

$$a = \sqrt{\frac{1}{2} + \frac{1}{2\sqrt{3}}}, \qquad b = \sqrt{\frac{1}{2} - \frac{1}{2\sqrt{3}}}, \tag{4.5}$$

which are used to define the following states:

$$|\phi_1\rangle = a\,|H\rangle + b\,|V\rangle \tag{4.6}$$
$$|\phi_2\rangle = a\,|H\rangle - b\,|V\rangle \tag{4.7}$$
$$|\phi_3\rangle = b\,|H\rangle + ia\,|V\rangle \tag{4.8}$$
$$|\phi_4\rangle = b\,|H\rangle - ia\,|V\rangle\,. \tag{4.9}$$

Now, two of the tetrahedron's states lie on the equator of the Poincaré sphere, making them linear, and the other two on the grand circle crossing it at $|V\rangle$, i.e. they are vertically elliptical. Figure 4.1 shows the four polarisations and the tetrahedron. In Poincaré coordinates, the states are the following:

$$|\phi_1\rangle \to 2\chi = \pi/2, 2\psi = 0.9553 \tag{4.10}$$
$$|\phi_2\rangle \to 2\chi = \pi/2, 2\psi = -0.9553 \tag{4.11}$$
$$|\phi_3\rangle \to 2\chi = 0.9553, 2\psi = \pi \tag{4.12}$$
$$|\phi_4\rangle \to 2\chi = -0.9553, 2\psi = \pi. \tag{4.13}$$

The difficulty using the POVM basis is that the experimental setup would require projection into non-orthogonal basis states: In [101], a potential experimental setup was proposed that uses a partially polarising beam splitter, with a 1/3 vs 2/3 distribution of states. This means that, without affecting the phase between the polarisation states, one arm of the beam splitter transmits 1/3 of $E_{x,0}$ and 2/3 of $E_{y,0}$, and the other one will do the opposite. This can be easily misunderstood, as a polarising beam splitter placed at an angle of 60° would separate $|H\rangle$ and $|V\rangle$ along these proportions, though it does not meet the assignment. It is important to stress here that this is irrespective of phase, it cannot fully separate the beam in another basis; the beam splitter must have a specific basis by which it sorts the polarisation but not do so fully. Unfortunately, such devices are not readily available, they must be custom made, making them very expensive. But through interferometry, everything is possible.

4.2 non-orthogonal polarimetry using interferometry

THIS CHAPTER OUTLINES THE FIRST EXPERIMENTAL REALISATION OF POVM POLARIMETRY DONE BY TWO FORMER PHD STUDENTS OF THE OPTICS GROUP: MUSTAFA

A. AL KHAFAJI [100] AND AMY MCWILLIAM [2]. I AIDED THE LATTER IN THE DEVELOPMENT AND MAINTENANCE. THE EXPERIMENT WAS CONCEPTUALISED BY SONJA FRANKE-ARNOLD, SARAH CROKE AND SEBASTIAO PADUA. THIS IS ALSO WHERE THE CURRENT EXPERIMENTAL SETUP IS DISCUSSED IN DETAIL

In section 4.1.1 of this chapter, it was shown that any beam can be characterised using strategic measurements of four non-orthogonal polarisation states, but that to do so experimentally requires a $\frac{1}{3}$ vs $\frac{2}{3}$ **partially polarising beam splitter** (PPBS), which is commercially unavailable.

A **Mach-Zehnder interferometer** can be used to yield the results of a generic PPBS, with full control over the proportions of component polarisations. This setup can be seen in figure 4.2A and has an output of

$$\vec{E}_{\text{out,1}} = \begin{pmatrix} -E_{H,\text{in}} \sin(2\alpha) \\ E_{V,\text{in}} \sin(2\beta) \end{pmatrix} \tag{4.14}$$

$$\vec{E}_{\text{out,2}} = \begin{pmatrix} E_{H,\text{in}} \cos(2\alpha) \\ -E_{V,\text{in}} \cos(2\beta) \end{pmatrix}, \tag{4.15}$$

where α and β are the angles of the HWPs in each of the arms.

In [100], this PPBS was used as the centrepiece of a polarimeter. Afterwards, the phase of each output was adjusted with a monorefringent quartz plate, and their polarisations altered with a QWP and HWP respectively, which allowed the now slightly misaligned paths to be projected into the bases from equation 4.18. A similar setup was used by Ling et al in a previous experiment, though they only measured homogeneous polarisations [102]. Sadly, Mach Zehnder interferometers are prone to misalignment, the three consecutive PBSs make the system highly unstable. The beams travel different paths, so noise such as air currents or vibrations might affect both beams unequally.

Before more research could be done, a more stable version had to be devised: A Sagnac interferometer with misaligned beam paths is effectively equivalent to a Mach-Zehnder interferometer that uses the same beam splitter twice. This principle was used to create the system in figure 4.2B. The difference in path lengths due to the nature of the experiment is compensated by the tilted glass slides in each arm of the interferometer. Slight change in alignment can be compensated by adjusting the effective optical path length. This improvement of stability was investigated in the first part of [2], in which the Sagnac setup was first used.

In both versions of the setup, readout occurs from a single camera image, allowing the polarimeter to measure changes in the experimental beam in real time. Figure 4.2C shows that each component polarisation occupies its own quadrant of the camera screen in clockwise order. While an equivalent configuration is theoretically also possible for measurements in the Stokes bases, camera space is limited, and the closer the beams are to each other, the larger the possibility of interference or cross talk. From each camera image, a four element vector describing the polarisation can be calculated:

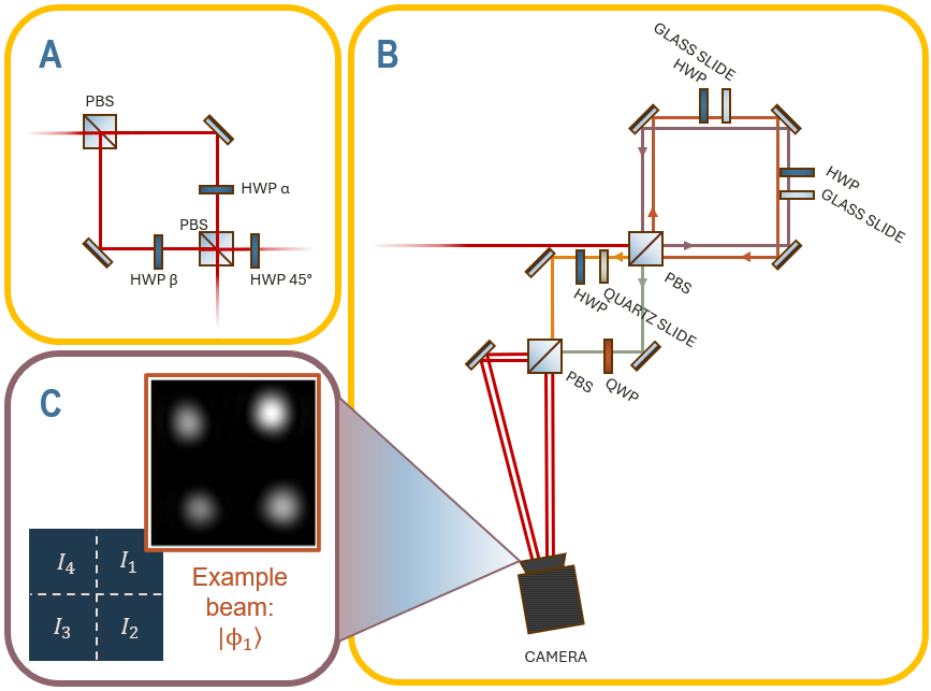

Figure 4.2: POVM experimental setup. A: Mach-Zehnder interferometer acting like a PPBS. HWP angles α and β make it possible to tune the fractions of the original beam in each arm. B: Current experimental setup using a modified Sagnac interferometer. The colour coding here does not indicate polarisation, it is intended to visualise the different beam paths. The glass slides have an adjustable tilt, making it possible to dynamically optimise the path difference. After the initial Sagnac interferometer, the beams are vertically displaced with respect to one another, so that the resulting beams can each occupy a different quadrant of the camera. C: The camera screen is divided into four regions, from which the states can be read out clockwise. In the orange box is an experimentally obtained image of beam $|\phi_1\rangle$. The intensity distribution shows that I_1 is at its maximum, while the remaining intensities are equal and lower, but still present.

$$\vec{I}^{(N)} = \begin{pmatrix} I_1 \\ I_2 \\ I_3 \\ I_4 \end{pmatrix} / I_t, \tag{4.16}$$

where I_n is the intensity in the relevant mode and I_t is the total intensity $I_t = \sum_{i=1}^{i=4} I_i$. The states have significant overlap with one another, making the POVM vector unintuitive to read, but it can be transformed into a Stokes vector via the instrumentation matrix

$$\Pi = \frac{1}{4} \begin{pmatrix} 1 & \sqrt{\frac{1}{3}} & \sqrt{\frac{2}{3}} & 0 \\ 1 & \sqrt{\frac{1}{3}} & -\sqrt{\frac{2}{3}} & 0 \\ 1 & \sqrt{-\frac{1}{3}} & 0 & -\sqrt{\frac{2}{3}} \\ 1 & \sqrt{-\frac{1}{3}} & 0 & \sqrt{\frac{2}{3}} \end{pmatrix}. \tag{4.17}$$

Like done with Stokes previously in section 2.3, these measurements can be done spatially, by measuring them with a camera image and calculating the stokes measurements pixel by pixel.

The beams for this experiment are generated by a digital micromirror device (DMD), which was introduced in chapter 2.2.2. DMDs allow for the generation of nearly any beam. This will be useful for creating vector modes later, but now it is especially useful for the arbitrary control over polarisation states.

The camera image produced by the POVM setup is less intuitive to interpret than images produced by Stokes measurements. As the POVM states are not orthogonal, any polarisation will have an overlap with multiple of them. A POVM state, in particular, will produce a projection into all three other states in addition to the maximum projection into its particular state. This causes additional challenges for the optimisation of the system.

Before measurements, the interferometer has to be calibrated. Experimentally, it is easier to optimise for minimum intensity rather than maximum, so the system is probed with homogeneously polarised beams that are orthogonally polarised to each of the POVM states:

$$\left|\bar{\phi_1}\right\rangle = b\left|H\right\rangle - a\left|V\right\rangle \tag{4.18}$$
$$\left|\bar{\phi_2}\right\rangle = b\left|H\right\rangle + a\left|V\right\rangle \tag{4.19}$$
$$\left|\bar{\phi_3}\right\rangle = a\left|H\right\rangle - ib\left|V\right\rangle \tag{4.20}$$
$$\left|\bar{\phi_4}\right\rangle = a\left|H\right\rangle + ib\left|V\right\rangle. \tag{4.21}$$

Figure 4.3 shows that this removes the respective POVM state from the camera image, if the system is properly aligned. In other words, the optical path difference between the arms of the Sagnac interferometer needs to be adjusted until the beam in question vanishes.

In [100], it was shown that this provides a viable single shot alternative to the Stokes measurement, even for beams with complicated polarisation structures. But beams rarely change on their own - if it is being altered in real time, the focus of the research tends to be the optical element that alters the beam.

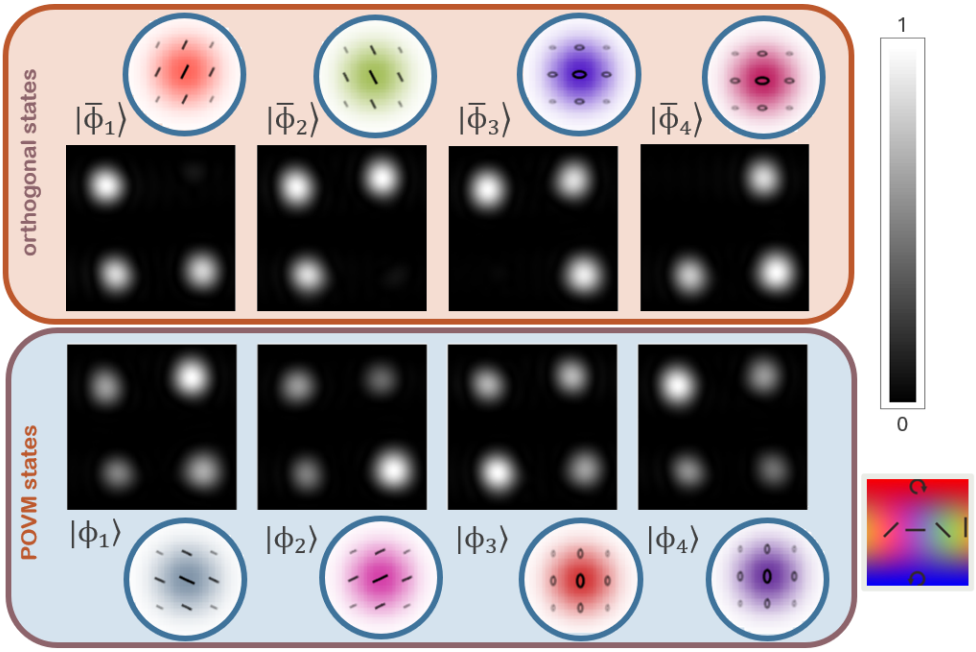

Figure 4.3: Using uniformly polarised beams to calibrate the POVM setup. The system is ready for measurements once the corresponding orthogonal projection fully disappears. Experimental data collected by Amy McWilliam, and adapted from [2]. Simulations of the probe beams by me.

4.3 generalised Mueller matrix measurements

THIS SECTION IS BASED ON THE PAPER "DYNAMIC MUELLER MATRIX POLARIMETRY USING GENERALIZED MEASUREMENTS" [2], THE FIRST EXPERIMENTAL PAPER I CONTRIBUTED TO DURING MY PHD. IT CONTAINS RESEARCH I DID ALONGSIDE AND UNDER THE GUIDANCE OF AMY MCWILLIAM, SEBASTIAO PADUA, AND SONJA FRANKE-ARNOLD. IN THIS PAPER, THE SHIFT FROM THE MACH-ZEHNDER INTERFEROMETER TO THE SAGNAC INTERFEROMETER WAS FIRST INTRODUCED AND ITS STABILITY INVESTIGATED. THE PRIMARY AIM, HOWEVER WAS THE SINGLE SHOT MEASUREMENTS OF MUELLER MATRICES. MY PRIMARY CONTRIBUTION, WHICH CONCERNED THE CHARACTERISATION OF A TILTED WAVE PLATE, HAS BEEN GIVEN ITS OWN SUBSECTION.

Any optical element has a 16 element Mueller matrix which describes its effect on the Stokes vector. They were first introduced in chapter 1.4.1 of this thesis as a largely theoretical concept, but in chapter 2.3.1, it was revealed that they can be measured using the six Stokes measurements, if the element in question is homogeneous. In order for this to work, the probe beam needs to feature every polarisation on the Poincaré sphere.

All information gained from a Stokes measurement can be gained from a single POVM image. In other words, [2] showed that it is possible to measure the Mueller matrix of an optically homogeneous sample from a single camera image, making it possible to monitor dynamic changes to the medium in real time.

The method for the experiment is the same that was used in chapter 4.2. The probe beam is generated by the DMD via superposition of Laguerre-Gauss modes, via the methods from chapter 2.2:

$$|\Psi\rangle = \frac{1}{\sqrt{2}}\left(LG_1^0|H\rangle + LG_0^2|V\rangle\right). \tag{4.22}$$

As the mode numbers of the component beams are the same, they have the same Gouy phase, and so their polarisation structure stays the same during propagation. Vector beams like this were previously introduced in chapter 2.

4.3.1 proof of principle and error analysis

In order to verify this method, initial measurements were taken of components with known Mueller matrices: A QWP and a HWP. Figure 4.4 shows the experimental beam before and after each component, with a selection of fast axis angles. Comparison to simulations of the beam after each component in question show that the measured effects on the polarisation are as anticipated.

Using the spatially dependent Stokes vectors describing the initial and final polarisation, the Mueller matrix of each element can be calculated. Figure 4.5 shows a graphical representation of the experimentally measured Mueller matrices plotted as solid bars, in comparison to the translucent bars showing the theoretical Mueller matrices from chapter 1.4.1. Their similarity validates this setup's ability to measure a Mueller matrix, but is it competitive?

The global error of the Mueller matrix elements can be calculated via the root mean square of the individual errors:

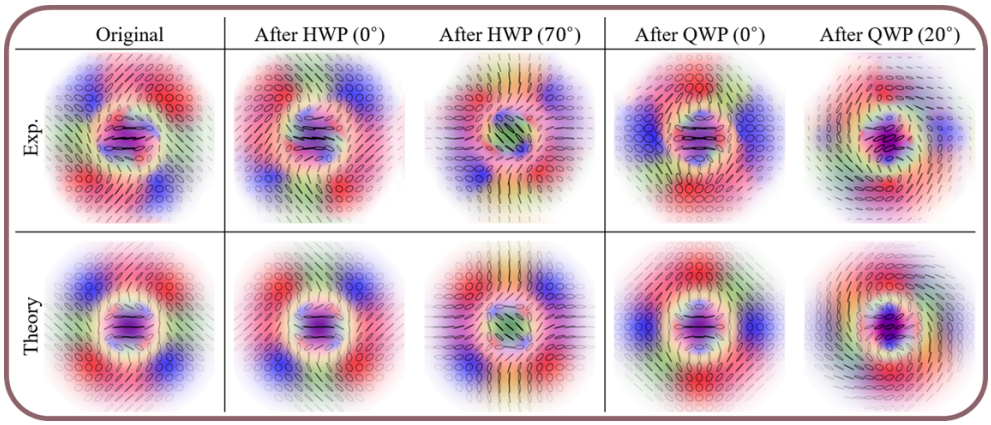

Figure 4.4: Experimental beam before and after a HWP at different fast axis angles. Figure taken from [2] and generated by Amy McWilliam.

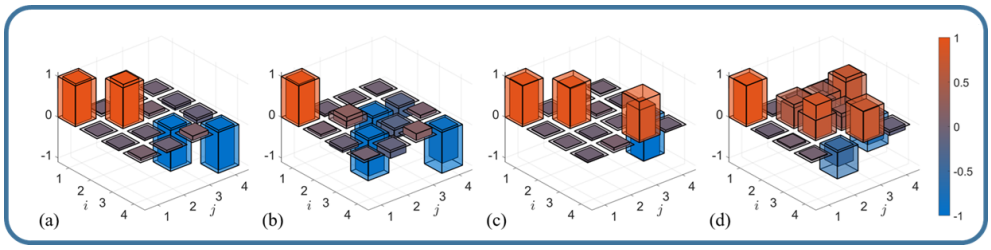

Figure 4.5: Theoretically (transparent) and experimentally (opaque) determined Mueller matrices. Each bar graph represents a Mueller matrix element $\hat{M}_{i,j}$. The elements are as follows: a) HWP at 0°, b) HWP at 70°, c) QWP at 0°, and d) QWP at 20° Figure taken from [2].

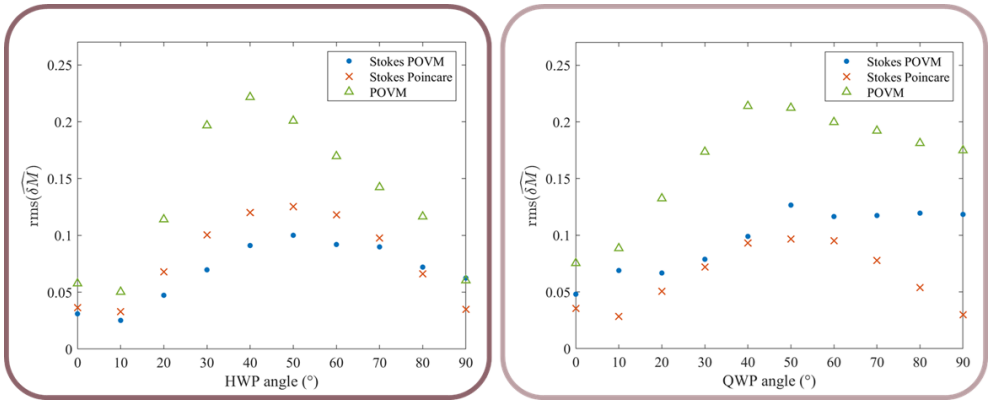

Figure 4.6: Root mean square as described in equation 4.23 of the individual errors on the Mueller matrix measurements. Three methods are being compared: The POVM Sagnac interferometer, standard Stokes polarimetry, and measurements obtained by using a Stokes setup to project into the POVM states. Figure adapted from [2], for which it was generated by Amy McWilliam.

$$rms(\delta\hat{M}) = \frac{1}{4}\sqrt{\sum_{i,j=1}^{4} |\delta M_{ij}|^2} \tag{4.23}$$

with $\widehat{\delta M} = \widehat{\delta M_E} - \widehat{\delta M_T}$ being the difference between the experimentally measured and theoretical Mueller matrices. The global errors are plotted as a function of fast axis angles in figure 4.6, and compared to equivalent results of two other methods: Conventional Stokes measurement as described in chapter 2.3, and using the same Stokes setup to project into POVM states.

As the POVM interferometer is much more complex than a Stokes setup, which consists of only three optical elements, it is unsurprising that there is a slight increase in error. However, these results show that the errors of the POVM measurements are within a factor of two of those of more conventional methods. The fact that the errors of all techniques seems to depend on the fast axis angle of the wave plates might suggest a slight tilt in the wave plate. This warrants further investigation.

4.3.2 nonstandard optical elements

A wave plate with a tilt has a different thickness relative to the beam axis. Wave plates are birefringent, so this results in a change in optical path difference and therefore phase retardance. Multi-order wave plates are designed to be used at normal incidence, and their theoretical retardance becomes nonlinear:

$$\delta_T(\theta,\alpha) = \frac{2\pi T}{\lambda}\left(\sqrt{n_e^2 - \frac{n_e^2\cos^2(\theta) + n_o^2\sin^2(\theta)}{n_o^2}\sin^2(\alpha)} - \sqrt{n_o^2 - \sin^2(\alpha)}\right), \tag{4.24}$$

where θ is the angle of the wave plates fast axis, α is the angle of incidence,

T is the thickness of the wave plate, n_o and n_e are the ordinary and extraordinary refractive indices and λ is the wavelength.

For a fast axis angle $\theta = 0°$, this equation simplifies to

$$\delta_T(\theta = 0, \alpha) = \frac{2\pi T}{\lambda}\left(\sqrt{n_e^2\left(1 - \frac{\sin^2(\alpha)}{n_o^2}\right)} - \sqrt{n_o^2 - \sin^2(\alpha)}\right). \tag{4.25}$$

The Mueller matrix for a wave plate with retardance δ and fast axis angle $\theta = 0°$ is

$$M(\delta, \theta = 0) = \begin{pmatrix} 1 & 0 & 0 & 0 \\ 0 & 1 & 0 & 0 \\ 0 & 0 & \cos\delta & -\sin\delta \\ 0 & 0 & \sin\delta & \cos\delta \end{pmatrix}. \tag{4.26}$$

This means there are four ways to calculate the retardance from a measured Mueller matrix:

$$\delta_1 = \tan^{-1}\left(-\frac{M_{34}}{M_{33}}\right) \tag{4.27}$$

$$\delta_2 = \tan^{-1}\left(-\frac{M_{34}}{M_{44}}\right) \tag{4.28}$$

$$\delta_3 = \tan^{-1}\left(\frac{M_{43}}{M_{33}}\right) \tag{4.29}$$

$$\delta_4 = \tan^{-1}\left(\frac{M_{43}}{M_{44}}\right). \tag{4.30}$$

To show that the setup is capable of measuring general phase retardance, a multi-order crystalline QWP (ThorLabs WPMQ05M-633) was mounted on a rotation stage to measure the Mueller matrix as a function of tilt angle.

Although all four retardances should theoretically be the same, there are slight discrepancies due to experimental errors. Their average values in dependence of tilt angle are displayed in figure 4.7, plotted against an experimental fit. Substituting the fitted curve back into equation 4.25, the refractive indexes of the wave plate can be calculated:

$$n_o = 1.54302 \pm 0.00032 \tag{4.31}$$

$$n_e = 1.55199 \pm 0.00033 \tag{4.32}$$

Thorlabs provides these values to four significant figures: $n_o = 1.543$ and $n_e = 1.552$. Both values lie in the expected range, validating this setups ability to measure refractive indexes.

This chapter has demonstrated the possible benefits of using generalised measurements as an alternative to Stokes measurements. They can be used to effectively characterise polarisation structures and Mueller matrices of known and unknown optical elements.

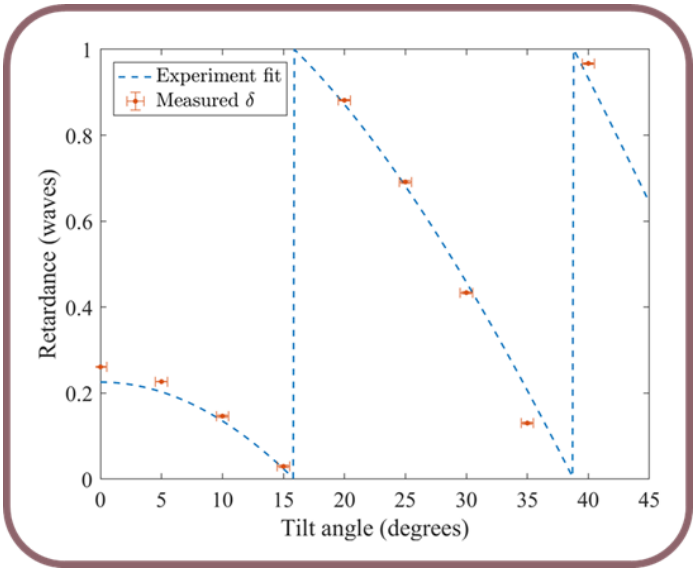

Figure 4.7: Retardance as a function of angle of incicence in a QWP with a fast axis at 0°. An average of the measured retardance is displayed in orange, and an experimental fit in blue. The fit can be used to calculate the wave plate's refractive indexes. Figure taken from [2].

The experiment's main benefit over other methods is that it can measure Mueller matrices and refractive indexes of changing optical media in real time, as shown in the supplemental material of [2] (there's a rotating wave plate video). The stability investigation revealed that it can be used to monitor an optical process over a longer time span without needing further input. As such it shows promising applications for characterising biological or chemical samples in a non invasive way - especially in situations that require a low level of probe light, or even single photon illumination. The interferometer is also suitable for miniaturisation into integrated optics.

conclusion of part I

Thus concludes the part of the thesis concerned with the behaviour of light. Everything said until this point is sufficient in order to understand its role in semiclassical atom-light interaction.

A direct consequence of Maxwell's equation are electromagnetic waves that propagate through space at the speed of light. They are transverse waves, which means they have polarisation, and they have an intensity profile in the transverse plane. If the intensity profile does not change in time or space, the beam is considered to be an eigenmode of propagation. Different modes that carry different polarisations can be combined to form a vector beam with a spatially dependent polarisation profile. The spatial dependence of the polarisation is quantified as the optical concurrence, a classical analogue to quantum entanglement. There are multiple ways of denoting polarisation, each suited to different applications.

Light is not transverse to the propagation axis, instead it is transverse to the wave vector. The wave vector of any beam points to the focus, causing most beams to have a longitudinal component. This component becomes significant when the beam is focused by a high numerical aperture lens. Prior to the work presented in chapter 9, it has never been directly measured.

The polarisation of light can be mapped to the surface of the Poincaré sphere. This state space was used to demonstrate that the minimum number of measurements for full tomography of polarisation is smaller than that used by conventional Stokes measurements. A change in basis states hence enables the single shot measurement of the polarisation of a vector beam, enabling us to measure real-time changes in the optical activity of samples. This lends itself to many exciting applications, biomedical sciences already use polarised light to investigate living tissues, and the system's efficiency makes it well suited to low-light experiments.

It probably says something that even the one pure optics experiment in my thesis was secretly about light-matter interaction. But while wave plates are classical elements, atoms are not. The structure of light, e.g. whether a beam is comprised of HG or LG modes, is a matter of chosen basis. Atoms, as fully quantised particles (or waves?) take this principle one step further.

It is time to dive into the matter of the thesis (pun intended).

CONCLUSION OF PART I

II

anatomy of an atom

This thesis is about atoms. The atom was initially conceptualised to be the fundamental building block of the universe, with its name translating to "unsplittable" (ironic, in hindsight).

The atom consists of a nucleus - which is made up of protons and neutrons, which in turn consist of quarks - and an outer electron shell. To many, the wave-like behaviour of a bound electron was the first introduction to the strange nature of quantum physics. The positive charge of the nucleus provides a potential well, in which the electrons are free to oscillate. These harmonics, or orbitals, are solutions to the **Schroedinger equation**, and their discrete energy levels and three dimensional harmonic wavefunctions are at the centre of entire academic disciplines, and the reason why objects as we know them are able to exist.

The particular field that provides the wider context of this thesis is **semiclassical atom optics**. The semiclassical limit assumes that a quantised atom is interacting with a classical light field (as described in part I) rather than individual photons. While this does not account for all effects that can be observed with its corresponding experiments [103], it provides a detailed enough approach that it can describe all phenomena that will be seen in the lab in part III. This part and the next are intended to complement each other, approaching the same phenomena from both theory and experiment.

Because of this, the atom I mean when I say atom optics is **Rubidium 87** (Rb-87). While everything said here is intended to be general, or at least transferable, it will be consistently used as an example in the two following chapters. It even gets its own section in chapter 7.1.

In the coming two chapters, a comprehensive model of the atom will be constructed. Beginning with the quantum numbers, it will become noticeable that the atom can carry various types of angular momentum. As this angular momentum is carried by charged particles, there are multiple sources of magnetic fields at play. This becomes relevant for atom-light interaction, and even more relevant in the presence of an external magnetic field - which is even capable of altering the quantum numbers.

All this once again comes down to a choice of basis states. It will be seen that the effects induced by an electric or magnetic field present differently when projected onto different quantisation axes, and that this can be used to construct an atomic state interferometer.

But to get there, one must assemble a toolkit for understanding the quantum world (semiclassically).

5 atomic theory

Our current model of the atom consists of a number of electrons in spherical harmonics around the nucleus. Solutions of the Schroedinger equation provide full information about the atomic processes, however from an analytical standpoint, the Schroedinger equation remains unsolved for all elements larger than helium. In order to be understood, the atom has to behave closely enough to hydrogen or helium that it can be approximated as a heavy version thereof.

The first column in the periodic table contains the alkali atoms. In their neutral state, alkali atoms only have a single electron in their outermost shell. As full electron shells destructively interfere with themselves and therefore cancel out, alkali atoms act as though they only have one single electron. From an optical perspective, this makes them analogues of hydrogen, but with a bigger nucleus [103].

It is possible to use Hydrogen for spectroscopic measurements, but doing so is unusual. Hydrogen is so light (in weight) that the radiation pressure from interacting with a photon entirely changes its trajectory. It is therefore common to do research on atom light interaction using heavier alkali atoms, and model their electron shells as those of Hydrogen. Most alkali species see some use [104]. Sodium saw much popularity in early atom optics, it was used to first demonstrate optical pumping [105] and in the discovery of dark resonances [106]. The main advantage of studying lithium is the attractive potential caused by atom-atom interactions [107], as well as its natural occurrence as both a bosonic and fermionic isotope [108]. Potassium, too, has fermionic isotopes [109], and is just gaining in popularity. Due to its high instability, francium sees little use. It is mostly used for research relating to atomic parity non-conservation [110]. Caesium is most well known for its use in atomic clocks, which led to the redefinition of the second [111]. Rubidium is arguably the most popular element in atom optics, to the point where it is often seen as the default. Chapter 7.1 is entirely dedicated to its features (as is the rest of this thesis, let's be honest). It is used in Bose-Einstein Condensation (BEC) [112, 113], atomic clocks [114], Rydberg atoms [115], magnetometry [116], trapping and manipulation [117], and of course interaction with vector light [1, 118]. Though not all atom optics is done on alkali elements - alkali metal ions also see use [119], and some experiments use mixtures of diffent atomic species [120].

This chapter aims to provide an overview of all concepts necessary to understand atom light interaction in the semiclassical limit, in which light is understood to be a classical wave, in order to highlight inner atomic processes in all their quantum glory. These concepts are applied to conceptualise an atomic state interferometer in chapter 6 which is then realised in chapter 8. Additionally, it is revealed in chapter 9 that everything discussed in this chapter is linked to the possibility of the interaction with non-paraxial light.

5.1 quantum numbers

IN WHICH THE COMPOSITION OF AN ATOM AND ITS INTERACTION WITH ITSELF IS DISCUSSED

There are four quantum numbers characterising the wave function of an electron within an atom. They are n, l, m_l and m_s. The **principal quantum number** n is the order of the outermost shell, and, for a neutral atom in its ground state, the row of the element in the periodic table. The **azimuthal quantum number** l indicates the subshell, which corresponds to the amount of OAM present in the electron. l ranges from 0 to $n-1$. This number is perhaps more well known from a different context: an electron with $l=0$ is an S orbital, $l=1$ a P orbital, $l=2$ a D orbital, etc. The specific orbital within the subshell, however, is given by the **magnetic quantum number** m_l. It can occupy integer values from $-l$ to $+l$. It corresponds to the projection of l along the chosen quantisation axis. The last one is the **electron spin** s. As fermions, electrons have spin of $\frac{1}{2}\hbar$, and their projection onto the quantisation axis m_s can take two values: $+\frac{1}{2}$ or $-\frac{1}{2}$. Pauli's exclusion principle says that two electrons can occupy the same orbital if they have opposite spin. Spin in general is very difficult to conceptualise [103, 121].

In its neutral ground state, Rb-87 has one electron in its 5th and outermost shell. This means it has the following quantum numbers: $n=5$, $l=0$, and hence $m_l=0$ and $m_s=-\frac{1}{2}$. This makes it an s-block element, with its valence electron having a ground state in the s subshell.

The nucleus however has spin too, it is the sum of the spin of all nucleons. This makes it isotope specific. Rb-87 has a **nuclear spin** $I=3/2$. The nuclear spin, too, can be projected onto the quantisation axis, this projection m_l ranging from $-I$ to I in integer steps.

Now, three of these quantum numbers are angular momentum related, and three more are the magnetic projections thereof. In an experimental setting, it is often more useful to have the information about their composite effects rather than to consider them individually, as they will certainly interfere with each other.

5.1.1 composite quantum numbers

A charged particle with angular momentum generates a magnetic field. Two magnetic fields will interfere, altering the particles generating it. The magnetic quantum numbers introduced earlier in this chapter will therefore have an impact on each other, in other words their angular momenta can couple to each other.

In atomic physics, a regime is characterised by its "**good quantum numbers**". A quantum number is considered good if it remains constant. Depending on the environment, atomic states characterised by some quantum numbers may couple to other states, so they can no longer be treated as constants. Generally, good quantum numbers are eigenvalues of operators that commute with the Hamiltonian.

Spin orbit coupling refers to the interaction between the electron's OAM and spin. It is the strongest of the couplings between angular momentum operators (resulting in coupled quantum numbers), spanning multiple experimental regimes. It is expressed as the **total electron angular momentum** j, which is calculated as the vector sum of the spin and the azimuthal quantum number [122]:

$$j = l + s \tag{5.1}$$

When projected onto the quantisation axis, its allowed values range from $-j \leq m_j \leq j$. This magnetic quantum number produces shifts in the atom's energy level, as will be explained in chapter 5.2.3. Notation for specific state configurations with spin orbit coupling is done in the following way: $n\ \ell_{|m_j|}\,|m_J, m_I\rangle$. Here are some examples: $5S_{1/2}\,|1/2, 3/2\rangle$ or $5P_{3/2}\,|3/2, 3/2\rangle$.

Under some circumstances (the specifics are the subject of chapter 6) the nuclear spin couples to the angular momentum of the electron. This **total angular momentum** F is the vector sum of its components [123]:

$$F = j + I \tag{5.2}$$

Specific F states can be denoted like n orbital$_{|m_j|}$ "F"$= F$, e.g. $5S_{1/2}F = 1$. In its ground state, Rb-87 can have two F sublevels: $(j = \pm 1/2) + (I = 3/2)$. Its $P_{3/2}$ state has four sub levels: $(j = (\ell = -1, 0, 1) + (s = \pm 1/2) = \{\pm 3/2, \pm 1/2\}) + (I = 3/2) = (F' = \{0, 1, 2, 3\})$

The projection of the total angular momentum m_F onto the quantisation axis, too, produces energy shifts that are the subject of chapter 5.2.5, and form the basis of all theoretical work done in chapter 6.3.2. But to get there, some groundwork must be lain concerning the very nature of atom-light interaction.

5.2 atom-light interaction

AN INTRODUCTION TO THE PROCESSES OF ATOM LIGHT INTERACTION, HEAVILY DRAWS ON THE WORK BY C.J. FOOT IN [103]. THIS SECTION COVERS BOTH FINE AND HYPERFINE STRUCTURE.

Every atomic state is associated with a specific energy. Two atomic states of different energies are separated by an energy gap. Energy can travel through the electromagnetic field, and if it carries the precise amount of energy needed to bridge the gap, the atom can absorb the photon and jump to the higher state. If the wavelength is much larger than the atomic radius a_0, the **dipole approximation** can be made, which pictures the atom interacting with a homogeneous electric field which oscillates at the atomic resonance frequency ω, inducing an oscillating electric dipole moment within the atom [103]. This is the only type of transition considered in this thesis.

5.2.1 Rabi oscilations

Consider, for now, a two level atom. In the presence of a driving electric field, it will oscillate between the ground state and the excited state. These Rabi oscillations were first described by I. Rabi in 1945, and their angular frequency is called the **Rabi frequency**, or Ω_R. If at time $t = 0$ the atom is in the ground state, it will be in the excited state at $\Omega_R\ t = \pi$, and return to the ground state at $\Omega_R t = 2\pi$. At all

other points in this period, the atom is in a superposition state. The populations are described by a set of equations:

$$|c_1(t)|^2 = \frac{\Omega_R^2}{\Omega_R'^2}\cos\left(\frac{\Omega_R' t}{2}\right) \tag{5.3}$$

$$|c_2(t)|^2 = \frac{\Omega_R^2}{\Omega_R'^2}\sin\left(\frac{\Omega_R' t}{2}\right), \tag{5.4}$$

where $\Omega_R' = \sqrt{\Omega_R^2 + \Delta^2}$, and Δ is the detuning. In other words, the effective Rabi frequency is detuning dependent - the further the light moves off resonance, the weaker the oscillations.

Rabi oscillations are a coherent process. This means its superposition structure is collapsed by quantum measurement. It can also randomly collapse due to spontaneous emission or other decoherent processes.

5.2.2 dispersion and absorption

The electric field changes the atom, and the atom changes it back. On resonance, the atoms absorb the energy of the electric field, but off resonance they still interact with its phase. Both of these effects stem from the atom's refractive index n_c.

The refractive index was introduced earlier in chapter 1.2.1 in a simplified form. In reality, it is a complex number. Its real part describes the dispersive effects that have been seen all throughout part I of this thesis, and its imaginary part is equal to the absorption coefficient [103]. These components are related via the Kramers-Kronig relations [124]:

$$\chi'(\omega) = \frac{2}{\pi}\int_0^\infty \omega' d\omega' \frac{\chi''(\omega')}{(\omega'^2 - \omega^2)} \tag{5.5}$$

where χ'' is the refractive index and ω is the angular frequency. For atoms, these effects are wavelength dependent. Figure 5.1 shows that approaching resonance, dispersive effects grow before being overtaken by the absorption line. The sign of the dispersive effects depends on whether the light is red or blue detuned.

In chapter 5.2.4 it will be revealed that atomic transitions are polarisation dependent. Thus the refractive index does not only depend on wavelength but also polarisation. The full effects of this are discussed in chapter 6.1.1.

For reasons beyond the scope of this thesis, every transition has depths and widths, but all follow the Lorentzian shape and its derivative from figure 5.1. However, in chapter 6.3.2, the spatially dependent refractive index of the $5S_{1/2}F = 1 \rightarrow 5P_{3/2}F' = 0$ transition of Rb-87 will be derived via the Master equation. But first, some elaboration on atomic level structure.

5.2.3 fine splitting

Fine splitting refers to the energy shifts induced by spin orbit coupling. Energy levels that would at first glance be considered to be degenerate (sharing the same energy) now have different energies, and transitions between them require the absorption of a photon [125].

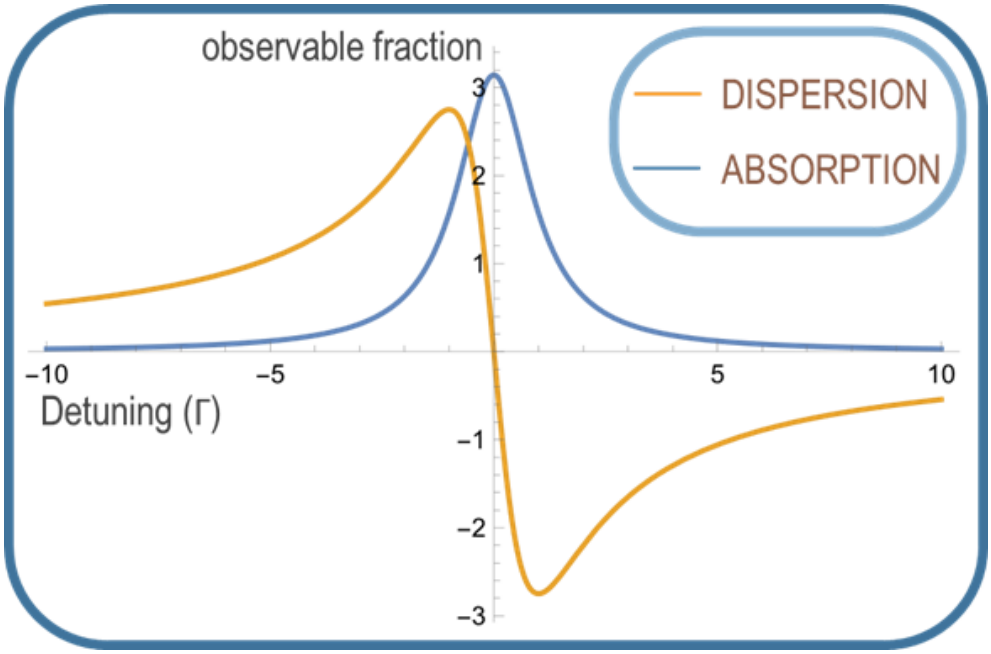

Figure 5.1: Simulated dispersion and absorption in terms of the natural linewidth Γ near the resonant frequency of a generic two level atom. The absorption line has a Lorentzian shape. It is related to the dispersion via Kramers-Kronig relations.

There is an additional effect that can occur on the same order of magnitude as fine splitting: The Lamb shift induces additional changes in the effective energies of the atomic sublevels. It is caused by vacuum effects that require an understanding of quantum electrodynamics to explain, and will hence go undiscussed [103].

Figure 5.2 shows the fine splitting between the S,P and D levels levels for Rb-87. j is a good quantum number here, as P is split by $|m_j|$ rather than $|m_l|$. The transitions between states have names: $5S^2_{1/2} \rightarrow 5P^2_{1/2}$ is called the **D1 line**, and $5S^2_{1/2} \rightarrow 5P^2_{3/2}$ the **D2 line** [121]. From this point onwards, this thesis only concerns itself with the D2 line.

5.2.4 selection rules

Angular momentum is a conserved quantity. The transition from one atomic level to another cannot change the amount of angular momentum in the universe. Transitions between energy levels with different amounts of angular momentum have to get the difference in angular momentum from somewhere. In chapter 1.1.1, it was shown that circularly polarised light carries $\pm\hbar$ of angular momentum, or ± 1 in natural units. If a circularly polarised photon is absorbed, its angular momentum is transferred to the atom.

As such, the angular momentum of an atom can be altered during atom-light interactions, but only in units of 1. For a generic projection of angular momentum m:

$$\Delta m = 0, \pm 1. \tag{5.6}$$

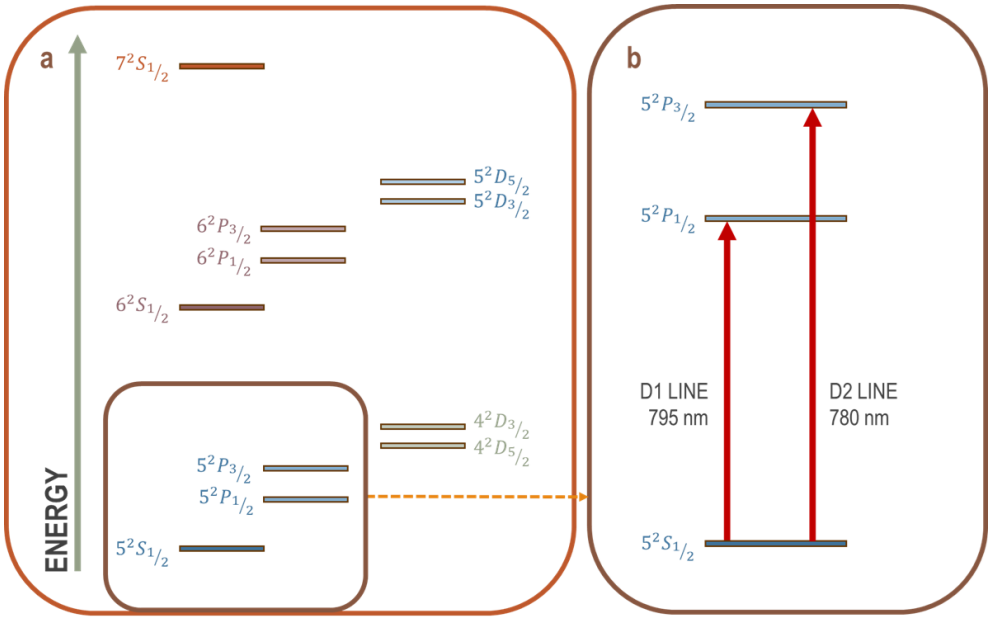

Figure 5.2: Fine structure of Rb-87. Energy not to scale. Spin orbit coupling causes sublevels of the same n state to separate in energy. a) shows the simplified level scheme from $5^2S_{1/2}$ to $7^2S_{1/2}$. b) zooms in on the $5^2S \rightarrow 5^2P$ transitions enabled by fine splitting. The $5^2S_{1/2} \rightarrow 5^2P_{1/2}$ transition is often called the D1 line and can be driven by light with a wavelength of 795 nm. The $5^2S_{1/2} \rightarrow 5^2P_{3/2}$ transition is called the D2 line and driven by light with a wavelength of 780 nm. The work in this thesis is done on the D2 line.

Transitions can change the angular momentum of the atom. Due to the conservation of angular momentum, the projection of the atom's angular momentum onto the propagation axis may also be changed, these transitions are called $\hat{\sigma}_+$ and $\hat{\sigma}_-$ transitions, depending on the sign of the change. The transition with no projected angular momentum transfer is called the $\hat{\pi}$ transition. Any transitions that fall outside this range are often referred to as "forbidden transitions". This rule applies for l,m_l,j,m_j,F, and m_F, but the spins are of course further restricted to their previously discussed values. Transitions always have to satisfy the selection rules for the good quantum number in the relative regime [126].

For completeness, it should be remembered that in chapter 2.1.3 it was said that light can not only carry spin but also orbital angular momentum. This has been used to drive transitions with $|\Delta L| > 1$, but such transitions are no longer described by the dipole approximation [127].

5.2.5 hyperfine splitting

In the regime in which F is a good quantum number (see chapter 6.3 for more information), the fine structure states are further split hyperfine sublevels.

Figure 5.3 shows this hyperfine structure for the D2 line of Rb-87. Note how the number of hyperfine sublevels grows with the orbital angular momentum of the fine structure state. As an S-block element, its ground state has $l = 0$, and so due to $F = I + s$ has two F sublevels, whereas the excited state has four sublevels.

There is an even finer structure: splitting can occur between the m_F sublevels. This will become relevant later in chapter 6.3, where a Hamiltonian of the $5S_{1/2}F = 1 \rightarrow 5P_{3/2}F' = 0$ transition and all its sublevels is constructed. But to get to this point, the last determining factor has to be discussed, for the determining factor of all angular momentum coupling is the ambient magnetic field.

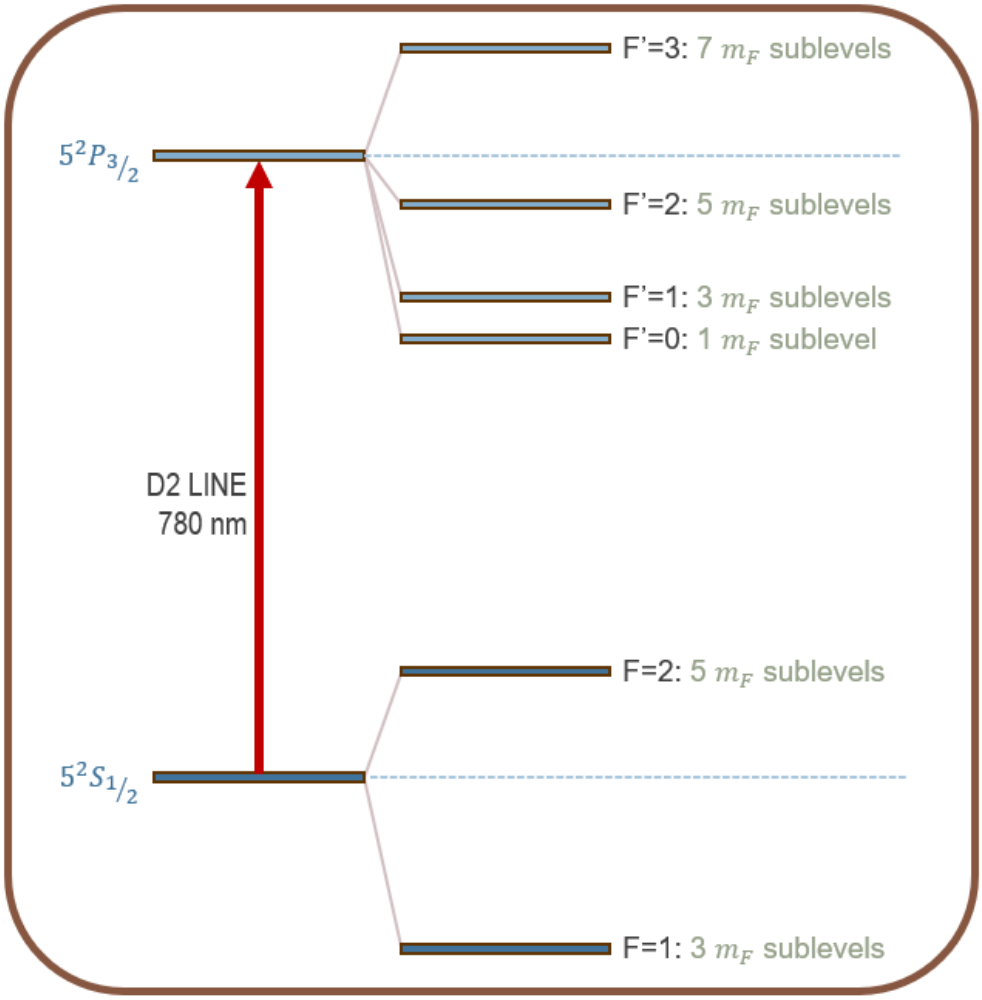

Figure 5.3: Diagram of hyperfine sublevels of the D2 line. Energy gaps between ground and exctited states not to scale. The system has two ground states and four excited states. Figure based on data presented in [121].

6 a break in the symmetry: magnetic fields

As mentioned in chapter 5.1.1, angular momentum states can couple to one another, as the rotating charges generate magnetic fields that interfere with each other. This results in a change of good quantum numbers. It should come at no surprise then, that magnetic fields generated by other sources also impact the atom. This can lead to a multitude of related effects, depending on the strength of the magnetic field, and its angle to the propagation axis.

As will be seen in chapter 6.2, a magnetic field of sufficient strength can couple to the angular momenta individually, leading them to decouple from one another. Weak magnetic fields leave the F quantum number intact, but that is not the same as leaving it unchanged. In chapter 1.2 the lab frame was used to provide a coordinate system, as light has no natural bases in the transverse plane. This notion was fully explored in chapter 1.5.1, where it was shown that any basis of states is equally valid, and in chapter 5 the atoms were largely treated as rotationally symmetric.

This is no longer true in the presence of a magnetic field. The propagation axis and the magnetic field direction both make their spatial direction distinguishable from the others, introducing an anisotropy, and the geometry of the system hinges on whether they are orthogonal or not. Chapter 6.3.2 will show that which atomic states can exist entirely depends on the choice of quantisation axis. To get there, we need to pay attention to the often overlooked m_F sublevels.

6.1 Zeeman splitting and Larmor oscillations

WHICH PROVIDES AN OVERVIEW OF THE MAGNETIC EFFECTS ON THE ATOMIC LEVEL STRUCTURE AS DESCRIBED BY THE ZEEMAN HAMILTONIAN, AND HOW THEY ARE CAPABLE OF ALTERING POLARISATION.

A charge with angular momentum is equivalent to a current loop. A current loop in a magnetic field is susceptible to induction. This holds true down to even individual spins, but if the states are coupled, this effect presents itself in the modification of "good" quantum numbers. The induction changes the energy of the sublevel in question in proportion to its angular momentum, causing degenerate sublevels to further split. This effect was first observed by P. Zeeman in 1896, and is named **Zeeman splitting** in his honour. It can be described by the Zeeman Hamiltonian $\hat{H}_Z$, which takes the following form [122]:

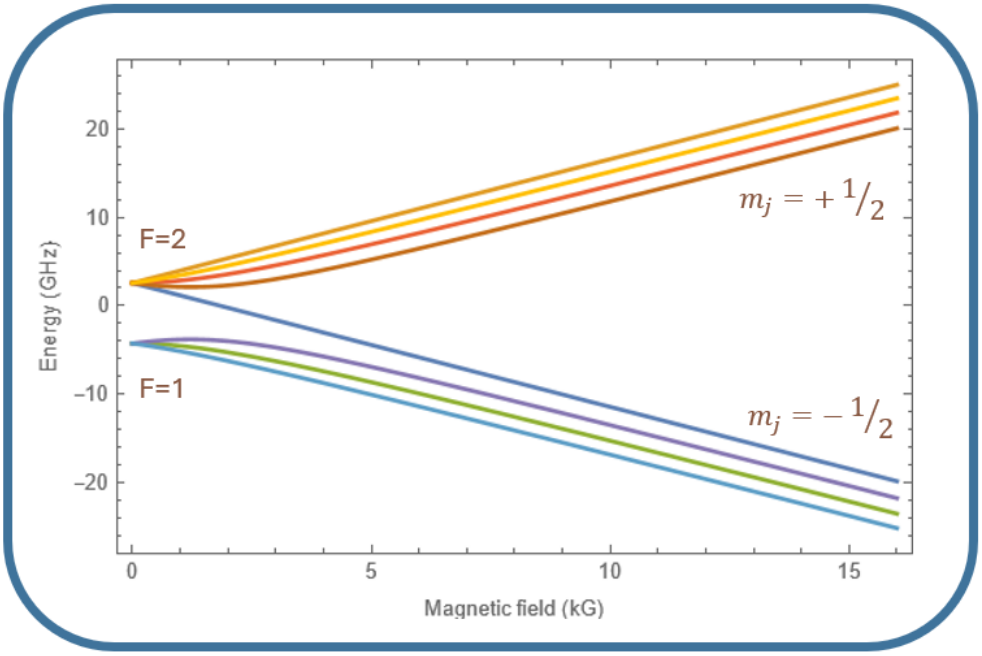

Figure 6.1: Breit-Rabi diagram showing the Zeeman splitting of the $5^2S_{1/2}$ sublevels of Rb-87. E=0 corresponds to the unshifted $5^2S_{1/2}$ state. Note that for low magnetic field the energies are grouped (i.e. closer together) by F state, whereas for bigger magnetic fields they regroup by m_j. This corresponds to a shift in good quantum numbers.

$$\hat{H}_Z = -\frac{\mu_B}{\hbar}(g_l\vec{l} + g_s\vec{s} + \frac{m_e}{m_p}g_I\vec{I}) \cdot \vec{B}, \tag{6.1}$$

where m_e is the mass of the electron and m_p is the mass of the proton. The Landé g-factors g_l, g_s and g_I characterise the magnetic moments of their respective angular momenta. Note the presence of all angular momentum quantum numbers from chapter 5.1, and that they are all represented individually rather than in their composite forms. The effects of this are shown in figure 6.1 for the sublevels of the $5S_{1/2}$ and $5P_{3/2}$ states of Rb-87. As the magnetic field increases, a regrouping occurs: For a zero magnetic field, all m_F sublevels are degenerate, but as magnetic fields increase they begin to split. Once this process becomes nonlinear, F stops being a good quantum number, but with a further increase, the behaviour begins to linearise again in different groups - the m_j sublevels. The strength of the external magnetic field dictates which quantum numbers are good.

These regimes have names to easily distinguish them for experimental and theoretical use. The realm of weak magnetic fields is called the Zeeman regime. It provides the backdrop to the theoretical work done in chapter 6.3 which is experimentally realised in chapter 8. Strong magnetic fields shift the atom into the Paschen-Back regime, ruled by the quantum numbers j and m_j. It is elaborated upon in chapter 6.2, and used for all experiments described in chapter 9.

Depending on the reference frame, this effect can present in an additional way: The atom is an object that is fundamentally quantum in nature. The superpositions of its states are as valid as their pure forms, and how they project onto any given quantisation axis depends on said quantisation axis. In the realm of atom light interaction, all magnetic fields can be considered to have a longitudinal component that is aligned with the magnetic field, and a transverse component that is orthogonal to it. As the effects of the magnetic field present differently depending on the magnetic field angle, these components are usually considered one at a time. A system in which the propagation axis is aligned with the magnetic field is called the **Faraday configuration**, and a magnetic field that is fully orthogonal to the propagation axis is in the **Voigt configuration**.

In the Faraday configuration, the absorptions affect the circular components exactly as discussed above, but in the Voigt configuration, there are now two choices of quantisation axis. Picking the propagation axis effectively misaligns the magnetic moments of the magnetic sublevels from the magnetic field. These magnetic dipoles are now acted upon by the Lorentz force, leading them to rotate around the axis of the magnetic field in a process known as **Larmor precessions**. The angular frequency of this is called the Larmor frequency, or Ω_L, and is given by [103]:

$$\Omega_L = \frac{eB}{2m_e}. \tag{6.2}$$

Of course, this is the same effect that causes Zeeman splitting [128], but it presents differently: when projected onto the propagation axis, the atom appears to periodically hop between degenerate(ish) states. In the Hamiltonian, this presents as off-diagonal terms connecting the sublevels.

Whether the atom is in the Faraday or Voigt configuration affects absorption and dispersion: In chapter 5.2.4, it was shown that from any given state, there is a maximum of three possible dipole-allowed transitions: $\pm 1\hbar$ of angular momentum, or no angular momentum transfer. The orientation of the angular momentum states couples to the magnetic field, so the three possible polarisations are co-rotating, counter-rotating, and aligned with the magnetic field axis. If the magnetic field is transverse to the propagation axis, the latter is the only paraxial polarisation, and therefore the only transition that can be driven - no angular momentum transfer is possible. In other words, in the Voigt configuration, the light can only be absorbed by the atom if it is polarised along the magnetic field direction.

In the Faraday configuration, the opposite is the case. The transverse plane is isotropic if the magnetic field is aligned with the propagation axis, and so to interact with the atom, the polarisation needs to be rotationally symmetric - in other words, the transitions are driven by right and left circularly polarised light. Circularly polarised light drives the $\hat{\sigma}_\pm$ transitions, which is by definition between states with different angular momenta. These states are unequally affected by the Zeeman splitting, which means that the energy gap is shifted. The angular momentum transitions $\hat{\sigma}_-$ driven by $|R\rangle$ are always red detuned with respect to the $\hat{\pi}$ transition, and $\hat{\sigma}_+$ transitions driven by $|L\rangle$ are always blue detuned by the same amount.

As explained in chapter 1.5.1, any polarisation can be expressed in terms of $|R\rangle$ and $|L\rangle$, so the third orthogonal component required to drive the $\hat{\pi}$ transition would have to be aligned with the propagation axis. This is done for the first time in chapter

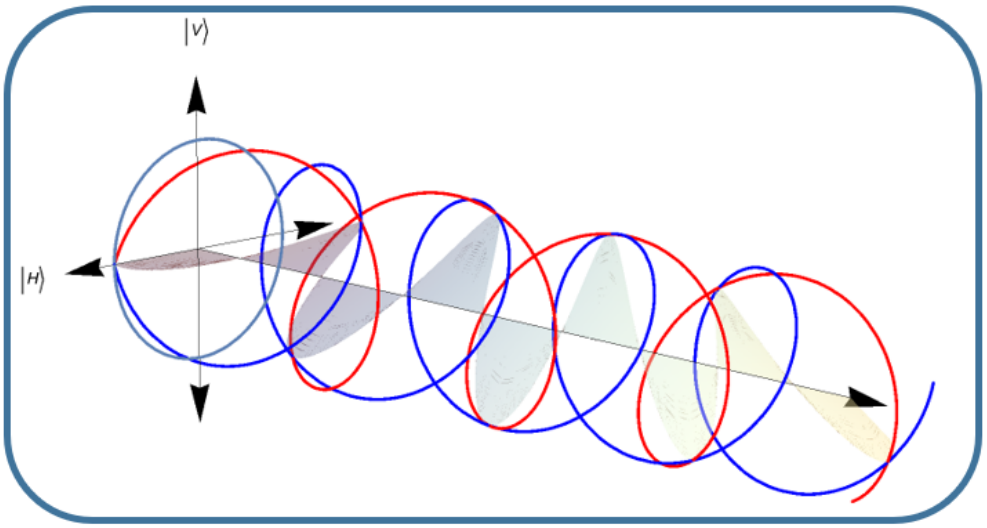

Figure 6.2: Theoretical diagram showing the faraday effect. Red is right circular and blue is left. The retarding effects are 1.5 as much on right as they are on left. Linearly polarised light is rotated upon propagation, changing its orientation.

9. However, the Faraday configuration has one final secret to reveal.

6.1.1 the Faraday effect

In chapter 5.2.2, it was shown that the absorption is the imaginary part of the complex refractive index. Its real part changes the phase retardance of the resonant polarisation, rendering the atom birefringent.

In the Faraday configuration, the eigenmodes of absorption are $|R\rangle$ and $|L\rangle$ (and $|z\rangle$). The absorption lines of these two polarisations are now frequency separated. Close to resonance of each of these lines are regions where the atom is circularly birefringent, as the dispersion curves (see figure 5.1) shift with the absorption lines. This turns the atomic cloud into an optical rotator, like in chapter 1.2.1. Figure 6.2 shows that a circularly birefringent medium will effectively rotate a propagating linearly polarised beam by changing the phase between its circular components. The resulting change in orientation of the polarisation ellipse is called **Faraday rotation** [129]. Experimentally, this effect is seen in chapter 9.4.1.

Right circularly polarised light propagating in the $+z$ direction and left circularly polarised light propagating in the $-z$ direction have identical electric fields. This concept, known as the photon's chirality, was originally introduced in chapter 1.1.1, and becomes relevant in the picture of light co or counter propagating with the magnetic field. In other words, reversing the magnetic field is equivalent to reversing the Zeeman splitting and therefore the direction of Faraday rotation [130].

It is also possible to create a magnetic field from polarised light via the inverse Faraday effect [131], and it can emerge from paramagnetism [132].

The Faraday effect sees many practical applications. It is most famous for being the key component in the most common type of optical isolator [133, 134], but in addition it can be used for narrow band optical filtering [135], optical switching [136,

137], constructing dichroic beamsplitters [138], magnetometry [139], and even far off-resonance laser locking [140](see chapter 7.3.1 for an explanation of laser locking).

As the Zeeman splitting depends on the strength of the magnetic field, so does the characteristic rotation. The way the energy levels are organised is determined by the good quantum numbers. Not every value of magnetic field has good quantum numbers, but a few distinct regimes with specific sets of rules have emerged. Here are two of them.

6.2 the hyperfine Paschen-Back regime, or strong magnetic fields

WHICH PROVIDES AN OVERVIEW OF HOW ATOMS ARE AFFECTED BY MAGNETIC FIELDS THAT ARE STRONG ENOUGH TO DECOUPLE THEIR NUCLEAR SPIN FROM THE ELECTRON.

Increasing the magnitude of the external magnetic field increases its coupling to the angular momentum quantum numbers. The Zeeman regime is left behind when F stops being a good quantum number, but once the field is significantly stronger than the coupling between nuclear and electron angular momentum, the atom enters the **Paschen-Back regime**. Under these conditions, the Zeeman shift is linearly dependent on the magnetic field [122]:

$$\Delta E \approx (g_j m_j \mu_B + g_I m_I \mu_N) B, \tag{6.3}$$

where μ_B is the Bohr magneton, μ_N the nuclear magneton, g_j is the Landé g factor for j and g_I that for I. The energy shift only depends on the magnitude of the magnetic field B, not its direction. m_j and m_I are good quantum numbers in this regime [122, 141].

The hyperfine Paschen-Back regime is characterised by the Zeeman shift always exceeding the ground state hyperfine splitting (see chapter 5.2.5). For Rb-87 this effect starts at 0.24 T [142], but full resolution of all transitions is only achieved at higher values, such as 1.6T, which is used for figure 6.3.

This diagram is called a Breit-Rabi diagram. Shown on the left are the sublevels from figure 6.1. The Zeeman splitting in the excited state is much weaker than that of the ground state, so while both m_I and m_j are used to specify the ground state, only m_j is used to distinguish between excited states. The detuning between individual transitions now lies in the GHz, and so the angular momentum transitions are separated into different batches in frequency space. However, the states aren't entirely pure, though the strength of the mixtures decreases as the magnetic field is increased. These mixtures can cause some weak crossover transitions [141].

Due to the strong frequency separation of the angular momentum transitions, the absorption spectra look vastly different depending on the magnetic field angle. The top half of figure 6.3 shows the spectrum in the Voigt configuration with a transverse and polarisation aligned magnetic field on top, and a londitudinal magnetic field, i.e. the Faraday configuration below it. This is the natural conclusion of chapter 6.1, in which it was said that $\hat{\pi}$ transitions are exclusive to the Voigt configuration, as

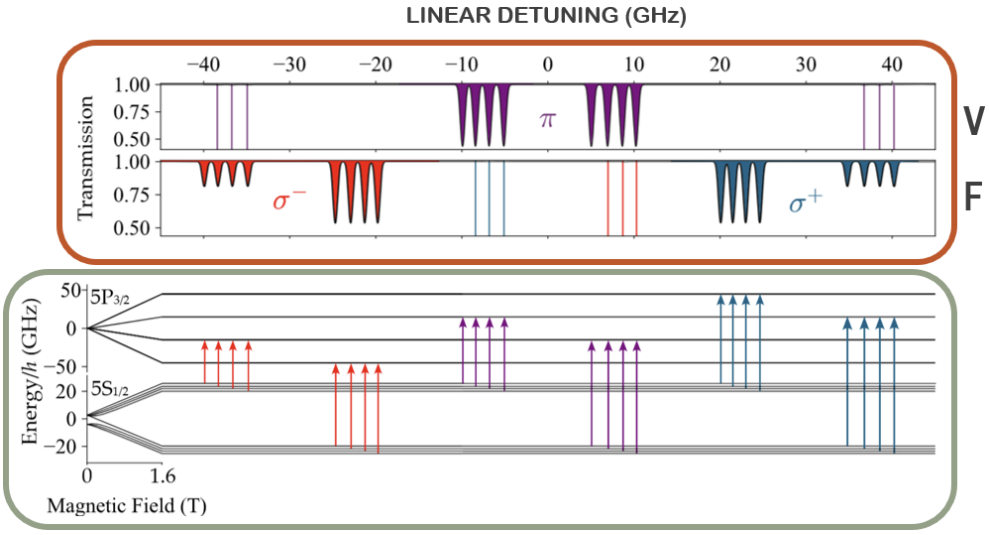

Figure 6.3: Absorption spectra in the hyperfine Paschen-Back regime for a paraxial linearly polarised beam. The box at the bottom shows the level scheme at 1.6T, where the flavours of transition are seperated in frequency space. The resulting spectra are shown in the box at the top: all transitions are Doppler resolved and grouped into packs of four. Some mixing of states remains, indicated by the lines in the top box, but it is very weak. V and F indicate the Faraday and Voigt configuration. σ_- transitions are colour coded red, σ_+ transitions blue, and π transitions purple. In the Faraday configuration, only $\sigma_\pm$ transitions are available, and in the Voigt configuration only π transitions. Figure adapted from [3], for which it was created by Danielle Pizzey.

are $\hat{\sigma}_{\pm}$ transitions to the Faraday configuration due to the paraxial nature of the light. Though, as mentioned in chapter 3, light is never fully transverse. The implications of this are brought to the lab in chapter 9.

Increasing the magnetic field even further will eventually once again lead to nonlinear effects - even the spin-orbit coupling can be split. Of more interest in this thesis, however, are the effects of magnetic fields that are weak enough to be easily controlled in three dimensions. If the available transitions are a function of the isotropy of its reference frame, what does this say about the atomic state space?

6.3 weak magnetic fields

THIS SECTION OUTLINES AN OVERVIEW OF THE THEORETICAL TOOLS USED IN THE CONSTRUCTION OF A HAMILTONIAN FUNCTION, USING MY OWN WORK MODELLING THE $F = 1 \rightarrow F' = 0$ TRANSITION OF RB-87. THIS WORK WAS DONE IN COLLABORATION WITH KUNTAL SAMANTA, NICLAS WESTERBERG, AND SONJA FRANKE-ARNOLD, AND CULMINATES IN THE DEVELOPMENT OF A GENERALISED DRESSED STATE PICTURE.

The Zeeman regime spans the range of external magnetic fields that aren't strong enough to decouple the nuclear spin I from the electron angular momentum j, and so the total angular momentum F and its projection m_F are the good quantum numbers. Under these conditions, the Zeeman shift is also linear, and can be described by the following equation:

$$\Delta E = \mu_B g_F m_F B_z, \tag{6.4}$$

where g_F is the Landé g-factor for F, and μ_B is the Bohr magneton [121]. In this regime, the energy shift depends only on the longitudinal component of the magnetic field. The selection rules are also simplified in the Zeeman regime:

$$-1 \leq \Delta F \leq +1 \tag{6.5}$$
$$-1 \leq \Delta m_F \leq +1. \tag{6.6}$$

The D2 line of Rb-87 was first introduced in chapter 5.2.3, and in chapter 5.2.5 it was shown that it has two F ground states and four F excited states. As the number of m_F sublevels scales with F, the simplest configuration among them is the $5s_{1/2}F = 1 \rightarrow 5p_{3/2}F' = 0$ transition.

The $5s_{1/2}F = 1$ ground state of Rb-87 has three m_F sublevels ($|g_-\rangle$, $|g_0\rangle$, and $|g_+\rangle$). The $5p_{3/2}F = 0$ has only one, $|e\rangle$. The possible transitions between the individual states form a lambda configuration, shown in figure 6.4. The magnetic field induces Zeeman splitting, changing the relative energy between the m_F sublevels, as well as Larmor precessions, coupling their populations.

It is this transition that concerns the majority of my theoretical work, for it can be reconfigured into a theoretical, and later, in chapter 8, experimental atomic state interferometer. To do this, everything discussed so far has to be brought together to form a Hamiltonian.

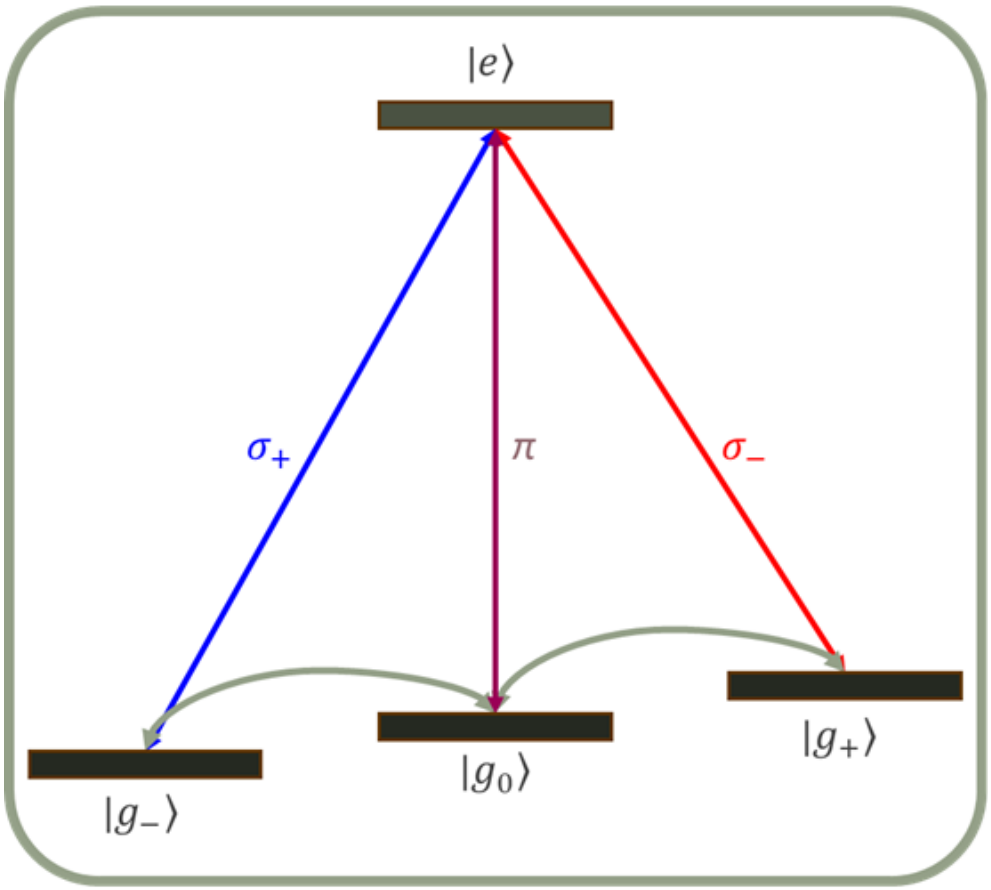

Figure 6.4: The $F = 1 \rightarrow F' = 0$ transition of the D2 line of Rb-87 forms a lambda transition, named for its shape.

6.3.1 constructing a Hamiltonian

The Hamiltonian $\hat{H}$ is an energy operator, that is to mean applying it to a state is the theoretical equivalent of measuring the system's energy. It can take the form of an $N \times N$ matrix acting on the N-dimensional vector containing the N possible states. Consider a two level atom:

$$\hat{H}_{2LV} = \begin{pmatrix} E_1 & \mathcal{J}_{21} \\ \mathcal{J}_{12} & E_2 \end{pmatrix} = E_1 |1\rangle \langle 1| + E_2 |2\rangle \langle 2| + \mathcal{J}_{21} |2\rangle \langle 1| + \text{H.c.} \tag{6.7}$$

The diagonal terms E_1 and E_2 are the energies of the states. If part of the aim is to explore energy shifts (like in this thesis), the unshifted energy of the state in question is set to 0. The off-diagonal terms $\mathcal{J}_{21}$ and $\mathcal{J}_{12}$ are complex conjugates of one another, and describe coherent hopping rates between the states. When considering atom light interactions, this is where Rabi oscillations and Larmor precessions are found. Of course, for larger systems there are specific hopping terms between any two states. This can get very complicated very fast. As will be seen in chapter 6.3.2, a large part of modelling atomic systems is reducing or simplifying these terms as much as possible.

As the energy operator, the Hamiltonian can describe a range of processes. A Hamiltonian that describes multiple separate processes can be expressed as the sum of the Hamiltonians of the individual processes. For example, the electric dipole interaction between an atom and a photon can be described by the dipole Hamiltonian

$$\hat{H} = -\vec{d} \cdot \vec{E} \tag{6.8}$$

where $\vec{d}$ is the induced electric dipole moment and $\vec{E}$ is the electric field. This is where the complex refractive index comes from. Similarly, the Zeeman Hamiltonian from equation 6.1 can describe magnetic effects between the energy levels of an atom.

The aim of this chapter is to construct a general Hamiltonian for the $5S_{1/2}F = 1 \rightarrow 5P_{3/2}F' = 0$ transition of the D2 line of Rb-87. It was shown earlier that this is a system with four states, which can be expressed using the state vector $|\Psi\rangle$:

$$|\Psi\rangle = \begin{pmatrix} g_+ \\ g_0 \\ g_- \\ e \end{pmatrix} \tag{6.9}$$

as this is the Zeeman regime, there is a strong magnetic coupling between all angular momentum quantum numbers. Therefore, the Zeeman Hamiltonian simplifies:

$$\hat{H}_Z = -\vec{\mu} \cdot \vec{B} \tag{6.10}$$

where $\vec{B}$ the magnetic field and $\vec{\mu}$ is the induced magnetic dipole momentm proportional to the Bohr magneton:

$$\vec{\mu} = -g_F \mu_B \left[\hat{z}\left(|g_+\rangle\langle g_+| - |g_-\rangle\langle g_-|\right) - \left(\hat{\sigma}_- |g_+\rangle\langle g_0| + \hat{\sigma}_+ |g_-\rangle\langle g_0| + \text{H.c.}\right)\right]. \tag{6.11}$$

The total Hamiltonian contains an additional term describing the energy of the excited state:

$$\hat{H}_{\text{lab}} = \hbar\omega_A |e\rangle\langle e| - \vec{d}\cdot\vec{E}(\vec{r}_A) - \vec{\mu}\cdot\vec{B}(\vec{r}_A) \tag{6.12}$$

where ω_A is the atomic resonance frequency. The states $|g_+\rangle$ and $|g_-\rangle$ have angular momentum, but $|g_0\rangle$ and$|e\rangle$ do not. This means that in order for the former two to hop into the excited state, they need to absorb light that carries angular momentum.

There are four states, this means the final Hamiltonian will have 16 elements. But what exactly those elements are depends on careful choice of parameters. The following subsections are intended to provide a toolkit for theoretical atom optics.

choice of electric and magnetic fields and quantisation axis

As the aim of this chapter is to create a general Hamiltonian, it has to be capable of modelling the interaction with any external magnetic field or (paraxial) radiation. The choice of notation for the latter is inherent to the available transitions. In chapter 1.3, the polarisation ellipse notation was introduced, which describes the polarisation in terms of angles on the Poincaré sphere, which do not favour any specific basis. As the atomic state vector separates the angular momentum states, it makes sense to initially separate the electric field the same way:

$$u_- = \cos\chi\, e^{-i\psi}, \tag{6.13}$$
$$u_+ = \sin\chi\, e^{i\psi}. \tag{6.14}$$

where $u_\pm$ are the circular polarisation components, and χ and ψ are the polar and azimuthal angles on the Poincaré sphere, respectively. This yields the spatially dependent electric field

$$\begin{aligned}\vec{E}(\vec{r}_\perp) &= E_0(\vec{r}_\perp)e^{i\omega t}\left[u_+(\vec{r}_\perp)\hat{\sigma}_+ + u_-(\vec{r}_\perp)\hat{\sigma}_-\right] + \text{c.c},\\ &= E_0(\vec{r}_\perp)e^{i\omega t}\Big[\sin\chi(\vec{r}_\perp)\, e^{i\psi(\vec{r}_\perp)}\hat{\sigma}_+ \\ &\qquad + \cos\chi(\vec{r}_\perp)\, e^{-i\psi(\vec{r}_\perp)}\hat{\sigma}_-\Big] + \text{c.c},\end{aligned} \tag{6.15}$$

which highlights the relevance to the atomic transition by using $\hat{\sigma}_+$ and $\hat{\sigma}_-$ rather than $|R\rangle$ and $|L\rangle$ to denote the polarisation components.

The light considered can be considered fully transverse, and as explained in chapter 6.1.1, this means the $\hat{\pi}$ transition is unavailable. The reason this initial state was chosen over its Voigt equivalent is that it interacts with both polarisaton bases,

whereas in the Voigt configuration only linearly polarised light aligned with the transverse magnetic field can interact. While this may seem like an oversight, chapter 6.3.2 will show that the transition itself is a function of the quantisation axis.

Using these basis states, the induced electric dipole of the atom takes the form:

$$\hat{\vec{d}} = \left[d\hat{\sigma}_+^* \left|g_+\right\rangle \left\langle e\right| + d\hat{\sigma}_-^* \left|g_-\right\rangle \left\langle e\right|\right]/2\sqrt{3} + \text{H.c.} \tag{6.16}$$

The electric dipole Hamiltonian from equation 6.8 can now be expanded to be:

$$\begin{aligned}\hat{H}_D &= -\vec{d}\cdot\vec{E} \\ &= -\frac{\Omega_R}{2\sqrt{3}}\left(\left[u_+e^{-i\omega t} + u_-^* e^{i\omega t}\right]\left|g_+\right\rangle\left\langle e\right| \right. \\ &\quad \left. + \left[u_-e^{-i\omega t} + u_+^* e^{i\omega t}\right]\left|g_-\right\rangle\left\langle e\right|\right) + \text{H.c.} \\ &= -\frac{\Omega_R}{2\sqrt{3}}\left(e^{i\psi}\left[\sin\chi\, e^{-i\omega t} + \cos\chi\, e^{i\omega t}\right]\left|g_+\right\rangle\left\langle e\right| \right. \\ &\quad \left. + \left[e^{-i\psi}\cos\chi\, e^{-i\omega t} + \sin\chi\, e^{i\omega t}\right]\left|g_-\right\rangle\left\langle e\right|\right) + \text{H.c.},\end{aligned} \tag{6.17}$$

Similarly, chapter 6.1 explained how the magnetic fields present is a matter of perspective, i.e. chosen parameterisation. To best seperate the Faraday and Voigt regimes, a spherical polar coordinate system is chosen:

$$\begin{aligned}\vec{B} &= B_0\left(\cos\theta_B\hat{z} + \sin\theta_B\cos\phi_B\hat{x} - \sin\theta_B\sin\phi_B\hat{y}\right) \\ &= B_0\left(\cos\theta_B\hat{z} + \frac{\sin\theta_B}{\sqrt{2}}\left[e^{-i\phi_B}\hat{\sigma}_- + e^{i\phi_B}\hat{\sigma}_+\right]\right),\end{aligned} \tag{6.18}$$

where θ_B is the polar magnetic field angle, ϕ_B the azimuthal one, and B_0 its magnitude. These polar coordinates are visualised in figure 6.5. The magnetic field is treated as fully homogeneous for the entirety of this thesis, but the model can be easily adapted to show the effects of spatially dependent magnetic fields, as long as they can be approximated to be homogeneous over the atomic radius. In a way, this is similar to the dipole approximation.

Using the magnetic field as the quantisation axis, the magnetic dipole moment from equation 6.11 can be put back into the Zeeman Hamiltonian from equation 6.10:

$$\begin{aligned}\hat{H}_Z &= -\vec{\mu}\cdot\vec{B} \\ &= \hbar\Omega_L\left[\cos\theta_B\left(\left|g_+\right\rangle\left\langle g_+\right| - \left|g_-\right\rangle\left\langle g_-\right|\right)\right. \\ &\qquad \left. -\frac{\sin\theta_B}{\sqrt{2}}\left(e^{i\phi_B}\left|g_+\right\rangle\left\langle g_0\right| + e^{-i\phi_B}\left|g_-\right\rangle\left\langle g_0\right|\right)\right],\end{aligned} \tag{6.19}$$

This version includes both Zeeman shifts due to longitudinal components, as well as Larmor precessions due to transverse components

Equation 6.12 unites all of these processes and provides a complete and general picture of the electromagnetic processes within the atom:

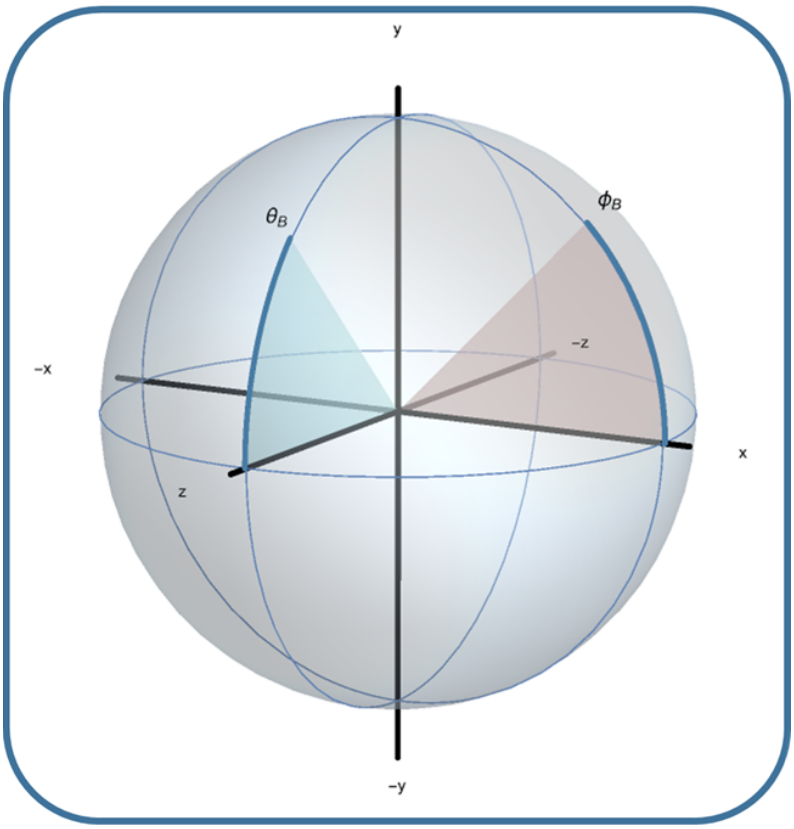

Figure 6.5: Convention of magnetic field polar coordinates θ_B and ϕ_B. Here, z is the propagation direction, so θ_B is the polar angle, and ϕ_B the azimuthal angle.

$$\begin{aligned}\hat{H}_{\text{lab}} &= \hbar\omega_A \left|e\right\rangle \left\langle e\right| - \vec{d}\cdot\vec{E}(\vec{r}_A) - \vec{\mu}\cdot\vec{B}(\vec{r}_A) \\ &= \hbar\omega_A \left|e\right\rangle \left\langle e\right| - E_0(\vec{r}_\perp)e^{i\omega t}\Big[\cos\chi(\vec{r}_\perp)\, e^{i\psi(\vec{r}_\perp)}\hat{\sigma}_+ \\ &\quad + \sin\chi(\vec{r}_\perp)\, e^{-i\psi(\vec{r}_\perp)}\hat{\sigma}_-\Big] + \text{c.c} \\ &\quad + \hbar\Omega_L\left[\cos\theta_B\left(\left|g_+\right\rangle\left\langle g_+\right| - \left|g_-\right\rangle\left\langle g_-\right|\right)\right. \\ &\quad \left. -\frac{\sin\theta_B}{\sqrt{2}}\left(e^{-i\phi_B}\left|g_+\right\rangle\left\langle g_0\right| + e^{i\phi_B}\left|g_-\right\rangle\left\langle g_0\right|\right)\right].\end{aligned} \tag{6.20}$$

This is four lines long. Simulating this will take and hour and might melt the computer in the process. Solving it analytically looks like a nightmare. Some simplification is direly needed.

Now, one problem that immediately stands out is that this equation is in the lab frame, which is not the ideal setting for evaluating a travelling wave. Maybe a coordinate change can fix our problems.

rotating wave approximation

Take a step back. Consider the two level system $\left|\Psi\right\rangle = c_g\left|g\right\rangle + c_e\left|e\right\rangle)$ performing Rabi oscillations driven by a plane wave. The time evolution of the complex amplitudes $c_{g,e}$ can be written as

$$i\hbar\frac{dc_g}{dt} = c_e\hbar\Omega^*\left(\frac{e^{i(\omega-\omega_0)t} + e^{-i(\omega+\omega_0)t}}{2}\right) \tag{6.21}$$

$$i\hbar\frac{dc_e}{dt} = c_g\hbar\Omega\left(\frac{e^{i(\omega+\omega_0)t} + e^{-i(\omega-\omega_0)t}}{2}\right). \tag{6.22}$$

For a system near resonance, $\omega + \omega_0 >> \omega - \omega_0$. Chapter 5.2.5 showed that Rb-87's resonant frequency sits in the THz, a time scale near incomprehensible to a human. In any measurement that can be detected in a lab, $\exp(i(\omega + \omega_0))$ averages to 0, so these terms can be removed from the equation:

$$i\hbar\frac{dc_g}{dt} = c_e\hbar\Omega^*\left(\frac{e^{i\Delta t}}{2}\right) \tag{6.23}$$

$$i\hbar\frac{dc_e}{dt} = c_g\hbar\Omega\left(\frac{e^{-i\Delta t}}{2}\right), \tag{6.24}$$

where $\Delta = \omega - \omega_0$ is the detuning.

With this in mind, let's go back to the Hamiltonian.

the interaction Hamiltonian

Two things can be done to simplify the Hamiltonian from equation 6.20: the rotating wave approximation can be applied, and the reference frame can be moved to co-rotate with the electric field via the unitary transform

$$\hat{H}_I = \hat{U}\hat{H}\hat{U}^\dagger + i\frac{\partial U}{\partial t}\hat{U}^\dagger, \tag{6.25}$$

where $\hat{U} = \exp\left[i\omega t \left|e\right\rangle\left\langle e\right|\right] = \left|g_+\right\rangle\left\langle g_+\right| + \left|g_0\right\rangle\left\langle g_0\right| + \left|g_-\right\rangle\left\langle g_-\right| + \left|e\right\rangle\left\langle e\right| e^{i\omega t}$. In this frame, and neglecting counter-rotating terms, the Hamiltonian is given by

$$\begin{aligned}
\hat{H} &= (\omega_A - \omega)\left|e\right\rangle\left\langle e\right| + \Omega_L \cos\theta_B \left(\left|g_+\right\rangle\left\langle g_+\right| - \left|g_-\right\rangle\left\langle g_-\right|\right) \\
&\quad - \frac{\Omega_R}{2\sqrt{3}}\left[u_-^* \left|g_+\right\rangle\left\langle e\right| + u_+^* \left|g_-\right\rangle\left\langle e\right| + \text{H.c.}\right] \\
&\quad - \Omega_L \frac{\sin\theta_B}{\sqrt{2}}\left[\left(e^{i\phi_B}\left|g_+\right\rangle\left\langle g_0\right| + e^{-i\phi_B}\left|g_-\right\rangle\left\langle g_0\right|\right) + \text{H.c.}\right], \\
&= (\omega_A - \omega)\left|e\right\rangle\left\langle e\right| + \Omega_L \cos\theta_B \left(\left|g_+\right\rangle\left\langle g_+\right| - \left|g_-\right\rangle\left\langle g_-\right|\right) \\
&\quad - \frac{\Omega_R}{2\sqrt{3}}\left[\cos\chi\, e^{i\psi}\left|g_+\right\rangle\left\langle e\right| + \sin\chi\, e^{-i\psi}\left|g_-\right\rangle\left\langle e\right| + \text{H.c.}\right] \\
&\quad - \Omega_L \frac{\sin\theta_B}{\sqrt{2}}\left[\left(e^{i\phi_B}\left|g_+\right\rangle\left\langle g_0\right| + e^{-i\phi_B}\left|g_-\right\rangle\left\langle g_0\right|\right) + \text{H.c.}\right].
\end{aligned} \tag{6.26}$$

The factors acting on states $\left|i\right\rangle\left\langle i\right|$ are energy terms, which include the energies of the Zeeman shifted $g_\pm$ states as well as the excited state. The next two lines contain the electric and magnetic coupling effects respectively.

While this equation is already simpler than its previous form, it is still quite large, and becomes difficult to interpret for non special cases. Instead, previous work done by the optics group relied heavily on numerical simulation. There are multiple methods that can be used to model scenarios that can be tested in the lab, each with their own strengths and weaknesses. But it is also possible to solve this system analytically.

6.3.2 partially dressed states

The interaction Hamiltonian in equation 6.26 is unwieldy, and it is difficult to extract usable information. This is solely a function of reference frame - moving into a partially dressed state picture will simplify this system to the point of intuitive legibility.

A dressed state transform is equivalent to a coordinate rotation in an N-dimensional coordinate system where N is the number of orthogonal states. In other words, if new states are defined as superpositions of the old states, the Hamiltonian for the new states can be simplified. Partially dressed states refers to a dressed state model that leaves one or more of the original states untouched.

Quantum physics is often the study of quantised waves. In chapter 1.5.1 it was shown that light has no inherent basis state, and neither do atoms. In other words, a dressed state transform is changing the projections, but describing the atom in a way that is equally real to the initial states. This can lead to some interesting interpretations.

Beginning with the Hamiltonian in equation 6.26, it is easily visible that the Rabi oscillations depend on the polarisation of the electric field. Right or left circularly polarised light will only drive one of the $\hat{\sigma}_\pm$ transitions, but a superposition thereof will drive oscillations between the excited state and a weighted superposition of the $\left|g_\pm\right\rangle$ states. It is therefore useful to transform the $\left|g_\pm\right\rangle$ ground states into a coupling

state $|\psi_c\rangle$, which is coupled to the excited state by whatever polarisation is present, and a noncoupling state $|\psi_{nc}\rangle$, which is driven by the orthogonal polarisation, which is absent:

$$|\psi_c\rangle = \frac{1}{N}\left(\cos\chi\, e^{i\psi}\,|g_+\rangle + \sin\chi\, e^{-i\psi}\,|g_-\rangle\right) \tag{6.27}$$

$$|\psi_{nc}\rangle = \frac{1}{N}\left(\sin\chi\, e^{i\psi}\,|g_+\rangle - \cos\chi\, e^{-i\psi}\,|g_-\rangle\right), \tag{6.28}$$

where $N = \sqrt{|u_+|^2 + |u_-|^2}$ is a normalisation constant related to the intensity $E_0^2 N$. The inverse transformation is useful for performing the substitution:

$$|g_+\rangle = \left(\cos\chi\, e^{-i\psi}\,|\psi_{\rm c}\rangle + \sin\chi\, e^{-i\psi}\,|\psi_{\rm nc}\rangle\right)/N \tag{6.29}$$

$$|g_-\rangle = \left(\sin\chi\, e^{i\psi}\,|\psi_{\rm c}\rangle - \cos\chi\, e^{i\psi}\,|\psi_{\rm nc}\rangle\right)/N. \tag{6.30}$$

Substituting these states yields the following partially dressed Hamiltonian:

$$\begin{aligned}\hat{H} = {} & \delta\,|e\rangle\langle e| + \Omega_L\cos\theta_B\left[\cos 2\chi\left(|\psi_{\rm c}\rangle\langle\psi_{\rm c}| - |\psi_{\rm nc}\rangle\langle\psi_{\rm nc}|\right) + \left(\sin 2\chi\,|\psi_{\rm c}\rangle\langle\psi_{\rm nc}| + \text{H.c}\right)\right] \\ & - \frac{1}{\sqrt{2}}\Omega_L\sin\theta_B\Big[e^{i\phi_B}\left(\cos\chi\, e^{-i\psi}\,|\psi_{\rm c}\rangle\langle g_0| + \sin\chi\, e^{-i\psi}\,|\psi_{\rm nc}\rangle\langle g_0|\right) \\ & + e^{-i\phi_B}\left(\sin\chi\, e^{i\psi}\,|\psi_{\rm c}\rangle\langle g_0| - \cos\chi\, e^{i\psi}\,|\psi_{\rm nc}\rangle\langle g_0|\right) + \text{H.c}\Big] \\ & - \frac{\Omega_R}{2\sqrt{3}}\left(|\psi_{\rm c}\rangle\langle e| + \text{H.c}\right),\end{aligned} \tag{6.31}$$

which uses δ to denote the detuning $\delta = \omega_A - \omega$. Additionally, the parameters P and Q have been introduced:

$$P = \left(|u_-|^2 - |u_+|^2\right)/N^2 = \cos 2\chi, \tag{6.32}$$

$$Q = 2u_-u_+/N^2 = \sin 2\chi. \tag{6.33}$$

These parameters are the projections on the poles or equator of the Poincaré sphere. In other words, P describes the ellipticity and is equal to the Stokes parameter S_3, and Q is the polarisations "linearity". Similarly, crosstalk between the ground states can be expressed in terms of the complex hopping rates J and $\bar{J}$:

$$J = \frac{1}{\sqrt{2}N}\left[e^{i(\psi-\phi_B)}\sin\chi + e^{-i(\psi-\phi_B)}\cos\chi\right] \tag{6.34}$$

$$\bar{J} = \frac{1}{\sqrt{2}N}\left[-e^{i(\psi-\phi_B)}\sin\chi + e^{-i(\psi-\phi_B)}\cos\chi\right]. \tag{6.35}$$

These come from the physical interpretation of the dressed state transformation. If a superposition between the two angular momentum state is driven, then the spin of the state will present as the hopping between the superpositions.

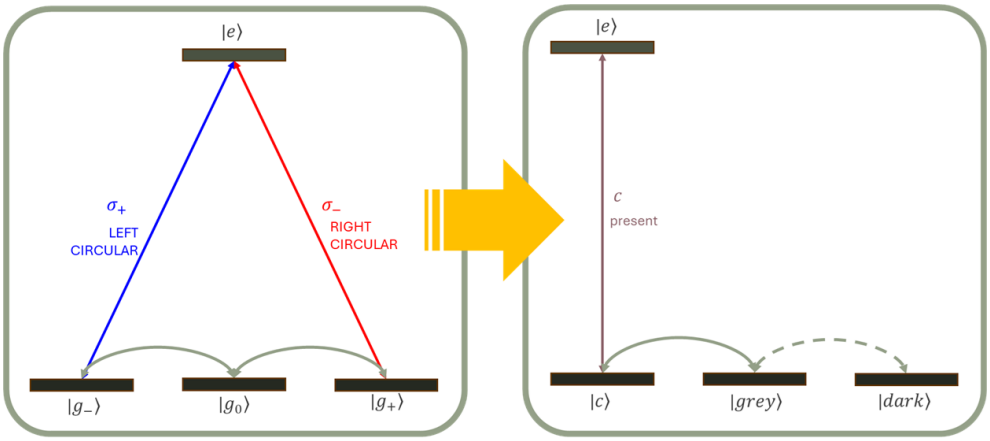

Figure 6.6: Visualising the partially dressed state transformation. The final system is in a "ladder configuration", where the states are in a linear hierarchy, and can only couple to the adjacent states.

It will become apparent that from this point onward ϕ_B and ψ only show up in addition with the other. Part of the reason for this is that they serve the same purpose: ϕ_B is the azimuthal angle of the magnetic field and ψ is the orientation of the polarisation ellipse, as shown in chapter 1.3.1. However, their conventions are opposite: ϕ_B turns clockwise (in +z direction) and ψ anticlockwise. Adding them in the phase term produces real values when the angles (in real space) align, imaginary ones when they differ.

Now the Hamiltonian can be written as

$$\begin{aligned}\hat{H} &= \delta\,|e\rangle\langle e| + \Omega_L \cos\theta_B P\left(|\psi_c\rangle\langle\psi_c| - |\psi_{nc}\rangle\langle\psi_{nc}|\right)\\ &+ \Omega_L\Big[\,|\psi_c\rangle\left(\cos\theta_B Q\,\langle\psi_{nc}| - \sin\theta_B J\,\langle g_0|\right) + \text{H.c.}\Big]\\ &+ \Omega_L \sin\theta_B\left(\bar{J}^*\,|\psi_{nc}\rangle\langle g_0| + \text{H.c.}\right)\\ &- N\Omega_R\big(\,|\psi_c\rangle\langle e| + \text{H.c}\big)/2\sqrt{3}.\end{aligned} \tag{6.36}$$

But wait. This isn't simpler at all! While the atom light interaction has become more straightforward, the magnetic field interaction now couples all three ground states, simply shifting the problem.

To mitigate this, another dressed state transformation is performed. Similarly to before, $|g_0\rangle$ and $|g_{nc}\rangle$ are transformed into one state magnetically coupled to $|g_c\rangle$, and one that isn't. This forms a **ladder configuration**, which is shown in figure 6.6.

The new states are called the grey state $|\psi_g\rangle$ and the dark state $|\psi_d\rangle$:

$$|\psi_g\rangle = \frac{1}{M}\left(\cos\theta_B Q^*\,|\psi_{nc}\rangle - \sin\theta_B J^*\,|g_0\rangle\right) \tag{6.37}$$

$$|\psi_d\rangle = \frac{1}{M}\left(\sin\theta_B J\,|\psi_{nc}\rangle + \cos\theta_B Q\,|g_0\rangle\right), \tag{6.38}$$

where M is a normalisation parameter:

$$M = \sqrt{\cos^2\theta_B|Q|^2 + \sin^2\theta_B|J|^2} \tag{6.39}$$

$$= \sqrt{\cos^2\theta_B \sin^2 2\chi + \sin^2\theta_B(1 + \sin 2\chi\cos(2(\phi_B + \psi)))}. \tag{6.40}$$

Note the grouping of terms in equations 6.37 and 6.38. The linearity Q shows up alongside the longitudinal component of the magnetic field, and its transverse component is always multiplied by the hopping rate. This is related to the two sources of coupling between states: one comes from the nature of the superposition, which is only really a superposition in the Faraday configuration, and one comes from the magnetic coupling in the Voigt configuration when projected onto the propagation axis in circular basis states.

The inverted version is once again more useful for performing the transformation:

$$|\psi_{\mathrm{nc}}\rangle = \frac{1}{M}\left(\cos\theta_B Q\,|\psi_g\rangle + \sin\theta_B J^*\,|\psi_d\rangle\right) \tag{6.41}$$

$$|g_0\rangle = \frac{1}{M}\left(-\sin\theta_B J\,|\psi_g\rangle + \cos\theta_B Q^*\,|\psi_d\rangle\right). \tag{6.42}$$

This final transformation will move the system into the ladder configuration.

interpreting the Hamiltonian

With it, the final Hamiltonian can be written out:

$$\begin{aligned}\hat{H} = {} & \delta\,|e\rangle\langle e| + E_{\mathrm{c}}\,|\psi_{\mathrm{c}}\rangle\langle\psi_{\mathrm{c}}| + E_g\,|\psi_g\rangle\langle\psi_g| + E_d\,|\psi_d\rangle\langle\psi_d| \\ & + \mathcal{J}_{ec}\,|e\rangle\langle\psi_{\mathrm{c}}| + \mathcal{J}_{cg}\,|\psi_{\mathrm{c}}\rangle\langle\psi_g| + \mathcal{J}_{gd}\,|\psi_g\rangle\langle\psi_d| + \text{H.c.}.\end{aligned} \tag{6.43}$$

It is in its abbreviated form for maximum interpretability. Here is a full list of all energy and coupling terms alongside their interpretations:

First, note the terms that are conspicuously absent: $\mathcal{J}_{cd} = \mathcal{J}_{ge} = \mathcal{J}_{de} = 0$. The Hamiltonian has not been diagonalised, but all terms that aren't adjacent to the diagonal have been removed. Therein lies the nature of the ladder system. Most of the remaining terms also go to 0 under certain conditions.

$$E_c = \Omega_L \cos\theta_B \cos 2\chi. \tag{6.44}$$

The Zeeman shift depends on the quantisation axis. In order for the coupling state to be shifted in energy, it has to be in the Faraday configuration and driven by circularly polarised light. The total shift of the system always has to be 0. With this in mind, here are the two remaining states:

$$E_g = -\frac{\Omega_L}{2M^2}\cos\theta_B \sin 4\chi \left[\cos^2\theta_B \sin 2\chi + \sin^2\theta_B \cos 2(\phi_B - \psi)\right], \tag{6.45}$$
$$E_d = -\frac{\Omega_L}{2M^2}\cos\theta_B \sin^2\theta_B \left[\cos 2\chi - \frac{1}{2}\sin 4\chi \cos 2(\phi_B - \psi)\right].$$

Both of them include the term $\cos\theta_B \sin^2\theta_B$ which become 0 at all multiples of $\frac{\pi}{2}$, i.e. Zeeman splitting can only occur if the magnetic field has both a longitudinal and a transverse component. Additionally, $|\psi_g\rangle$ can also be shifted in the Faraday configuration, to counter the shift in the coupling state.

The hopping term between coupling and grey state has been reduced to

$$\begin{aligned}\mathcal{J}_{cg} &= M\Omega_L/2 \\ &= \frac{\Omega_L}{2}\sqrt{\cos^2\theta_B \sin^2 2\chi + \sin^2\theta_B(1 + \sin 2\chi \cos(2(\psi - \phi_B)))},\end{aligned} \tag{6.46}$$

which shows that as the magnetic field's transverse component grows, its azimuthal angle becomes more and more relevant.

The most important term in the entire equation is $\mathcal{J}_{gd}$, the coupling term between grey and dark state.

$$\mathcal{J}_{gd} = -\frac{\Omega_L}{M^2}\sin\theta_B \left[\cos^2\theta_B \sin 2\chi \bar{J} + \sin^2\theta_B J^2 \bar{J}\right]. \tag{6.47}$$

The thing about $\mathcal{J}_{gd}$ is that for some specific configurations, it vanishes. Spontaneous decay is a decoherent process, it can happen at any time in the Rabi oscillations, and when it happens, the atom can decay into any state. If the ground states are all coupled, the atom will eventually find its way back to the coupling state and resume the Rabi oscillations. If they are not coupled, the dark state has earned its name. The atom is locked into a state from which it can't be excited, becoming transparent to the laser light.

To better illustrate, the energies and hopping rates for different χ, θ_B, and ψ are plotted in figures 6.7 and 6.8, respectively.

There are multiple ways to mathematically express this. Here are two approaches.

predicting dark states

A simple way to visualise the absorption rate as a function of θ_B, ϕ_B, χ, and ψ is to model the transition probability from the dark state $|\psi_d\rangle$ to the excited state $|e\rangle$. In its base form, this is known as Fermi's golden rule, but a more accurate result can be obtained by considering all electric and magnetic effects to be weak perturbations of the system [143].

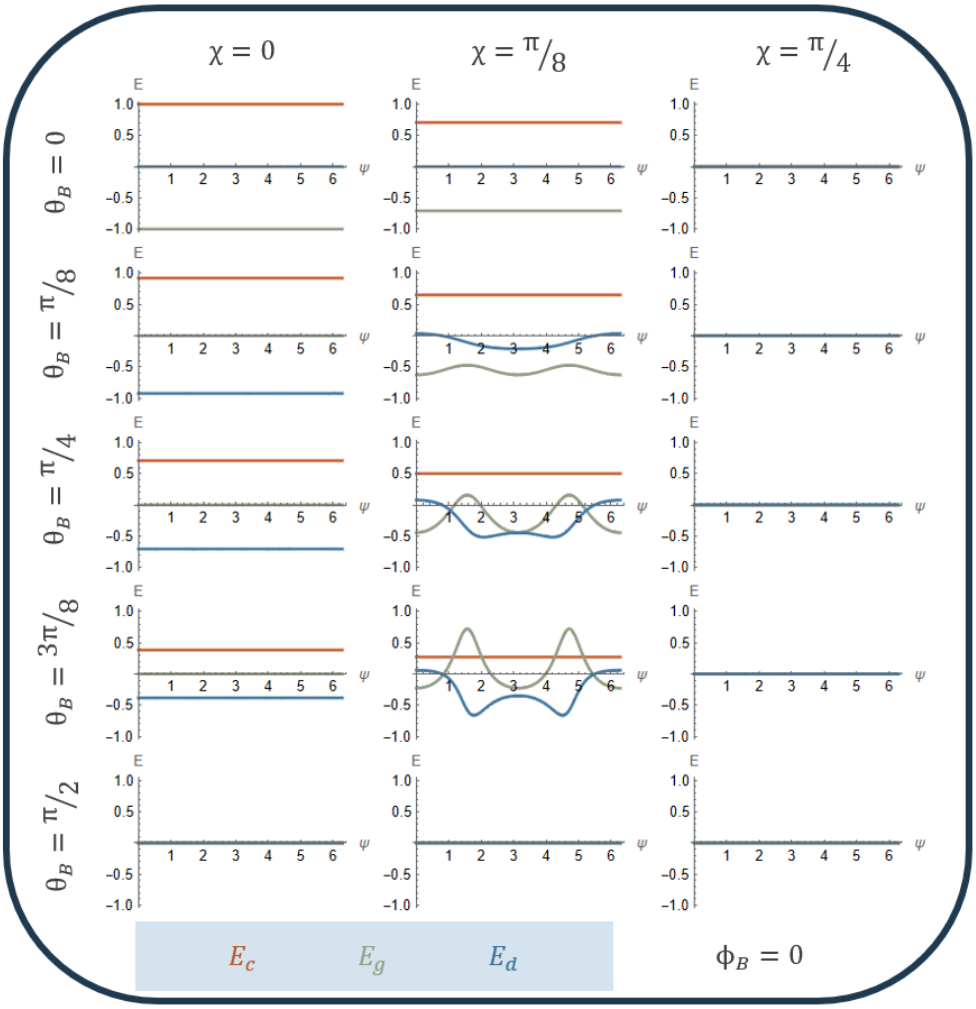

Figure 6.7: Energies of the partially dressed states in terms of χ, θ_B, and ψ, for $\phi_B = 0$. Zeeman splitting only becomes orientation dependent for elliptically polarised light, as linear polarisations don't carry angular momentum, and circular polarisations are rotationally symmetric. The inclination of the magnetic field dictates the modulation of said dependence.

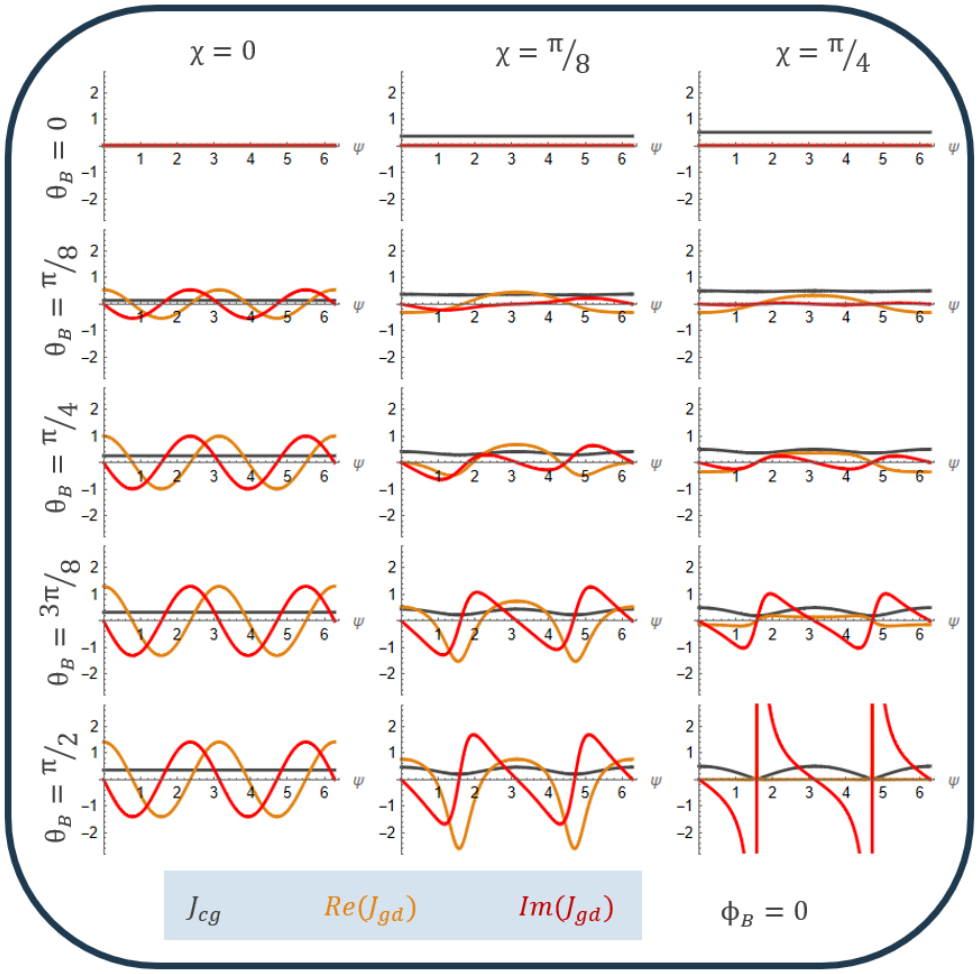

Figure 6.8: Hopping rates of the partially dressed states in terms of χ, θ_B, and ψ, for $\phi_B = 0$. The imaginary component of $\mathcal{J}_{gd}$ goes to infinity for $\chi = \pm\pi/4$, $\theta_B = \pm\pi/2$ $\psi - \phi_B = \pm\pi/2$. The more linear the polarisation, the more symmetrical are the coherences. $\mathcal{J}_{cg}$ can also vanish, but only if the polarisation is linear.

$$P_{e\to d} \;=\; |\langle e|\psi(t)\rangle|^2 \,. \tag{6.48}$$

The transition probability between any two states is $|a_{i\to f}(t)|^2$. To calculate the probability of a system with multiple states, the state vector needs to be is decomposed into all the component states

$$|\psi(t)\rangle = a_e(t)\,|e\rangle + a_{\mathrm{C}}(t)\,|\psi_{\mathrm{C}}\rangle + a_g(t)\,|\psi_g\rangle + a_d(t)\,|\psi_d\rangle\,, \tag{6.49}$$

which can then be put into the Schroedinger equation.

Applying this to the dressed states yields the probability of an atom in the dark state transitioning to the excited state, which is directly related to the electric field absorption:

$$\begin{aligned} P_{d\to e} &= |a_e(t)|^2 \\ &= \left| \frac{\mathcal{J}_{ec}\mathcal{J}_{cg}\mathcal{J}_{gd}}{(E_g - E_d - i\gamma_{gd})(E_{\mathrm{C}} - E_d - i\gamma_{\mathrm{C}d})(\delta - E_d - i\gamma_{ed})} \right|^2 . \end{aligned} \tag{6.50}$$

This method can be used to determine the configurations of states necessary to render the atom transparent: if the transition probability is equal to 0, no light can be absorbed.

the Master equation

The most detailed way to model an atomic system is to use the **optical Bloch equations** (OBE). The optical Bloch equations describe the rate of change in each state of the system via the commutator of the Hamiltonian and the density operator:

$$\dot{\hat{\rho}} = -\frac{i}{\hbar}\left[\hat{H}, \hat{\rho}\right] . \tag{6.51}$$

The density operator was first introduced in chapter 4. It is an N×N matrix describing the probabilities of all states and transitions between them of an N dimensional state space. The diagonal terms ρ_{ii} contain the populations of the states, and the off-diagonal terms ρ_{ij} $(i \neq j)$ are the coherences.

Solving the optical Bloch equations often involves finding solutions for a steady state, i.e. $\dot{\rho} = 0$. This is because time dependent processes on an atomic scale are not really measurable, as seen in chapter 6.3.1

The optical Bloch equations only describe coherent processes. This model aims to describe electromagnetically induced transparency, which depends on decoherent effects [11]. This means a term describing spontaneous decays must be added. These are described by the spontaneous process operators [123]:

$$\hat{\Gamma} = \gamma \sum_i |g_i\rangle \langle g_i| + (\gamma + \Gamma) |e\rangle \langle e| \tag{6.52}$$

$$\hat{\Lambda} = \frac{1}{N_g} \sum_i (\gamma + \Gamma \rho_{ee}) |g_i\rangle \langle g_i| , \tag{6.53}$$

where $\hat{\Gamma}$ is the relaxation operator and $\hat{\Lambda}$ is the repopulation operator. The latter stems from the fact that, as mentioned previously, this Hamiltonian does not describe the process for any given particular atom, but instead is for a particular point in space which is assumed to always be occupied by an atom but not necessarily the same one. This is in line with the Stenholm approach [144]. Here, γ is the natural linewidth, N_g is the number of ground states. Note that $\hat{\Gamma}$ and $\hat{\Lambda}$ don't have any off diagonal elements. They do not describe coherent processes, so there are no coherences.

This form assumes that the atoms sit perfectly still. While this is unrealistic for reasons explained in chapter 7.2, it is a good enough approximation for a system where for every atom that is moved another takes its place, as all the atoms are identical and indistinguishable. In other words, this is not a model for a specific atom but rather a specific position. The spontaneous process operators get attached to the optical Bloch equations like this:

$$\dot{\rho} = -\frac{i}{\hbar}[\hat{H}, \hat{\rho}] - \frac{1}{2}(\hat{\Gamma}\hat{\rho} + \hat{\rho}\hat{\Gamma}) + \hat{\Lambda}. \tag{6.54}$$

An equation of this form goes by many names. Sometimes it is called the **master equation**, sometimes the Liouville equation, sometimes something entirely different. Despite its incredible amount of detail it is used sparingly. This is due to the high complexity of most Hamiltonians, like the one in equation 6.20. Solving the master equation for a system like this using all four variables is as taxing on the computer as it is on the brain.

Once the dressed state model in equation 6.43 was completed, a numerical simulation was written to take advantage of its efficiency. In parallel, work was begun to analytically solve the system to discover further configurations that lead to dark states, and to speed up simulation times.

Some of the results of the numerical simulations are presented in chapter 8 alongside experimental data, as, without the experimental realisation, the research presented in this chapter is only half complete. The theoretical model is based on the experiments that can be performed on the cold atom experimental setup at the University of Glasgow. This one of a kind device probes the $5S_{1/2}F = 1 \rightarrow 5P_{3/2}F' = 0$ transition of the D2 line of ultracold Rb-87 vapours with vector light, which has been the subject of chapter 2.2, making it possible to probe for spatially dependent χ or ψ in a single transmission image. And for the first two years of my PhD, the maintenance of this experiment was my main responsibility.

conclusion of part II

Atoms are inherently quantum. Due to their discrete energy structure, it is impossible to understand them in a classical way, they have to be modeled as quantum mechanical objects. This is why the semiclassical limit is so commonly used to introduce students to quantum mechanics. As they provide a friendly interface between the classical and the quantum world, they also provide a bridge in our minds, which allows us to understand something that is fully unlike what most people experience. Each atom is governed by discrete quantum numbers that describe its size, charge, charge distribution, angular momentum, and therefore its interaction with the world - which for the purpose of this thesis consists of oscillating electric and static magnetic fields.

In chapter 4, it was shown that all understanding of wavelike objects is inherently projective. Put into the context of this chapter, this means that the atom is changed by the fields that surround it. The atom can only be as symmetrical as the space it is defined by, and the electric field of the polarisation as well as the magnetic field provide the quantisation axes of the atom's state space. In other words, the atom itself becomes an interferometer, measuring the fields interacting with it.

This was shown to present in multiple ways. Magnetic fields induce energy changes in the atom's angular momentum states, causing their resonant frequencies to shift. This Zeeman splitting makes it possible to alter polarisation via dichroic absorption or circular birefringence, which can be used to extract information about the magnetic field [145]. If projected transversely to the magnetic field axis, the Zeeman splitting instead presents as Larmor precessions, a hopping between the atomic states. The strength of the magnetic field therefore alters the spectrum: Low magnetic fields see the atom in the Zeeman regime, in which its orientation matters more than its magnitude. Strong magnetic fields, however, can decouple the nuclear spin from the electronic angular momentum, causing the Zeeman splitting to become larger than both the hyperfine interaction, and, for sufficiently large fields, even the Doppler width.

Quantum physics dictates that a superposition is a very real thing, not halfway, but both. Superposition states are often phase dependent - just as light can be expressed in different choices of mutually unbiased bases, two orthogonal atomic states can be redefined as orthogonal superpositions of one another, without losing any touch with reality the description had to begin with. In chapter 6 of this part, this principle was used to reveal a hidden structure within the atoms, responsible for all effects seen in chapter 8. For specific configurations of electric and magnetic fields, it is possible to pump the atom into a dark state, rendering it transparent. The new model makes it possible to find patterns between these states, but this research is still in its early stages.

CONCLUSION OF PART II

As this is a model developed specifically for an experimental system, it is important to discuss them side by side. The final discussion of the results obtained by the partially dressed state model will be presented in chapter 8.

III

state space in a lab frame

Atomic theory revolutionised our understanding of the world as we know it. In the early 20th century, new models and forms of maths and hypotheses and technologies were sprouting up all around the globe, and it was a great time for physics in general.

This paradigm shift was entirely guided by a series of new data, forcing scientists to rethink concepts that had long been taken for granted. The photoelectric effect proved the existence of discrete energy levels, the Stern-Gerlach experiment lead to the discovery of spin, Millikan's oil drop experiment first showed the quantisation of charge, and variants of Young's double slit experiment showed that wave-particle duality does not just apply to light, but all fundamental particles. This is only to name a few - quantum physics was born in the lab.

A theory becomes successful when proven. The scientific method is based on the idea that knowledge about the universe comes from empirical evidence [146]. Theory and experiment are two inseparable sides of the same coin, greater than the sum of its parts. It was experimental evidence that inspired all the theoretical work in part II, as well as validating all the tools used to get there. Now, it is time to return the favour by applying the model in order to predict and show previously unseen effects.

This part of the thesis is split into three chapters. Chapter 7 is essentially an extended method section, going through every major component of the cold atom experiment at the University of Glasgow. This experimental setup is the largest one within the optics group, ideally manned by two PhD students. It investigates the interaction of ultracold ($\approx$ 100 μK) Rb-87 atoms with structured light under the influence of a magnetic field, and is highly versatile in the range of things it can measure. This is seen in chapter 8, where some of the recent data gathered with it is presented and compared to the new theoretical model. The title of said chapter, "Phase Dependent Atom Optics", is a nod to the thesis of my predecessor Aline Vernier, who was instrumental in initially setting up the experiment [147].

Chapter 9 is something entirely new. In this collaboration with Durham University it was shown that atoms provide a unique interface for three dimensional polarisation states which has not been directly measured before. This was alluded to in chapter 3, and goes to show that the choice of quantisation axis of the atomic state space is uniquely suited to revealing otherwise elusive electromagnetic effects.

Lab work is gruelling sometimes, and it is almost necessary to have a podcast or audiobook or something while you work in order to prevent going insane. Lab work is also why I am here. Being able to actively observe with my own eyes the evidence of the laws that govern the universe is a feeling that cannot be compared to anything else. It is worth every second of tedious alignment work. Said grunt work also really makes you appreciate the work of the giants you are trying to climb onto the shoulders of. A new PhD student is scheduled to begin this year, and just one generation after him, the next student he will hand the experiment over to will likely be younger than the experimental setup. It is beautiful to be a part of such a large project.

7 to trap an atom

People often associate "harnessing the atom" with nuclear power, but this is doing the atom a disservice. Atom optics is as versatile as it is ubiquitous. Most famously, atomic clocks are central to the redefinition of the second [111], but atom light interaction is used in quantum computing [148], accelerometry [149], rotation sensing [150], gravimetry [151], search for exotic particles [152], and of course magnetometry. The building blocks of our universe are resourceful like that.

In a way, this chapter is about the groundwork behind the experimental realisation of all the work in chapter 6.3.2 (which predates my academic career by quite a bit), but it is about more than that. When I started my PhD I took over the cold atom experiment with minimal training. There was no formal documentation, no consistent record keeping, nothing. This wasn't anyone's fault in particular, but it made progress on the Optics Group's largest experiment come to a standstill. To prevent this from happening again I began work on a "manual", a shared internal document detailing the setup and functionality of all the experimental components as well as basic procedures and troubleshooting guides. It is by no means complete.

This chapter is an abbreviated version of it, outlining the function of every component, and how they come together to form a state of the art magnetometer. As such, it is more intended as a guide for future students taking over the experiment than experienced thesis reviewers (when I asked Sonja on feedback for this chapter she called it "atom trapping for dummies"). Think of it as an extended method section. I didn't build any of this - in fact, I probably made it quite a bit worse - but it is my work nonetheless.

7.1 Rubidium 87

IN WHICH WE INTRODUCE OUR FAVOURITE ISOTOPE.

Rubidium (Rb) is the 37th element, fifth down in the first column of the periodic table. This makes it an alkali, and an S block element. In its neutral state it has a single electron in its outermost shell, making it highly explosive when it comes in contact with water. It was discovered in 1861 by Robert Bunsen and Gustav Kirchhoff.

Rb is estimated to make up 0.05% of the earth's crust. The majority of commercially available Rb is mined from large lepidolite deposits in Canada and Italy, which are primarily exploited for their Aluminium, as Rb has very few uses outside research. It is solid at room temperature, a state in which it has a silvery grey colour. Its melting point is at $39.9°C$ and its boiling point at 688° C [153].

There are two naturally occurring isotopes of Rb: Rb-85 and Rb-87. The former accounts for 72% of the natural abundance, the latter for 28%. It has 50 neutrons, and it is slightly radioactive, with a half life of 48.8×10^9 years. It β-decays into Sr-87.

The name Rubidium comes from the deep red colour of its emission spectrum. As already hinted by the previous part of this thesis, it is primarily used for research in the field of atom light interactions. This is because the D2 line (see chapter 5.2.3) of both isotopes is driven by light with a wavelength of 780 nm, which is the wavelength of a DVD player diode, making it possible to cheaply build speciality lasers (see chapter 7.3.1) [49]. It is ultimately the spacing of the absorption dips that makes Rb-87 slightly more popular, though both are very common research atoms [121].

7.2 MOTs and SpOTs

IN WHICH ATOMS ARE MAGNETO-OPTICALLY TRAPPED.

In chapter 6.3.2, the assumption was made that the atoms sit perfectly still while experiments are being done on them. This is not the way gases normally behave. Thermal gases are subject to thermal noise and short decoherence times, collisions with each other and, more commonly, the cell walls cause unpredictable changes in momentum. This can be mitigated via things like anti-relaxation coatings [154] but is more commonly resolved by cooling and trapping the atoms.

Light is energy is heat. Laser cooling makes use of this principle by using spontaneous emission to systematically remove all kinetic energy from an atomic (or molecular) gas. It remains gaseous though the individual atoms come to a standstill (nearly). If all atoms are brought to a standstill at the same point, and they can no longer move, they are considered trapped.

There are many types of traps for neutral atoms, such as the optical dipole trap [155] and optical tweezers [156], but one of the most common methods is the **magneto-optical trap** (MOT). They are capable of cooling atomic gases to temperatures as low as 10 μK, and are used to prepare atomic clouds to become Bose-Einstein condensates [112], in addition to being used in many quantum technologies, such as atomic clocks [157], quantum sensing [158, 159] and have seen miniaturisations such as the grating MOT [160]. They are also the reason the cold atom experiment at the University of Glasgow is called that.

7.2.1 MOTs

The magneto-optical trap has two components: a counter-propagating laser beam and a quadrupole magnetic field generated by a set of anti-Helmholtz coils. This section is going to outline how these two fields come together to trap the atoms. To get there, consider the dynamics of atom-light interaction.

If an atom (initially at rest) absorbs a photon the conservation of momentum dictates that the atom gains the photon's momentum, and starts travelling in the photon's propagation direction. The atom is now in its excited state. When it spontaneously emits a photon, the same rules apply. Depending on the direction of emission, the atom will gain momentum in the opposite direction. Only if the emitted photon's propagation axis is the same as that of the original photon will the atom come to a standstill.

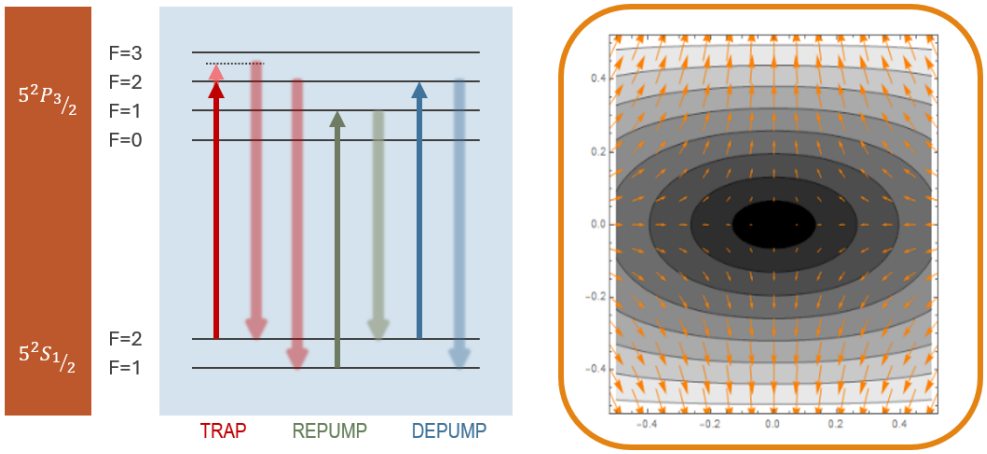

Figure 7.1: Left: level scheme indicating the transitions driven by the different lasers in the MOT/SpOT. Due to the detuning, the trapping beam (in red) can let the atom decay into the F=1 ground state, removing it from the cyclical transition. The repump laser (green) counteracts this process. The depump laser (blue) amplifies it. Right: the quadrupole magnetic field generated by anti-Helmholtz coils is weakest in the centre. It causes a Zeeman shift in the atoms that changes the effective detuning of the trap laser as a function of distance from the magnetic field centre. Image taken from [49] and generated by Adam Selyem.

An atom in motion will experience all light to be Doppler shifted. If it is moving towards the light source, red detuned light will appear closer to the resonant frequency. Absorbing a photon from this source reduces the atom's momentum in this direction. If the driven transition is cyclical, i.e. if the atom is forced to decay back to its original state due to selection rules, this process can occur over and over again. An example of this type of cyclical transition is the $5S_{1/2}F = 2, m_F = +2 \rightarrow 5P_{3/2}F' = 3, m_F = +3$ transition of Rb-87. This process is a form of Doppler-cooling, and for Rubidium, it can cool atoms to temperatures as low as $100\mu K$, but no spatial confinement is happening. This is where the magnetic field comes in.

Magnetic fields cause an atom's magnetic sublevels to experience a shift in energy. This concept was explored in detail in chapter 6.1, and is very useful for exploiting the detuning dependence. Right circularly polarised light drives σ_+ transitions where the ground and excited states have different amounts of angular momentum. This can be exploited by having a spatially varying magnetic field. If the strength of the Zeeman shift increases with the distance from the centre of the trap, then the velocity of the resonant atoms also becomes spatially dependent. Such a magnetic field can be generated by anti-Helmholtz coils, as seen in figure 7.1 (more on this type of coil configuration in chapter 7.3.5). Most traps feature counter propagating beams in all three spatial dimensions, in order to reduce the total velocity of the atoms.

So now, two effects determine the resonance of the atoms with the laser light: The spatially dependent Zeeman shift, and the Doppler shift caused by the atom's velocity. As the laser is red detuned, atoms moving towards the light source will be resonant. The magnetic field Zeeman shifts the energy levels, the further from the

centre of the field, the stronger the Zeeman shift, so to compensate the atoms must be faster towards the outside of the trap in order to be resonant. At the cetre of the magnetic field, where its strength is 0, amasses a blob of atoms with 0 velocity - the atoms are trapped!

The trapped atoms experience no Zeeman shift, as there is no magnetic field at the centre of the trap. This means they also stop interacting with the light, because it is detuned.

However, atoms that do experience a Zeeman shift and also have a velocity can be resonant in more than one way. It is possible for the same beam to excite the atoms into the $5P_{3/2}F = 2$ state (though much less likely) from where they are able to decay into the $F = 1$ ground state. The atom has now been removed from the cyclical transition. This is a problem.

One way to solve this issue is to introduce a second beam that is aligned with the trapping beam. It drives the $5S_{1/2}F = 1 \rightarrow 5P_{3/2}F' = 1$ transition, an excited state from which decay into the $F = 2$ ground state is possible, from where the cooling cycle can resume. To differentiate them, the cooling beam is often called the **Trap laser** and the secondary beam the **Repump laser**. Figure 7.1 shows these transitions contextualised in their level scheme.

Magneto-optical trapping is unfortunately associated with a finite Doppler temperature. This in turn limits the densities that can be achieved in a MOT. Light is energy is heat, and as such, getting the atom into an even lower energy state is the next step for improving the trap.

7.2.2 SpOTs

Left to its own devices, the Trap laser causes a fraction of the atoms to be pumped into the F=1 ground state. While this removes it from the cyclical transition, it also does lower the atom's energy, as the force of the trapping beam on an already trapped atom only causes unneccessary perturbations. This process could be exploited to achieve the desired higher densities, but the atoms are now in a dark state.

Now, sometimes it is actually good to have the atoms in a dark state. All the modelling of atomic state interferometry done in chapter 6.3.2 was done on the $5S_{1/2}F = 1 \rightarrow 5P_{3/2}F' = 0$ transition. In order to test it, the atoms have to be in the $F = 1$ ground state which the Repump beam makes sure they can't stay in. This is unhelpful.

Realistically, the Repump is only necessary at the edges of the trap. The atoms at the centre have already been cooled. For some species of atom, the strong natural line width of certain transitions would see them decay into the dark state almost instantaneously in the absence of a Repump beam, but unfortunately, this isn't the case here. Instead, a third beam, the **Depump laser** could drive the atoms in the centre along the $5S_{1/2}F = 2 \rightarrow 5P_{3/2}F' = 2$ transition, ensuring that the trapped atoms are in the $F = 1$ dark state, ready for the experiment.

This type of modified MOT is called a **Spontaneous Force dark Optical Trap** (SpOT) [161]. The beam configuration is done via a spatial light modulator (see chapter 7.3.3), which holographically "cuts" a hole into the Repump beam and fills it with the Depump beam, as seen in figure 7.2.

Building and maintaining a SpOT is no trivial undertaking. Over the last 20 years, the cold atom experimental setup has seen as many changes as it has PhD students. The beam shaping and auxiliary equipment of just the three trapping beams nearly

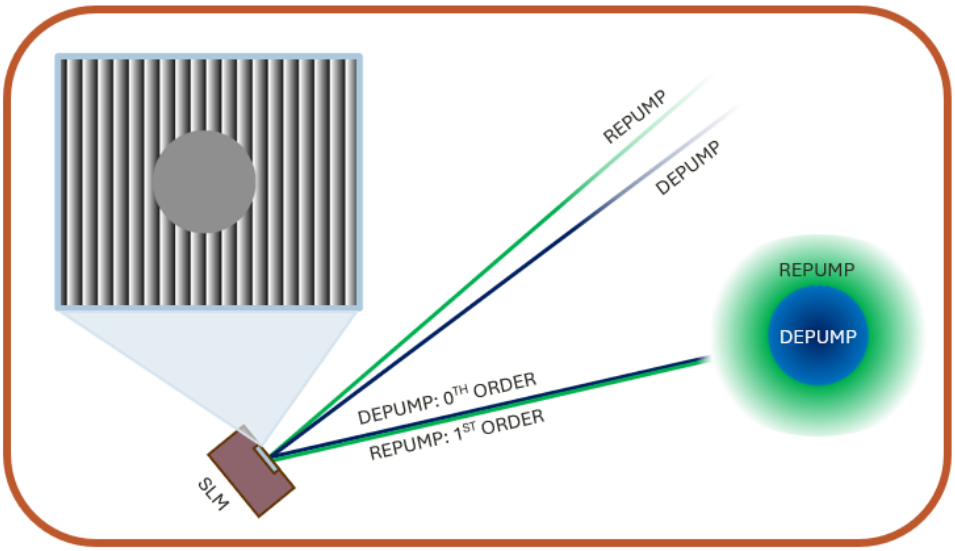

Figure 7.2: Holographic shaping and combining of the SpOT beams via a grating on the SLM. As Repump and Depump have different incident angles on the SLM, their different orders can be combined, so that the beam has a spatially dependent wavelength.

fill an entire large optical table. To truly understand how this type of trap works from an experimental perspective, a few more optical elements have to be introduced.

7.3 the real experiment

THIS SECTION GOES OVER THE SETUP AND METHOD OF THE COLD ATOM EXPERIMENT AT THE UNIVERSITY OF GLASGOW. IT DRAWS HEAVILY ON ADAM SELYEM'S THESIS [49].

The cold atom experiment was initially constructed in 2006 by Sonja Franke-Arnold and Aline Vernier [147]. Since then, while being handed down from PhD student to PhD student, it provided the research for four papers [1, 11, 12, 161], three of them PRLs, and has been the inspiration for theoretical simulations [162]. As of writing, the dynamic switching between a standard MOT and a dark SpOT and the use of the dark state as a starting point for investigations into phase dependent effects, makes it the only experiment of its kind. Once I submit this thesis, it will fall into the capable hands of Kuntal Samanta.

Of course the trap itself is far from the only component in the experiment - each of the component beams of the trap, alongside any probe beams has to be generated, shaped, and tuned. The vapour pressure within the vacuum chamber has to be maintained, the magnetic fields need to be created and controlled, and, of course, the infrastructure to take the measurements has to exist, meaning all the previous components have to respond to each other like clockwork in a highly precise timing

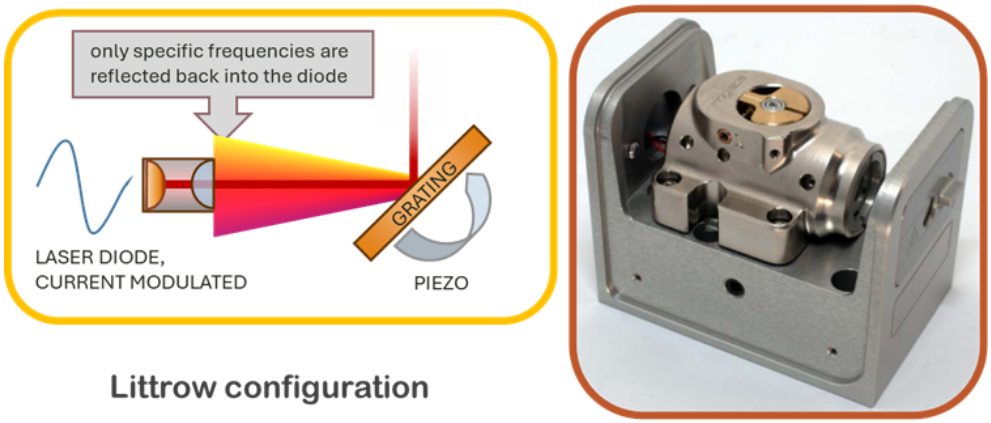

Figure 7.3: Left: schematic of the Littrow configuration, the mechanism by which the ECDL is tunable. The laser diode emits a broadband beam. A piezoelectric transducer controls the angle of a grating, which reflects different frequencies at different angles. Lasing occurs only for the narrow linewidth that is reflected back into the diode. Right: Moglabs CEF cateye.

sequence. In order to keep this experiment functional, these tasks are best done on a daily basis, the system is highly temperamental. This chapter provides only an outline, and for the sake of brevity treats many of its fascinating components as black boxes, further reading is highly encouraged.

7.3.1 external cavity diode lasers and saturated absorption spectroscopy

As explained in chapter 7.2.2, three laser beams of different wavelengths are necessary to construct a SpOT. Each of them has to be produced by a different laser. External cavity diode lasers (ECDLs) are a common choice in atom optics. They are commonly built in house, though commercial models are also available. They are tuneable, which means their frequency has to be specifically selected. Now follows an overview of their mechanism, and how one can ensure that they are tuned to specific hyperfine transitions.

to build an ECDL

A major component of the cold atom setup are the three ECDLs that provide the beams. One a MOGLABS CEF cateye, two homebuilt by my predecessors [163]. Their main advantage is their tunable wavelength and narrow linewidth ($\approx$ 100 kHz) [49]. Here's how they work:

A laser diode emits a fairly broad spectrum of light. A grating is placed in front of the diode in the Littrow configuration as shown in figure 7.3. The grating's angle of reflection is wavelength dependent, so the physical angle of the grating determines the wavelength reflected back into the diode. Stimulated emission now occurs in the very narrow chosen range of the spectrum, i.e. the laser's wavelength can be selected by adjusting the grating angle.

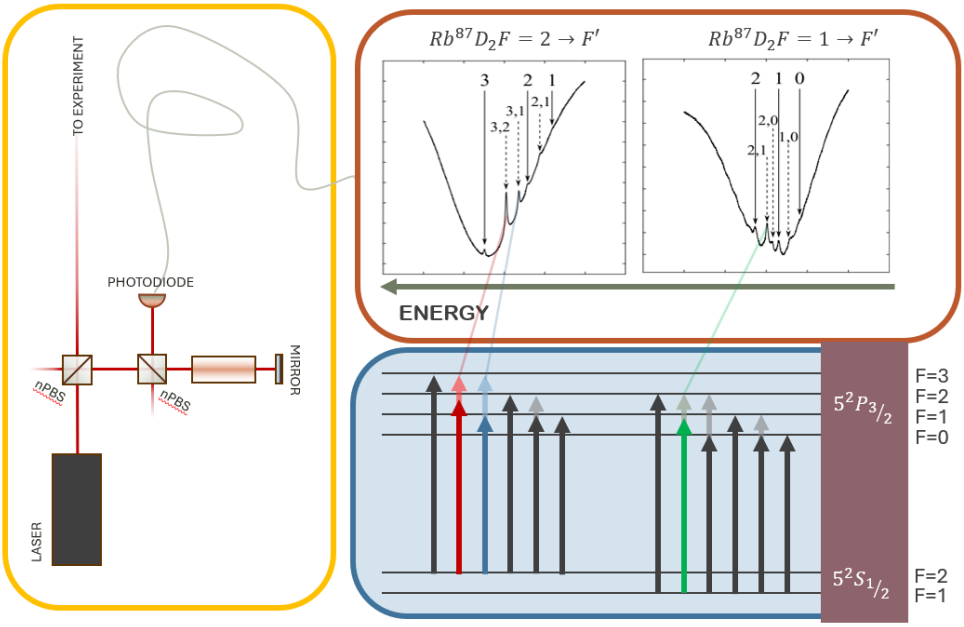

Figure 7.4: Saturated absorption spectroscopy. Left: simplified experimental setup. Top right: Hyperfine spectra with the excited states indicated. Adapted from [49]. Bottom right: corresponding level scheme. The transitions the three lasers are locked to are not the same as those they drive in the experiment, as the crossover peaks are stronger. The crossover peaks that Trap, Depump, and Repump are locked to are indicated in red, blue, and green, respectively.

This angle can be manually adjusted via screws in the horizontal and vertical directions. Additionally, a piezoelectric transducer is used for fine control of the horizontal angle of the grating electronically, allowing for temporal scanning over a small range of frequencies. This is used to tune the wavelength of the laser to drive a specific atomic transition.

Unfortunately, something that can be easily controlled manually can also be easily controlled by random noise. ECDLs are often subject to frequency drift and random fluctuations. While their temperatures are conventionally stabilised using Peltier thermoelectric coolers, this is not enough to ensure that they stay perfectly tuned to a single hyperfine atomic transition. A frequency reference must be used to limit drift - and what's a better reference than the atoms themselves?

hyperfine pumping spectroscopy

Saturated absorption spectroscopy is a method for using the atoms as a frequency reference for the laser. If a laser is scanned through a vapour cell (e.g. Thorlabs GC25075-RB) of room temperature atoms, absorption will occur at resonant frequencies. But since the atoms are thermal, they are moving, and the absorption dips are Doppler broadened to 500MHz. The resulting absorption spectrum shows the fine structure (chapter 5.2.3) of the atoms, but as the standard lab is in the Zeeman regime (chapter 6.1), the hyperfine splitting is smaller than the Doppler width, and

the hyperfine transitions can not be differentiated.

This problem is solved by using a pump-probe configuration. Commonly, both are provided by the same laser; a mirror is placed at the end of the vapour cell. This kind of setup is shown in figure 7.4. To understand the effect of this, consider an atom with a single transition at frequency ω_0, and a laser at frequency ω. In order to absorb the pump laser, the atom needs to travel at velocity $v_1 = (\omega - \omega_0)/k$ where k is the wave number. Note only the velocity component along the propagation axis is considered here. Similarly, the probe beam is absorbed by atoms travelling at $v_2 = -(\omega - \omega_0)/k = -v_1$. If $v_1 = v_2 = 0$, then the absorption rate is reduced according to the relative intensities, as some atoms resonant with the probe beam are already in the excited state from the pump. The beam, after having passed through the cell, is measured by a photodiode. If the laser is scanned through a range of frequencies (often done by applying a sawtooth wave to the piezoelectric transducer), an absorption spectrum is measured. In the Doppler broadened absorption dip will be a spike of reduced absorption at the resonant frequency.

Most atoms have more than one transition, Rb-87 certainly does. This can cause so-called crossover peaks. If the atom is moving at velocity $2kv = \omega_{0a} - \omega_{0b}$ where ω_{0a} and ω_{0b} are the frequencies of the two transitions, another dip in absorption will occur, as driving transition a with the pump will prevent the probe from driving transition b and vice versa. These crossover peaks are often stronger than those of single transitions.

The way these spectra are used to stabilise the laser frequency is via laser locking. The time derivative, or error signal, of the saturated absorption spectrum crosses 0 at the apex of each peak. A device called a **lock-in amplifier** can control the piezoelectric transducer using the error signal: If the signal goes above 0, the laser is blue detuned and the grating position is adjusted. Similarly, if the signal goes below 0, the laser is red detuned. (This is an example. Which way around it is depends on the amplifier and can often be chosen.) Doing this is called **locking the laser**. Figure 7.4 shows that all three lasers are locked to crossover peaks for convenience. This means in order to drive their respective SpOT transitions, their frequencies have to be altered.

7.3.2 acousto-optical modulation

So now the lasers are all locked, but they are at the wrong frequency. Luckily, it is possible to change the frequency of a laser using an acousto-optical modulator (AOM). AOMs have three main components: a piezoelectric transducer, a crystal, often tellurium oxide or quartz, and an acoustic absorber. When switched on, the piezo starts oscillating at a provided radio frequency, inducing an acoustic wave in the crystal. Photons entering the crystal collide with the acoustic phonons and leave with altered momentum, which presents as a change in both wavelength and direction. This is a probabilistic process, every AOM will generate multiple orders - beams with positive changes in frequency are deflected away from the piezo and beams with negative changes towards it. The change in frequency of each order m is shifted by $m \cdot f$, where f is the radio frequency. However, the weighting between the orders is not equal, a well aligned AOM can have up to 80% of the input intensity in the desired order.

The diffraction angle depends on the frequency shift. This becomes a problem when the wavelength needs to be dynamically detuned, like it does for the Trap beam.

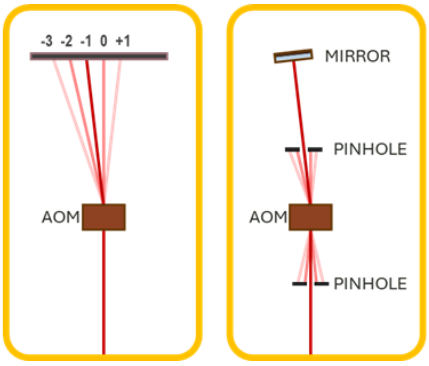

Figure 7.5: Acousto-optical modulation. Right: A single pass AOM aligned for maximum output in the -1 order. All output beams are blocked and labelled. Right: Double pass AOM. The desired order is reflected back into the AOM, leading to a beam with doubly changed frequency counterpropagating to the input beam.

This effect is mitigated via the use of a double-pass configuration. AOMs are usually aligned with the focus of a beam, and the output orders are collimated by a second lens. This standardises the beam path, allowing a mirror to reflect all orders at all angles back into the AOM. If all but the desired order are blocked, it will be deflected twice by the same amount, now counterpropagating with the original beam (see figure 7.5). A QWP before the mirror makes it possible to separate the beams with a PBS.

Unwanted orders are usually blocked, but in one case they serve a secondary purpose: AOMs can be used to rapidly switch the beams on and off. This is central to the timing sequence in chapter 7.3.7 in more than one way - the +1 order of the Depump is used to trigger the the start of the eqperimental sequence via the SLM. Speaking of which -

7.3.3 the spatial light modulator

The spatial light modulator (SLM) has a liquid crystal display that can be shaped into a grating of choice by a LabVIEW program. It is used to dynamically switch the MOT into a SpOT as outlined in chapter 7.2.2 by replacing the centre of the Repump beam with the Depump beam.

The SLM can not be triggered externally with the accuracy the experiment requires, and as such must be the source of synchronisation. But more on that later.

The cold atom experiment uses a liquid crystal on silicon type SLM. It is plugged into the central lab computer as a secondary monitor, and the various LabVIEW programs use it to dynamically display the holographic structures. Most notably is a uniform grating, which reflects the Repump beam into the MOT, and the combination hologram from figure 7.2, which is used to combine Repump and Depump. The hologram is changed once the MOT is loaded, to dynamically switch from the MOT to the SpOT.

7.3.4 probe beam generation

There are three probe beams used in this experiment. Two are used to characterise and optimised the SpOT and one is used for the actual experiments, which are the subject of chapter 8.

The probes for characterising the MOT are confusingly called Probe and Repump probe. They drive the same transitions as Trap and Repump (see figure 7.1), though the Probe is only tuned by a single pass AOM, as it does not benefit from dynamic alterations like the Trap. Each is spliced off the respective laser before the AOM, and they are combined before passing through the centre of the MOT onto the camera.

The experimental beam, or q-Plate beam is named for the q-plate that gives it spatial structure. The m-number of the q-plate depends on the experiment in question. It is spliced off the Trap laser before the AOM, and its frequency can be dynamically controlled via a double pass AOM of its own.

A flip mirror controls the experimental configuration - either Probe and Repump Probe interact with the atoms, or the q-plate beam is shone through the MOT onto the camera.

7.3.5 magnetic fields

There are two separately controlled magnetic fields used on the cold atom experiment. One is the quadrupole field used for magneto-optical trapping as described in chapter 7.2.1, the other a homogeneous magnetic field generated by three orthogonal sets of coils. It is used to cancel out background magnetic fields and also provide the quantisation field for the experiments in chapter 8.

Coils generate a lot of heat, and the magnetic fields they produce depend on their temperature. This is mitigated by a home built current buffer [49].

The rise time of the magnetic field generated by the coils is bigger than zero. Therefore the magnetic fields are turned on 800μs before all other components in the timing sequence.

the trapping field

As mentioned previously in Chapter 7.2.1, the MOT consists of the 3D trapping beam from 6 directions, and a quadrupole magnetic field, which is generated by a set of anti Helmholtz coils, 8 cm in diameter and separated by 4 cm. They have 100 turns [49]. The optimised current is 2.4 A [161], though of course the current driver sets what the coils are actually getting. The point is to create a gradient of about 10 G/cm. They can be rapidly switched on and off by the labview via DAQ cards, though this is subject to the delayed rise time.

the compensation and probing field(s)

Surrounding the vacuum chamber sits a cage of vaguely cubic shape, with a set of coils wrapped around each side to form three pairs of coils that each share an axis, one in each spatial direction. These serve the dual purpose of cancelling out any ambient magnetic fields, as well as generating the desired magnetic field for the experiment. These coils are controlled via the various labview program running the experiment.

The dimensions of the rectangular coils are as follows: height=6.5 cm, width 1 =15 cm, width 2 = 13 cm. Each coil has 30 turns.

In order to not obstruct the view of the cameras, the cage of coils has a tilt of 25° with respect to the beam path.

The ambient magnetic field is subject to changes and fluctuations, and as such recalibration has to occur every time before a measurement. The three sets of coils are independently adjustable. It can be coarsely calibrated by observing the position of the trapped atoms while lowering the trapping field, fine tuned by rapidly switching off the trapping lasers and seeing whether the cloud of atoms dissipates evenly in all directions, and final adjustments can be done using the measurement procedure itself - it is a magnetometer after all.

For all measurements in chapter 8, the magnitude of the quantisation field was set to be 1G, and only the direction was varied.

7.3.6 the vacuum chamber and auxiliary equipment

The centrepiece of the cold atom experiment is a vacuum chamber filled with low pressure Rb-87 gas. The gas is provided by **getters**, a Rubidium wire that, when heated, releases its atoms into the cell. This is only necessary when a sufficient number of the atoms in the cell has been lost due to radioactive decay or condensation on the cell walls.

Figure 7.6 shows a simplified schematic of the equipment surrounding the vacuum chamber. The trapping coils are arranged vertically around the chamber, with the quantisation coils forming a sort of cage around them. The MOT itself is imaged by two CCDs - one from the side, one aligned to also image the probe beams during experiments.

7.3.7 how to run an experiment

We have now gathered all major pieces of equipment. Time to run an experiment.

But before data can be taken, the system has to be optimised. This is done via the following standard procedure:

steps before measurement

First, all three lasers are locked to the respective peaks to check their functionality. Then, the power of Trap and Repump post AOM are checked using a power meter. The Trap should be around 20 mW before split into 3. The Repump should be 8-12 mW before the SLM. The beam shape just before the vacuum chamber is checked using an infrared viewer. Its alignment in both direction is checked using 3D printed alignment aids. The alignment of the probe beams is checked using the camera feed.

Then, the MOT is loaded. Initial alignment optimises the shape of the atomic cloud, the fluorescence of which can be seen on the CCDs. A dedicated Labview program characterises the SpOT by probing the loaded SPOT twice, once with the Probe, load it again, and then with the Repump Probe. From this data it calculates the numbers of atoms in the $F = 1$ and $F = 2$ ground states [49]. The parameters of the circle hologram, such as the radius and the Depump time are optimised at this stage. The final step before each experiment is to adjust the background magnetic field as outlined in chapter 7.3.5.

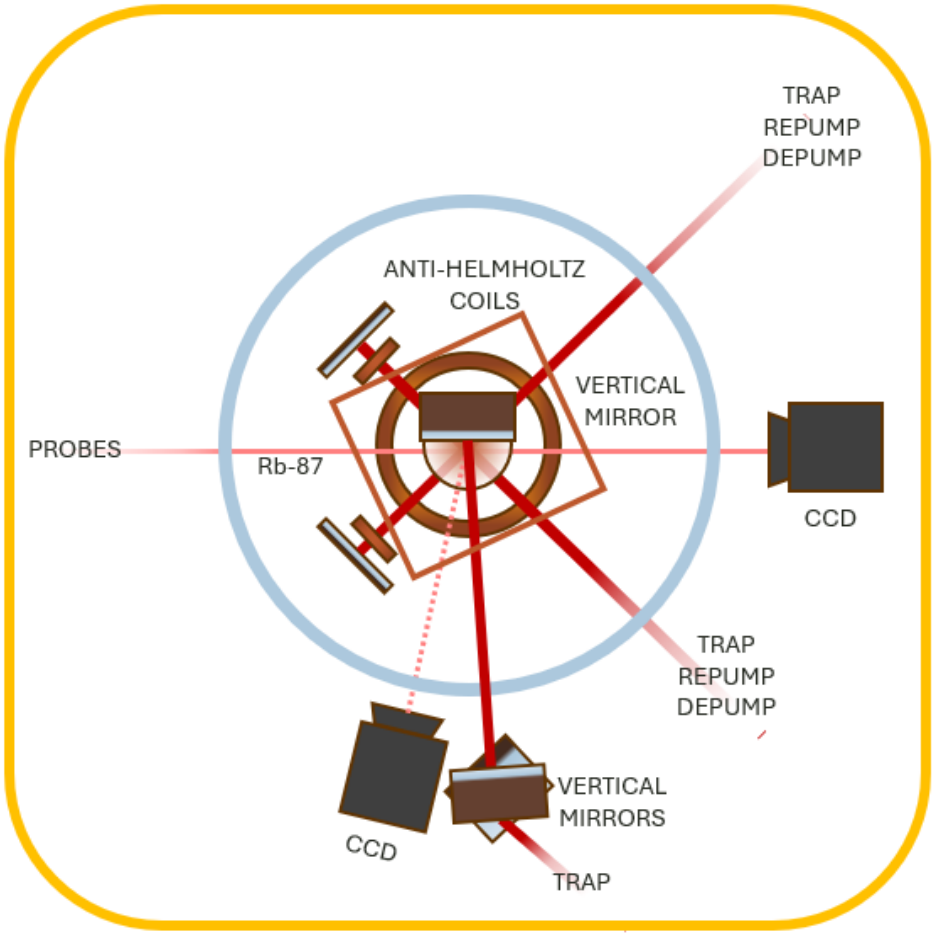

Figure 7.6: Setup schematic of the immediate surroundings of the vacuum chamber. The Trap beam interacts with the atoms from three orthogonal directions (one beam is elevated before being vertically shone into the atoms from above and reflected by a mirror lying flat on the optical table), Repump and Depump from two. The anti-Helmholtz coils are both parallel to the optical table. The rectangle indicates the alignment of the compensation coils. Two CCDs are used to monitor the fluorescence of the MOT. One of them is also in the path of the probe beams, and hence used to take the experimental transmission images.

timing sequence

As mentioned previously, the SLM's internal clock can not be externally controlled. This means that everything else has to somehow be adjusted to the SLM's timing, because once the SLM switches the MOT into a SpOT, everything has to go like clockwork for the data to be useful.

This is where the 1st order mode from the Depump AOM comes in. Until the program is run, it is reflected off a small area at the edge of the SLM onto a photodiode. The photodiode signal is sent to a Schmitt trigger, which sets of the rest of the experimental sequence.

The process begins by imaging the q-plate beam beam to obtain its intensity I_{in}. Then, the atoms are loaded into the MOT for 6s, and transferred into the SpOT for 250 ms. This is when the trapping beams and quadrupole field are switched off, and the cloud is left to expand for 2-5 ms, depending on the experimental run. Two more images are taken: one of the q-plate beam interacting with the cloud of atoms under influence of the quantisation field, and one more of the background, for normalisation [123].

This method has been used to show that the spatially dependent electromagnetically induced transparency is possible [11], that the atomic cloud is itself a magnetometer [12], and that optical concurrence can be transferred into the atoms [1]. How the data is analysed to reveal these patterns deserves its own chapter.

8 phase dependent atom optics

In 2016, while I was scrungling through my high school finals, my pre-pre-pre-predecessors Tom Clark and Neal Radwell first demonstrated a novel effect: spatially dependent electromagnetically induced transparency (SEIT) [11].

The experimental setup outlined in chapter 7.3 does its experiments on the $5^2S_{1/2}F = 1 \rightarrow 5^2P_{3/2}F' = 0$ transition along the D2 line of Rb-87, and this experiment is where all this began. As discussed in chapter 6.3, the $F = 1$ ground state has 3 m_F sublevels, and the $F = 0$ excited state only one, making it a Lambda transition, with three possible transitions (see figure 6.4 in chapter 6). The $\sigma_\pm$ transitions require a change in angular momentum projection, and are hence driven by circularly polarised light. In chapter 1.1.1 at the start of the thesis it was shown that all linearly polarised light can be expressed as and created by superpositions of right and left circularly polarised light, and as the transitions are orthogonal, and two of them require right and left circularly polarised light, it was understood that the $\sigma_\pm$ transitions were the only ones available.

To investigate this dependence, they shone structured beams containing every linear polarisation into the atoms, as shown in figure 8.1. These beams were generated by q-plates, with topological charges ranging from m=1 to m=200, to demonstrate these effects were happening on an atomic scale, and directly dependent on the polarisation profile of the beam. In their resulting paper [11], they showed that the local linear polarisation of a vector beam had a direct impact on whether it was absorbed or not, in other words, the phase between right and left circularly polarised light dictated the nature of the atom light interaction. The results of which are seen in figure 8.1 - the absorption pattern showing a clear dependence on the topological charge, without any losses in resolution.

The problem was that at the time it was not yet understood what caused this phase dependence. To further investigate, they focused on improving the calibration of the compensation coils, to fully remove all trace influences of stray magnetic fields, but to their surprise, when they finally succeeded, the absorption pattern vanished. The team found themselves at a conundrum - and at the edge of a discovery that changed their view of the entire experiment.

8.1 the atomic compass

THIS SECTION IS DEDICATED TO THE PREVIOUS WORK BY FRANCESCO CASTELLUCCI ET.AL. IN [12] IN THE CONTEXT OF THE NEW THEORETICAL MODEL FROM CHAPTER 6.3.2

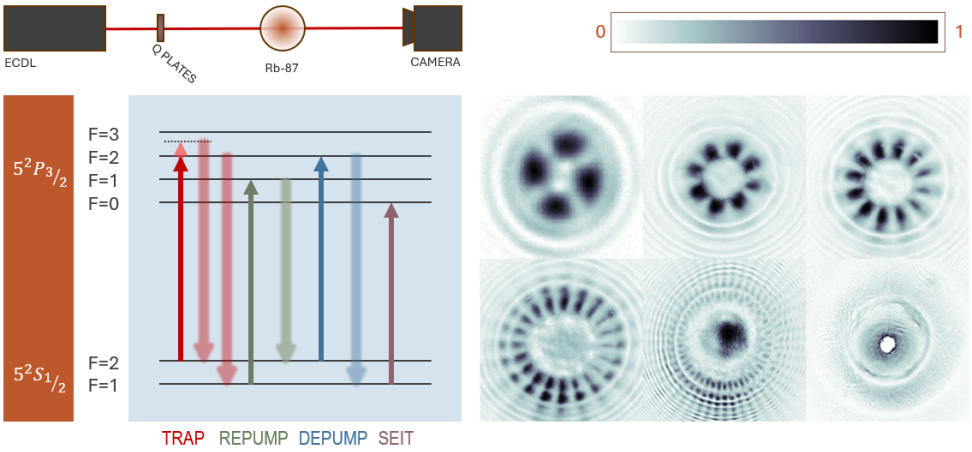

Figure 8.1: Top left: Simplified experimental setup of the SEIT experiment. The following q-plates are used: m = 2, 4, 6, 10, 24, and 200. Bottom left: level scheme of the SpOT beams (see chapter 7.2) and the experimental beam. Right: Optical density of the atoms. Figure adapted from [11, 123].

In chapter 6.3.2, a theoretical model was developed, showing that the coupling between ground states disappears for specific configurations of polarisation and magnetic field angle. If the probe beam only contains linear polarisations, then a special case of $2\chi = \pi/2$ applies, which simplifies the terms of the Hamiltonian from equation 6.43:

$$E_c = E_g = E_d = 0 \tag{8.1}$$

$$\mathcal{J}_{cg} = \frac{M\Omega_L}{2} \tag{8.2}$$

$$\mathcal{J}_{gd} = \frac{\Omega_L}{2N}\cos(\psi - \phi_B)[\cos^2\theta_B - i\sin(\psi - \phi_B)\sin^2\theta_B], \tag{8.3}$$

where E_c,E_g, and E_d are the energies of the coupling, grey, and dark state respectively, and $\mathcal{J}_{cg}$ and $\mathcal{J}_{gd}$ are the hopping rates between coupling and grey or grey and dark state. Ω_L is the Larmor frequency, M the normalisation term, θ_B the magnetic field inclination, ϕ_B the magnetic field azimuthal angle, and ψ the orientation of the polarisation ellipse.

As the q-plate beam only consists of linear polarisations, the Zeeman shift disappears entirely. The dependence of the hopping rates on $\psi - \phi_B$ itself now fully depends on the inclination angle θ_B. For angles $\psi - \phi_B$ the coupling between grey and dark state vanishes, so spontaneous decay causes atoms to be pumped into the dark state, rendering them transparent to it if the magnetic field is transverse.

In other words, the modulation of the transmission pattern depends on the inclination of the magnetic field, and the orientation on its azimuthal angle.

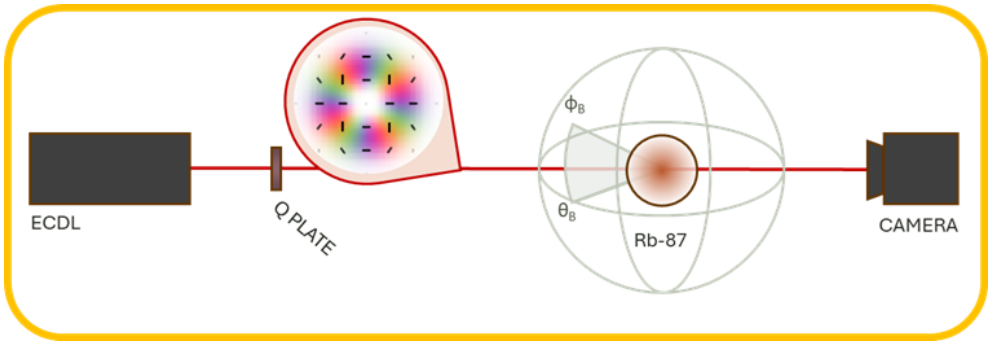

Figure 8.2: Simplified setup for the atomic compass experiment. The twofold beam is generated by a m=2 q-plate. The magnetic field can be freely adjusted in 3D.

8.1.1 the original paper

These are the experimental conditions from the 2021 paper "The atomic compass" [12]. It was found that the phase dependent transparency from SEIT depended on the transverse magnetic field angle with respect to the polarisation. In other words, the optics group had a magnetometer on their hands.

The experimental method followed the standard method of the cold atom table as detailed in chapter 7.3.7. A simplified version of the setup is shown in figure 8.2 The atoms were probed with a twofold beam generated by a m=2 q-plate. Two series of measurements were carried out: At fixed azimuthal angle $\phi_B = 0$, the inclination θ_B is varied from 0 to π. In the second run, ϕ_B was varied from 0 to π while the inclination was kept at $\theta_B = \pi/4$.

The selective absorption due to SEIT can be calculated from a single absorption image. All three images taken during the experimental procedure come together to calculate the **optical density**, which is proportional to the absorption:

$$\text{OD} = ln \frac{I_{probe} - I_{dark}}{I_{atoms} - I_{dark}}. \tag{8.4}$$

This is evaluated pixel by pixel, and visualised in the top part of figure 8.3.

The bottom part of the figure shows another technique that is useful to visualise the data: the "**unwrapping**" of an image. A ring segment of the area of maximum intensity is selected, the same for all beams. Plotting the azimuthal angle φ along the x-axis of a graph produces a stripe with little variation in the radial (or now y-)direction. This makes it possible to reproduce graphs like the ones seen in chapter 6.3.2 from experimental data by "stacking" these stripes for varying experimental parameters along the y-axis. As the beam has an azimuthally encoded ψ, the result is a density plot with ψ on the x-axis and the experimental magnetic field angle θ_B or ϕ_B on the y-axis.

8.1.2 reanalysis and comparison the new states

Given the updated theoretical model, it makes sense to reconsider the data in its context. Figure 8.4 shows the optical density data from [12] juxtaposed with simulations

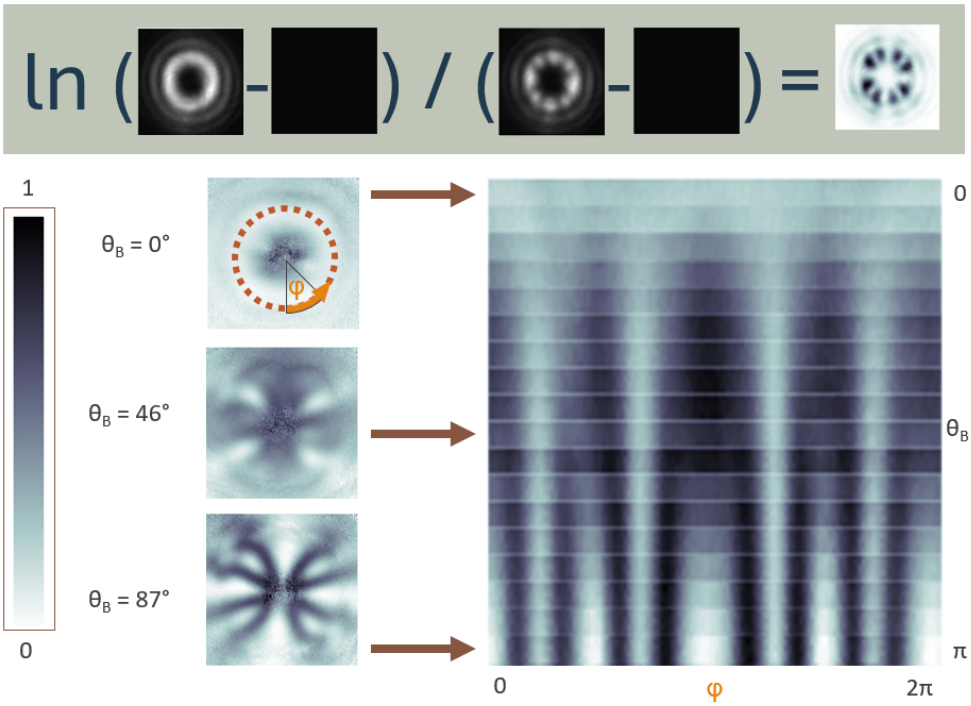

Figure 8.3: Processing of cold atom experimental data. Top: Example of how optical density is calculated. Bottom: unwrapping procedure. A slice corresponding to the area of highest intensity is taken from each image and stitched together in cartesian coordinates to create a density plot of magnetic field inclination θ_B vs polar beam angle φ. The spatial distribution of the optical density depends on the inclination angle of the magnetic field. The processed data is adapted from [12, 164].

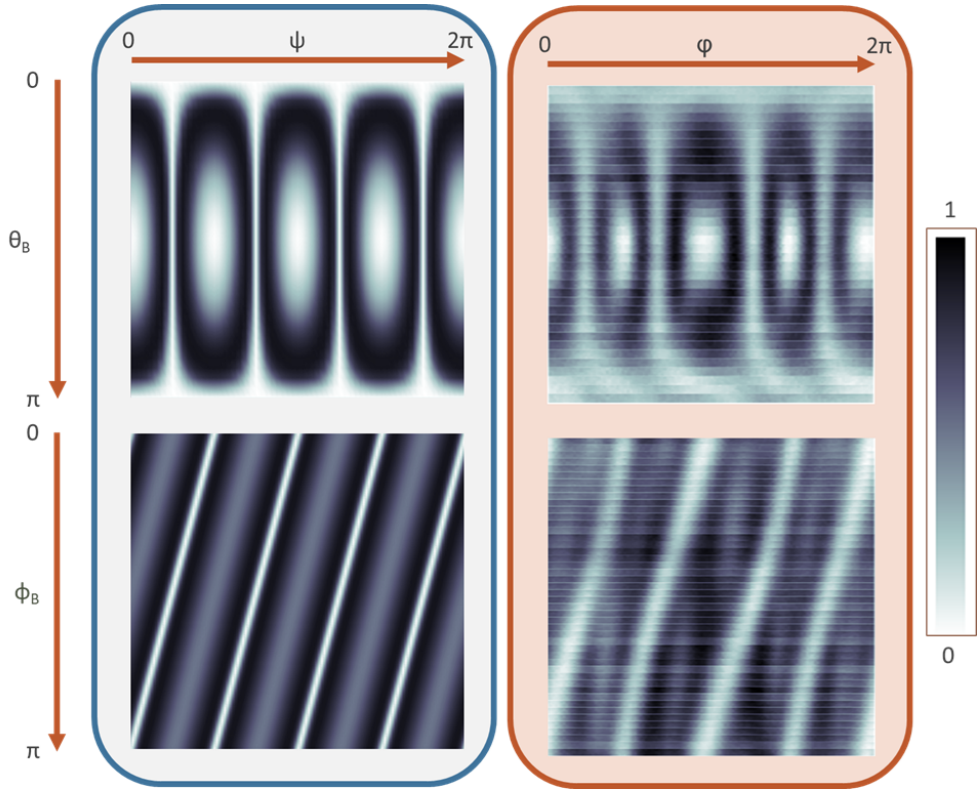

Figure 8.4: Comparison of data from the atomic compass to the new theoretical model. Left: Numerically simulated absorptions generated using the master equation. Right: Unwrapped experimental data adapted from [12], where ψ was encoded in the azimuthal beam angle φ. The top two figures show optical density/absorption as a function of magnetic field inclination θ_B, the bottom two depend on the azimuthal magnetic field angle ϕ_B.

using master equation derived in chapter 6.3.2. In the paper, a previous version of this model was compared to the data by matching the Fourier amplitude and phase to the modulation of the absorption depth $\mathcal{M}$:

$$\mathcal{M} = \frac{max(T_{d\to e}) - min(T_{d\to e})}{max(T_{d\to e})}. \tag{8.5}$$

This metric is very useful for comparison between the different methods of simulation.

Of more interest in the context of this thesis are however its theoretical implications. This paper was the inspiration for all theoretical work in chapter 6.3. Figure 8.4 shows that the data validates the partially dressed states model.

The method by which the magnetic field is measured in this experiment is unconventional, to say the least. Optical magnetometry is a broad field, featuring many different approaches [165]. Magnetometers based on cold atoms are capable of self-

calibration [166], measuring magnetic gradients [167], and dynamically cancelling magnetic fields in three dimensions [168]. But within the different approaches, homogeneity is found. For example, optically pumped atomic magnetometers are most commonly based on observations of the Larmor precession of the atomic spins polarised by the magnetic field [169–171]. In contrast, vector magnetometers usually employ radio-frequency modulation in order to map the vector components onto different harmonics [172–174]. Though it was also shown that an EIT based vector magnetometer can detect multiple components of the magnetic field [175].

The atomic compass forms the basis of an exciting new international research project the University of Glasgow is involved in, which is intended to lead to a minituarised magnetometer based on the same principles, with an intended application in geophysics, though it also seems promising for biomedical applications. However, in this section only the magnetic field parameters θ_B and ϕ_B were discussed. This leaves the Poincaré sphere coordinates (or polarisation ellipse parameters χ and ψ entirely undiscussed. Time to do something about that.

8.2 transfer of optical concurrence to atomic clouds

IN WHICH OPTICAL CONCURRENCE IS MEASURED BY AND TRANSFERRED TO A CLOUD OF ULTRACOLD ATOMS. THIS WORK WAS DONE UNDER THE GUIDANCE OF JINWEN WANG IN THE EARLY MONTHS OF MY PHD, AND PUBLISHED IN [1].

The highest modulation in the atomic compass paper occurs for magnetic field inclinations of $\theta_B = \pi/2$, or transverse magnetic fields. This means that this is the configuration in which the three other factors have the biggest amount of influence on the transparency on the atoms.

In this chapter, the influence of the spatial dependence of the beam on the modulation or Fourier amplitude of the transparency of the atoms is explored. A transverse magnetic field lends itself to this investigation. For the assumptions $\theta_B = \pi/2$ and $\phi_B = 0$, the partially dressed state model from chapter 6.3.2 simplifies, and the terms in the Hamiltonian become:

$$E_c = E_g = E_d = 0 \tag{8.6}$$

$$\mathcal{J}_{cg} = \frac{M\Omega_L}{2} \tag{8.7}$$

$$\mathcal{J}_{gd} = -\Omega_L J(\cos 2\chi \cos(\psi) - i\sin(\psi)). \tag{8.8}$$

Due to the fact that the magnetic field is now orthogonal to the propagation axis, all Zeeman splitting has disappeared. The hopping rates between the three ground states have significantly simplified, and the ellipticity $\cos 2\chi$ entirely determines whether $\mathcal{J}_{gd}$ has a real component or not. In the partially dressed state model, ϕ_B and ψ only ever show up in relation to one another. As only their relative phase matters, the interaction can be simplified by setting $\phi_B = 0$ without losing generality in scenarios that involve every value of ψ.

The theoretical framework from chapter 6 simulates the interaction on an atom

to atom basis. This microscopic view is highly useful from the perspective of the atom but runs counter to one of the main lessons from chapter 2: a beam propagates and interacts as a whole. Each of the photons that make up a laser beams is identical to all others and has the intensity and polarisation structure of the overall beam. In other words, the spatial structure of the beam is reduced to the sum of its parts, instead of the classical equivalent of quantum entanglement it is known for.

The concept of optical concurrence was first introduced in chapter 2.2.1. It serves as a measure of the correlation of two degrees of freedom within the atom - the polarisation and the spatial position. A twofold beam, like the ones discussed in chapter 2.2, consists of two LG of equal and opposite circular polarisations:

$$|\Psi_2\rangle = \frac{1}{\sqrt{2}}\left[LG_0^2\,|R\rangle + LG_0^{-2}\,|L\rangle\right]. \tag{8.9}$$

The intensity of this beam solely depends on the radius. For its polarisation, the opposite is the case: Its polarisation is radially uniform, but it is tied to its azimuthal angle φ. In other words, this beam wraps around the equator of the Poincaré sphere four times, making it a vector beam that covers all possible values of ψ. It has a concurrence of 1.

All of this however changes if the component LG modes are not equally weighted. A beam created from the same modes but with unequal intensities will still have the same correlation between φ and ψ, but its trajectory on the Poincaré sphere will be different: it will now wrap around a smaller circle that is parallel to the equator. It is no longer a vector beam. Its concurrence is smaller than 1. Mathematically, this is equivalent to introducing χ into equation 8.9:

$$|\Psi\rangle = \cos\chi LG_0^2\,|R\rangle + \sin\chi LG_0^{-2}\,|L\rangle. \tag{8.10}$$

For a beam of this form, the concurrence becomes directly related to the polar angle of the Poincaré sphere:

$$C = \sin 2\chi. \tag{8.11}$$

So this is a type of beam that spatially covers all values of ψ for different values of χ - ideal for investigating the relationship of the polarisation structure on the spatially dependent electromagnetically induced transparency.

8.2.1 experimental procedure

As the concept of the concurrence measurement is complementary to that of the atomic compass, their methods are variants of one another, too. The base setup and method follow that outlined in chapter 7.3, but with the following specifications:

The magnetic field is kept transverse in the $\hat{x}$ direction, with a fixed magnitude of 1G. The experimental probe beam is generated with a $m = 2$ q-plate placed after a QWP. The QWP controls the ellipticity of the beam going into the q-plate and hence the weighting of the component LG modes of the beam going into the atoms. The intensity of the probe beam is 0.2μW. A simplified version of the setup is seen in figure 8.5, alongside Stokes images of the beams used in the experiment.

As the aim of the experiment was to investigate the dependence of the absorption pattern on the beam structure, the absorption image was analysed for its spatial

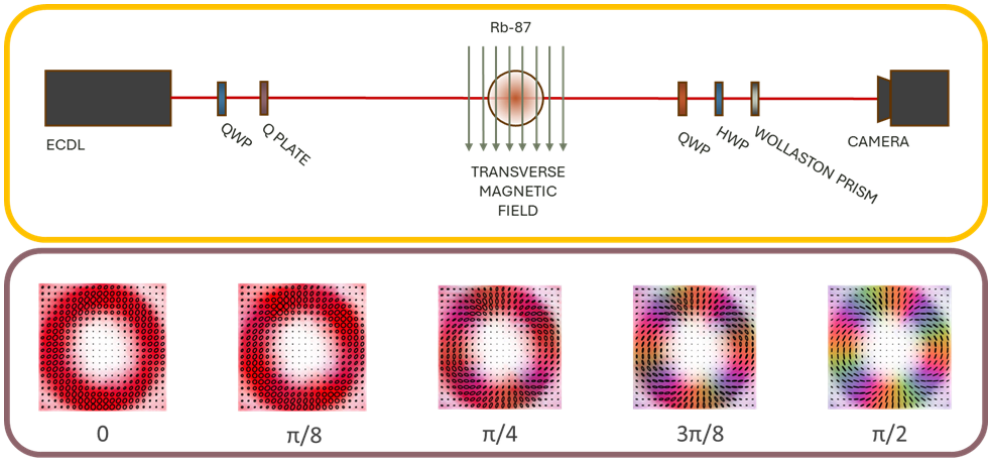

Figure 8.5: Top: Simplified setup used in the concurrence experiment. A Stokes measurement can be performed. Bottom: experimental images of the beams used. The QWP before the q-plate makes it possible to change the ratio of the LG modes comprising the beam. If they are equal, the beam has a twofold structure.

dependence as a function of the probe beam's Poincaré sphere angle χ. In the paper, this was compared to numerical simulations using previously existing theoretical models. But a deeper understanding can be gleamed from the partially dressed state model.

8.2.2 spatially dependent state space

Both simplified hopping rates in equations 8.7 and 8.8 have two terms - one that depends on χ and one that does not. However, their relationships to it are quite different: $\mathcal{J}_{cg}$ is biggest for linearly polarised light, but always real and bigger than 0. Quite the opposite is true for $\mathcal{J}_{gd}$, where χ has an influence on whether the term is real or imaginary that is as big as that of ψ. In this configuration, it is possible for $\mathcal{J}_{gd}$ to become fully imaginary.

As the beams contain all possible values of ψ, the range of the hopping rates is determined by χ, which is constant across the beam. Figure 8.6 shows the experimental data juxtaposed with simulations done using the new dressed state model, as well as the previous model. In order to reduce noise in the measured modulation depth, it was extracted via a Fourier series expansion [176], as the modulation is identical to the $\ell = 2$ Fourier coefficient of the transition probability $P_{d\to e}$ (see chapter 6.3.2). This allows the measured images to be directly compared to the curves predicted by perturbation theory and the master equation.

The data shows that the modulation in transmitted beam intensity directly depends on χ, and hence the concurrence. The concurrence has changed degree of freedom, polarisation modulation has turned into intensity modulation. This is something the camera is able to detect, so this means it is possible to measure the concurrence from a single absorption image.

In the context of this thesis, this data serves the dual purpose of demonstrating the single shot measurement of optical concurrence while also experimentally vali-

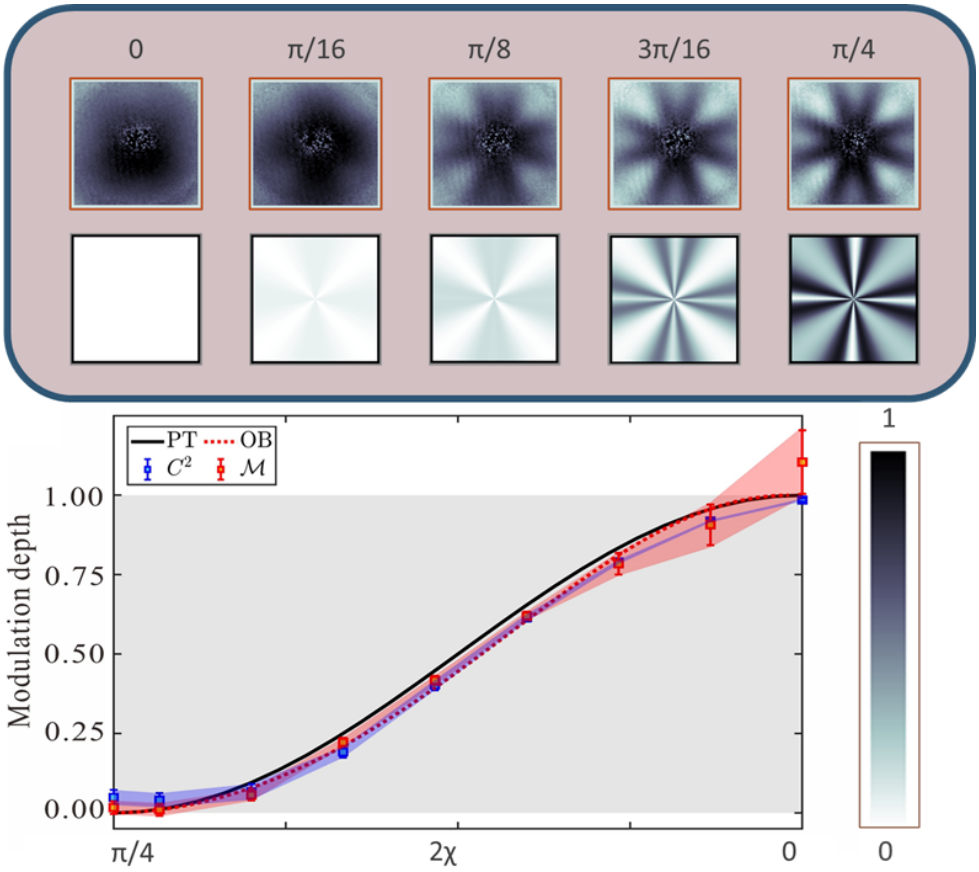

Figure 8.6: Top: measured (top row) vs simulated (bottom row) optical density of beams with varying concurrence. The difference in overall intensity is most likely due to a difference in normalisation procedure. The change in fringe modulation however is in agreement. Bottom: Fringe modulation as a function of concurrence. PT: perturbation theory. OB: optical Bloch equations. C: concurrence. $\mathcal{M}$: modulation. Adapted from [1].

dating the partially dressed state theoretical model. Qualitatively, the data perfectly agrees with the simulations carried out using the master equation, showing that this is a valid method for the prediction of spatial absorption patterns.

As the transparency is tied to the state occupied by the atom, the other implication of the data is that the atomic cloud itself has become spatially dependent. Its population now carries concurrence, but not just that - its very state space depends on the parameters of the input polarisation structure, as the partially dressed state model's redefinition of states is a function of the spatially varying Poincaré sphere trajectories.

While only a specific selection of beams generated from a single set of components was used in this setup, optical concurrence can be carried by many types of beams. Not only can the concurrence with any beam be measured this way, but it might also be applicable for measuring other parameters in spatial beam structure, such as Skyrmion numbers [13].

Of course, this method is not exclusive to atoms. Similar processes have been shown to be generalisable to systems including atomic BECs [177–179], ions [180, 181], and molecules [182]. In other words, concurrence is measurable with any system capable of polarisation dependent atom-light interaction.

Mathematically, concurrence is the classical analogue to quantum entanglement. This means that the transfer process as demonstrated in this chapter is a simulation of the transfer of quantum entanglement into another medium with different degrees of freedom. This effect, too, is therefore reproduceable with any of the systems listed above. In fact, it suggests that it could be possible to create entanglement between state spaces.

9 driving an atomic transition with longitudinally polarised light

Light is not inherently paraxial. In chapter 3, it was shown that longitudinally polarised light can be created by focusing a beam with a radial polarisation component. Despite this, it has been conspicuously absent from all chapters since then, being omitted from all forms of polarimetry and models of atom light interaction.

Unless the interacting medium sits within the focal region of a strong lens, the paraxial approximation is a reasonable one, the longitudinal component of most beams is vanishingly small and assuming it to be zero simplifies the maths significantly. But the flip side of this is that longitudinally polarised light remains poorly studied. Conventional detectors such as CCDs and photodiodes are not able to pick it up, its propagation cannot be modelled the same way as transversly polarised light, and all previous attempts of measuring it had to rely on indirect methods such as reconstructing the full 3D field from Mie scattering off a microscopic particle [89, 90], illuminating gold nanoparticles with radial beams and supressing the forward scattering [85], inferring the presence from the fluorescence patterns of single molecules with fixed absorption dipole moments [86, 87], interactions with molecular monolayers [88], or via the medium of angular momentum states of particles in optical tweezers [183].

Thinking of light as three-dimensional recontextualises some things. In chapter 6.1, it was shown that there are three different flavours of dipole transitions available to atoms: $\sigma_\pm$ transitions which alter the atoms magnetic quantum numbers, i.e. the angular momentum projection, and π transitions, which do not. The optical polarisations driving these transitions have to be orthogonal to one another, and depend on the angle of the external magnetic field with respect to the propagation axis. If the system is in the Faraday configuration, i.e. if the magnetic field is aligned with the propagation axis, the angular momentum required to drive the $\sigma_\pm$ transitions comes from right and left circularly polarised light. In the paraxial limit, $|R\rangle$ and $|L\rangle$ are a complete set of basis states, meaning the π transition is unavailable. But there is a polarisation that is orthogonal to both circular polarisations: longitudinally polarised light.

In the Zeeman regime, which has been introduced in chapter 6.3, and used as the backdrop for all theoretical and experimental work done so far in this thesis, the Zeeman shifts are (usually) smaller than the Doppler width. This makes it more difficult to tell which transition is being driven, instead of using detuning, one has to fall back on things like spatial encoding (as demonstrated in chapter 8) or squeezed states. Unfortunately, this only works for light that propagates. In order to show longitudinally polarised light exists, a medium is needed that interacts exclusively

with it.

The hyperfine Paschen-Back regime, which was introduced in chapter 6.2, occurs for magnetic fields that are sufficiently strong that the Zeeman shift exceeds the hyperfine splitting. For Rb-87, the HPB effect emerges at magnetic fields of 0.23T [184]. A magnetic field of 1.6T splits the spectrum so much that the individual transitions are considerably further apart than the Doppler width. As a result, the spectrum has distinct absorption dips for the different transitions that are fully resolved in frequency space, and the spectrum depends on the angle of the magnetic field to the propagation axis. The resulting spectra are shown in figure 6.3 in chapter 6.2. In the Faraday configuration, the π transition is normally considered unavailable. The π transition is driven by light polarised along the magnetic field, which is the same as the propagation axis. The π transition can be driven by longitudinally polarised light.

9.1 the "Durham experiment"

IN WHICH THE SETUP AND EXPERIMENTAL PROCEDURE OF THE STRONG FOCUSING EXPERIMENT ARE DISCUSSED. THIS SETUP WAS PIONEERED BY CLARE HIGGINS, IFAN HUGHES, AND DANIELLE PIZZEY AT THE UNIVERSITY OF DURHAM, AND THEN ADAPTED FOR STRUCTURED LIGHT BY SONJA FRANKE-ARNOLD AND MYSELF.

So selection rules predict that the π-transition can be driven by longitudinally polarised light, which has no angular momentum. For the same reasons, this transition is normally unavailable in the Faraday configuration (see chapter 6.1).

In order to test this hypothesis, an experimental setup was constructed. The project is a collaboration between the Optics Group of the University of Glasgow and the Quantum, Light & Matter Group from Durham University, where the initial version of the experiment was conceived. After its arrival in our Atoms Lab, it took on the nickname "the Durham experiment", and it stuck because it makes it sound cool and mysterious.

Figure 9.1 shows the full version of the experimental setup. It consists of the following components:

The beam is generated by a distributed feedback (DFB) laser with a central wavelength of 780 nm, which scans over a range of 100 GHz, enough to encompass all transitions in the HPB regime. The scan has the shape of a triangle wave and has a period of 10s. In order to turn the beam profile into a more Gaussian shape, the beam is spatially filtered by a 50 μm pinhole, and its vertical polarisation ensured by a polarising beamsplitter. A small portion of the beam is spliced off using a HWP and PBS in order to centre the scan around the absorption dips of a Rb vapour cell by tuning the laser so the Doppler broadened absorption dips of the D2 line are centred on the oscilloscope (not shown in the diagram).

As the radial component of the initial beam is proportional to the longitudinal component at the focus, it can be helpful to directly control the beam's radial and azimuthal components. Radially and azimuthally polarised beams are generated by an m=1 q-plate after a HWP. The angle of the HWP dictates the strength of the radial component. Alternatively, beams with spatially varying radial and azimuthal components can be generated by a m=2 q-plate. In this case, additional structures can be generated by inserting a second HWP after the q-plate.

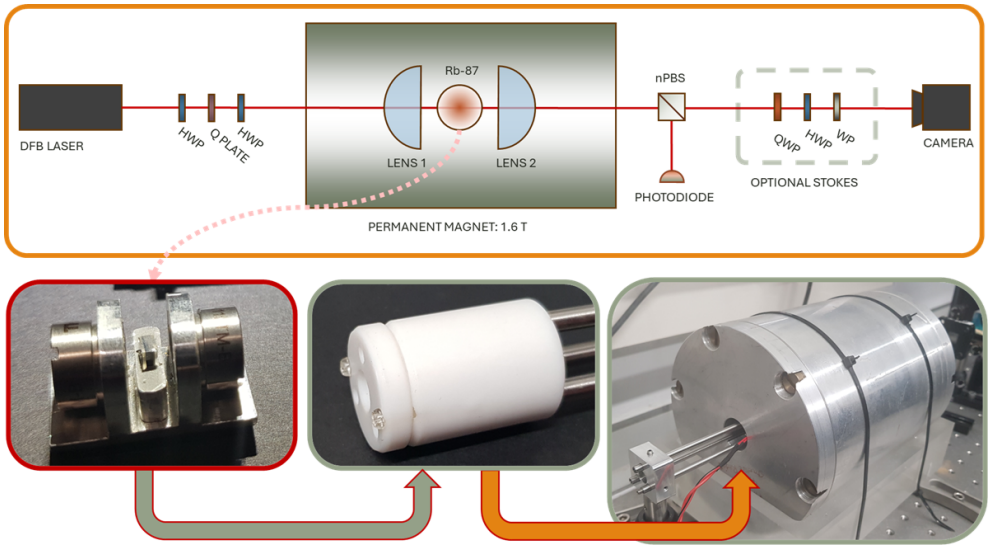

Figure 9.1: Experimental setup of the strong focusing experiment. Top: simplified setup schematic with all optional components. The first or second HWP can be removed, depending on the beam generated. For measurements with the camera, the non-polarising beam splitter (nPBS) is removed in order to reduce influence on the polarisation. The components for Stokes measurements are only used for the measurements in chapter 9.4.1. Bottom: photos of the actual cell holder with lenses and mm^2 cell, its teflon unit, and how it is inserted into the magnet.

The centrepiece of the experiment is a neodynium (NdFeB) magnet, a permanent magnet made from an alloy of neodymium, iron, and boron [130]. It has a borehole, at the centre of which the homogeneous magnetic field, which is parallel to the hole, measures 1.6 T. This is where the strong focusing contraption will be inserted. The Rb-87 atoms themselves are contained in a 1mm^3 vacuum cell, which sits atop a small mount which also contains two NA=0.4 lenses in a 2f configuration [33], with the vapour cell at the focus. It has a hole for a cell heater, as the experiments are performed at temperatures between 75° and 85° in order to increase the atomic density and hence the interaction strength. The mount itself is in turn contained in a Teflon/copper unit, which is mounted to alignment rods. Once the device has been inserted into the magnets, its position can be fixed in place such that the propagation axis is parallel to the magnetic field.

Before entering the magnet, the beam has a waist of 1.3 mm and a maximum intensity of 2.2 nW/m^2. The focal length is 7mm, making the effective numerical aperture 0.3537. This means the beam is focused at an angle of α = 0.2382π rad, or = 42.8789°, and has a spot size of 0.1337 μm at the focus.

Depending on the set of measurements, the resulting beam is either recorded by a photodiode and displayed and processed by an oscilloscope, or spatially imaged using a CCD. The CCD can take videos of the beam, with 304 images in a full scan cycle. As the beams have spatially varying polarisation profiles, there is the option for Stokes polarimetry (chapter 2.3) - using a Wollaston prism instead of a polariser allows for the projection of orthogonal Stokes bases onto different areas of the camera. This is invaluable for the syncing of the separate videos, as integrating over the full frame of the camera will give the full beam intensity. The latter can then be plotted and compared as a spectrum.

Another hurdle in the analysis of the videos are the intensity fluctuations over the scan of the laser. The spectrum generated by integrating over each frame can be normalised by fitting a fifth order polynomial to the slope, but excluding the transitions. Figure 9.2 shows a spectrum obtained this way and the polynomial used to normalise it. The transitions used for data analysis are also standardised, and chosen for optimal agreement between different videos.

Alignment procedure

In order to optimise the system it has to be ensured that the optical axis, the centre of both lenses and cell, and the magnetic field axis, coincide. To achieve this, a procedure with multiple steps has been devised:

The first alignment step takes place during the initial setup of the experiment, before the lens-cell-contraption is inserted into the magnet. For this initial alignment, two 3D-printed alignment aides, each with a hole of 3 mm, are fitted into each side of the magnet's bore hole. The beam is aligned through these holes.

Then, the focusing of the beam through the cell is optimised on the cell holder, before it is inserted into the magnet. Once inside, its position is controlled and ultimately fixed via the alignment rods. At this stage, alignment is optimised for beam shape by monitoring it with the camera. Once this has been achieved, fine tuning can begin.

Observing the absorption of longitudinal polarisation itself can be used for fine tuning: As azimuthally polarised light carries no longitudinal component, the π transition can not be driven if the propagation axis and magnetic field are parallel, so

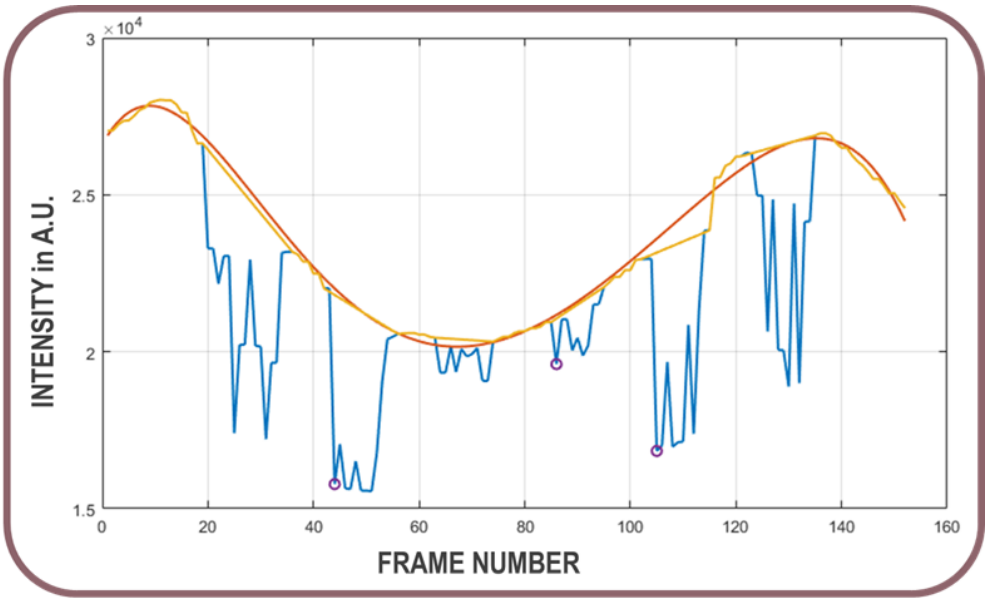

Figure 9.2: Videos are normalised to account for power fluctuations in the laser by summing over each frame and plotting the resulting spectrum (blue). Beginning and end frame of each of the six absorption blocks are selected manually (yellow). The off-resonant frames have a fifth-order polynomial fitted to them (orange) which is then used to normalise all frames. Shown here is a single scan of the intensity only video of the sixfold beam. Transitions used for later data analysis in figure 9.7 are indicated with purple circles.

the atomic spectrum can be monitored to minimise this transition. Alternatively, a radial beam will generate an azimuthally uniform longitudinal component, which can be used to view the π transition on the camera in order to make sure the absorption evenly affects the outside of the beam.

Some challenges in this process are that the beam is not a perfect Gaussian mode to begin with, and therefore the beam will not be azimuthally uniform in intensity after the q-plate. In such a case, even an azimuthal beam will carry a slight z-component. Additionally, in an early version of the cell holder, the cell was placed with its face orthogonal to the propagation axis. This caused it to act like a cavity, introducing unwanted resonances. To mitigate these effects, the current model of the cell holder has the cell sitting at a slight angle to the propagation axis. This, however, diverts the beam a slight amount, meaning if the beam is aligned with the first lens, and said first lens is aligned with the magnet, the propagation axis will be slightly shifted within the cell, and slightly off centre at the second lens. This effect can be minimised with hours of careful alignment and many tears. Time to take some data.

9.2 π transition as a function of radiality

IN WHICH I DRIVE ALL THREE TYPES OF ATOMIC DIPOLE TRANSITION IN THE FARADAY CONFIGURATION.

It was shown in chapter 3 that the longitudinal polarisation component is a function of the focusing angle and the radial component. Experimentally, the radial component is a function of the fast axis angle of the HWP before the q-plate. This suggests a linear relationship between the HWP angle and the strength of the longitudinal polarisation, or the depth of the π transition.

In order to verify this, a series of measurements was taken: the angle of the HWP before the q-plate varied from 0° to 90°. The HWP after was removed for this experiment. For each angle, the absorption spectrum was measured 10 times with a photodiode. The resulting oscilloscope traces were averaged for each angle, and plotted in figure 9.3. In this plot, it becomes visible that the depth of the transition depends on the radial component. This is the first ever published image of the π transition being driven in the Faraday configuration, and direct evidence for the existence of longitudinal polarisations.

In order to better visualise the linear dependence, a second set of traces for identical parameters was taken, but at a slightly higher temperature, $\approx 125^\circ$C. Figure 9.4 shows these spectra. All absorption dips have deepened, some even saturated. This higher contrast lends itself to an illustration of the linear relationship between the fraction of light intensity with radial polarisation prior to focusing and depth of the π transition, as seen in the inset. This is in line with the theoretical model described by Richards and Wolf.

However, it can not go without comment that in both figures, a small amount of the π transition remains even for fully azimuthal beams. This is likely due to the aforementioned intensity variation across the beam's spatial profile. An azimuthal intensity gradient is equivalent to a rotational assymetry in the beam, and therefore capable of generating a longitudinal component when focused. Nevertheless, the linear relationship between the initial polarisation and the absorbed longitudinal component

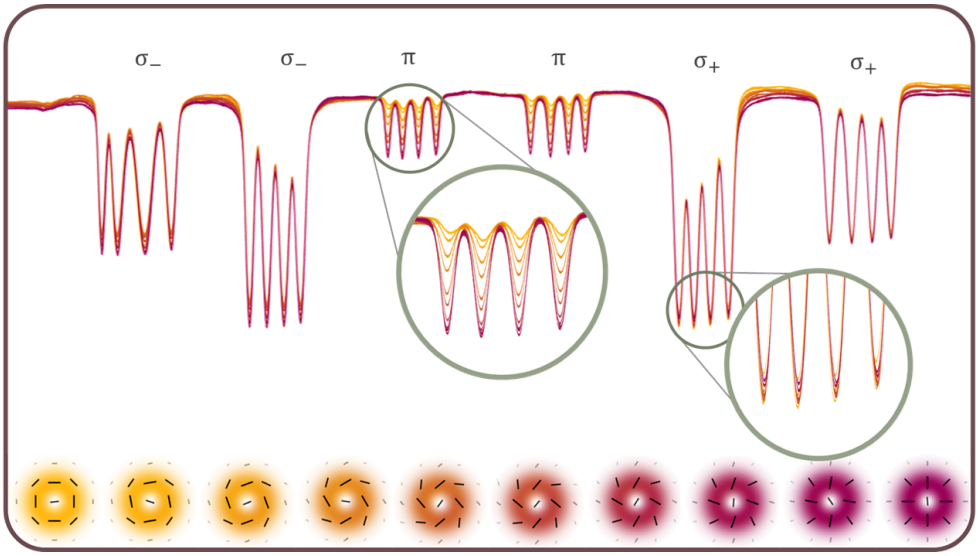

Figure 9.3: Experimentally measured absorption spectra measured with the photodiode after the atoms. The radial component of the input beam is varied using th HWP before the q-plate, changing the amplitude of the longitudinal polarisation component at the focus. The polarisation structures are indicated on the bottom of the figure. Radial beams in purple, azimuthal in yellow. The orientation of the line of each beam's centre is random, and an artifact of the simulation. Cell temperature $\approx$ 80°C

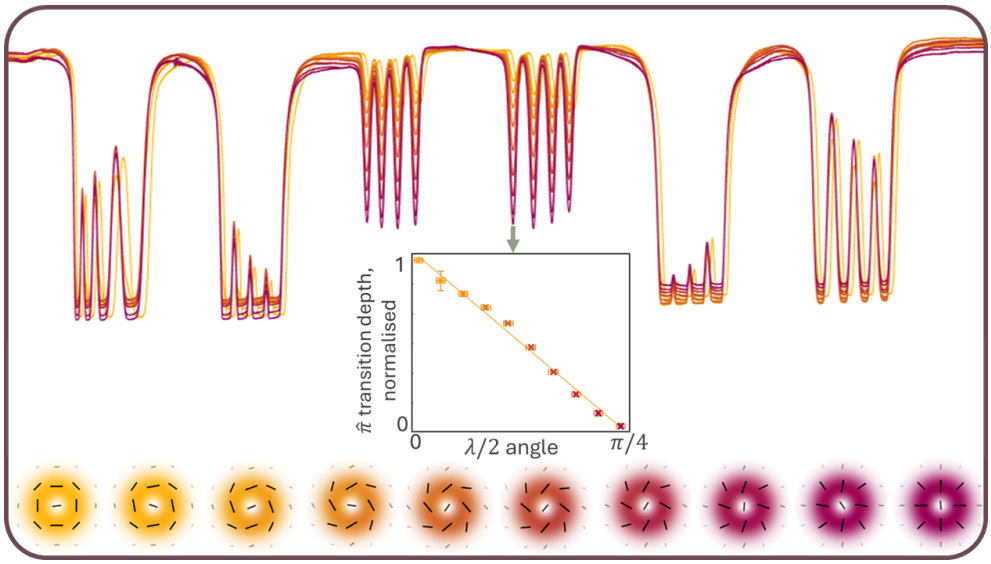

Figure 9.4: Experimentally measured absorption spectra measured with the photodiode after the atoms for the same selection of beams as figure 9.3. The inset shows the normalised depth of the π transition as a function of HWP angle. Cell temperature $\approx$125°C.

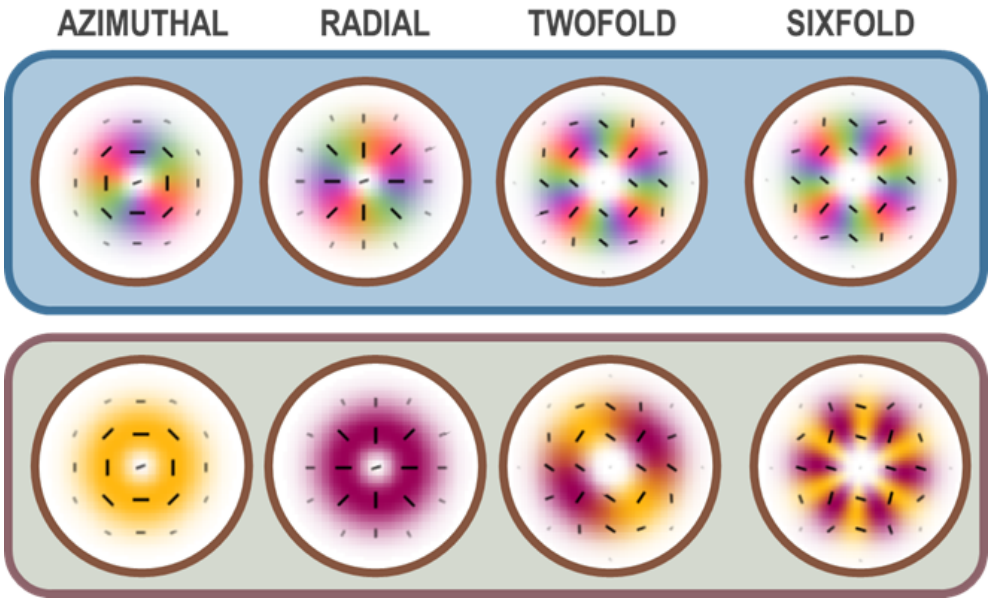

Figure 9.5: Comparison between the two colourmaps used in this chapter for the four beams that are spatially imaged. On the top is the Poincaré colour map from chapter 1.3.2, and on the bottom is an alternative colourmap that shows azimuthal polarisations in yellow and radial polarisations in purple. The twofold and sixfold beams generated by an m=2 q-plate have the same symmetry in the Cartesian Poincaré frame but a different symmetry in the polar radial-azimuthal basis - hence their names.

speaks for itself - the π transition is being driven by longitudinally polarised light.

9.3 spatially dependent longitudinal polarisation

IN WHICH BEAMS WITH THREE DIMENSIONAL POLARISATION STRUCTURES ARE GENERATED AND MEASURED BY YOURS TRULY

The beams used in the previous experiments have spatial dependence, but their radiality is azimuthally uniform. Beams can, however, feature spatially dependent radiality, which suggests that their longitudinal components, too, can be spatially structured. A m=2 q-plate generally produces a twofold beam (beam with twofold polarisation symmetry in the radial-azimuthal basis, see chapter 2) if the input polarisation is linear, and a HWP after it turns it into a sixfold beam. Under most circumstances, these beams would be considered to be very similar to one another, their trajectories on the Poincaré sphere are the same but in opposite direction. However, when considered in the radial-azimuthal basis as introduced in chapter 3.1, the cause of their names becomes apparent: the twofold beam cycles through radial and azimuthal polarisations twice, while the sixfold beam goes through the same process six times.

The symmetry of the beam will become three-dimensional when focused, and therefore translate to a spatial absorption pattern within the atoms. To investigate

this, the setup was switched to the camera configuration, and multiple scans were measured for each of the following beams: radial, azimuthal, twofold and sixfold. Figure 9.6 shows the unwrapped transmission patterns as a function of frequency scan. The $\sigma_{\pm}$ absorptions frame the data as constant, uninterrupted lines, but the π transitions show a much stronger dependence on the initial polarisation: They are uninterrupted for the radial beam, which is to be expected, and so is their (near) absence for an azimuthal beam. The aforementioned symmetries start to become apparent with the beams generated by the m=2 q-plate, there are two distinct patches of absorption for the twofold beam, and six for the sixfold.

Another tool introduced in chapter 8.1 is that of optical density. Being a measure of absorption, it lends itself to qualitative comparison between predicted polarisation components and experimentally determined spatial absorption patterns. Figure 9.7 shows just that - and the experimental data agrees with the prediction.

The data in figure 9.7 constitutes direct evidence of the exclusive absorption of longitudinally polarised light, something which has not been seen before in atomic spectra. For the first time, σ_{+}, σ_{-}, and π transitions have been recorded in the same spectrum for atoms in the Faraday configuration. This marks a milestone in optical techniques, and leaves us with a whole new set of questions to investigate. Like, how is the polarisation of the remaining beam affected by this?

9.4 the strong focusing faraday effect

WHICH CONTAINS UNPUBLISHED WORK TAKEN IN COLLABORATION WITH OUR COLLABORATORS AT DURHAM UNIVERSITY, AND PRELIMINARY ANALYSIS IN LINE WITH THE WORK BY ZHUJUN YE AND JOERG GOETTE.

Under the influence of a magnetic field, an atom's angular momentum sublevels shift, altering the detuning needed for $\sigma_{\pm}$ and π transitions. In chapter 5.2.2, the complex refractive index was revealed to be the underlying property that dictates both absorption and dispersion characteristics. As the absorption lines shift in frequency, so do the dispersion lines shift, allowing the atom to alter the polarisation. This causes the Faraday effect, which was introduced in chapter 6.1.

The Zeeman effect is the dominant feature of the HPB regime, its multiple adjacent transitions for the same circular polarisation cause the orientation of the polarisation ellipse to undergo a full rotation between each set of absorption dips. But how does this type of phase retardance affect longitudinally polarised light?

Polarimetry can be performed by the experimental setup in figure 9.1 by placing the optical components needed for Stokes measurements in front of the camera. As mentioned previously, the Wollaston prism projects orthogonal bases onto different areas of the camera while the wave plates are cycled through the three sets of unbiased bases, effectively halving the number of required measurements and making it easier for the videos to be synchronised in the analysis stage. So, in this type of measurement, three separate videos are obtained, each featuring two projections into orthogonal states in different areas of the camera. To synchronise the videos, the total intensity of each frame is calculated and plotted as spectra, using the scan cycle length of 304 frames. The start point of each video can now be adjusted, so that the absorption dips of the three videos line up.

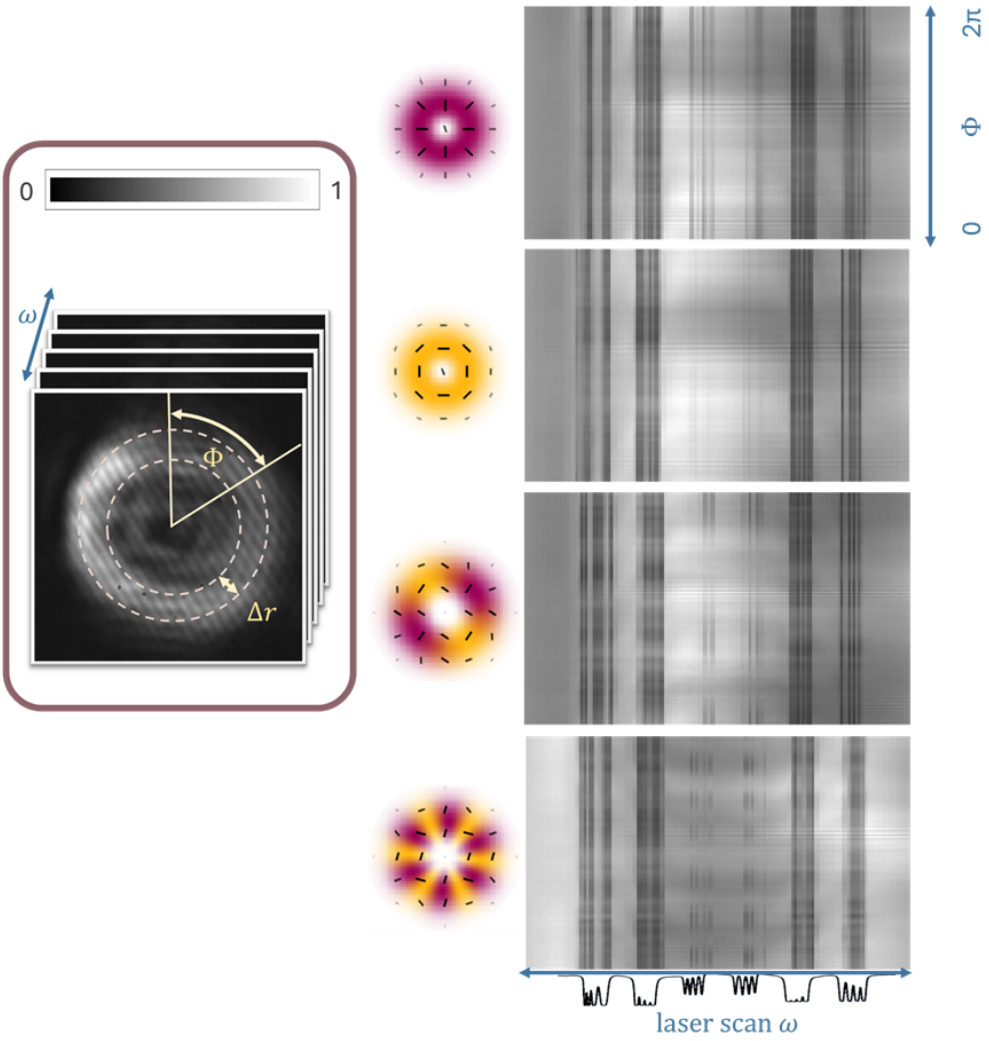

Figure 9.6: Unwrapped videos showing spatially dependent absorption. The horizontal axis is the scan, where each row corresponds to a frame. The vertical axis has the sum of the intensity of the beam at azimuthal angle φ in the frame in question. Note the spatially dependent absorption at the π transition in the twofold and sixfold beams, corresponding to the beam's symmetry.

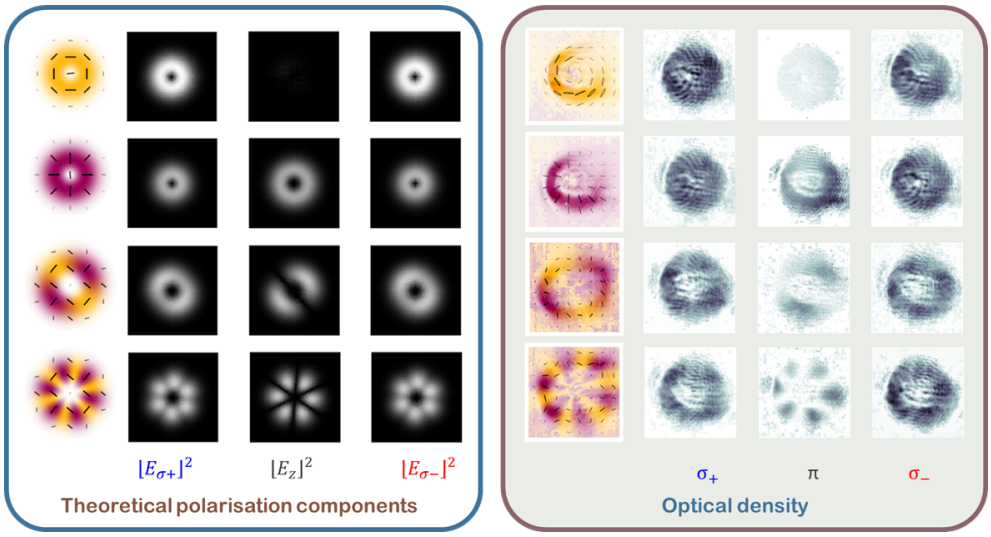

Figure 9.7: Optical density at different transitions in comparison to the polarisation components at the focus. Left: Simulated electric fields of right, longitudinal, and left polarisation components at the focus for azimuthal, radial, twofold and sixfold beams. Right: Experimentally obtained optical density at the σ_+, π, and σ_- transitions. The images have been normalised to the depth of absorption in the respective transition for a radial beam. The spatial distribution of both beams agrees with one another.

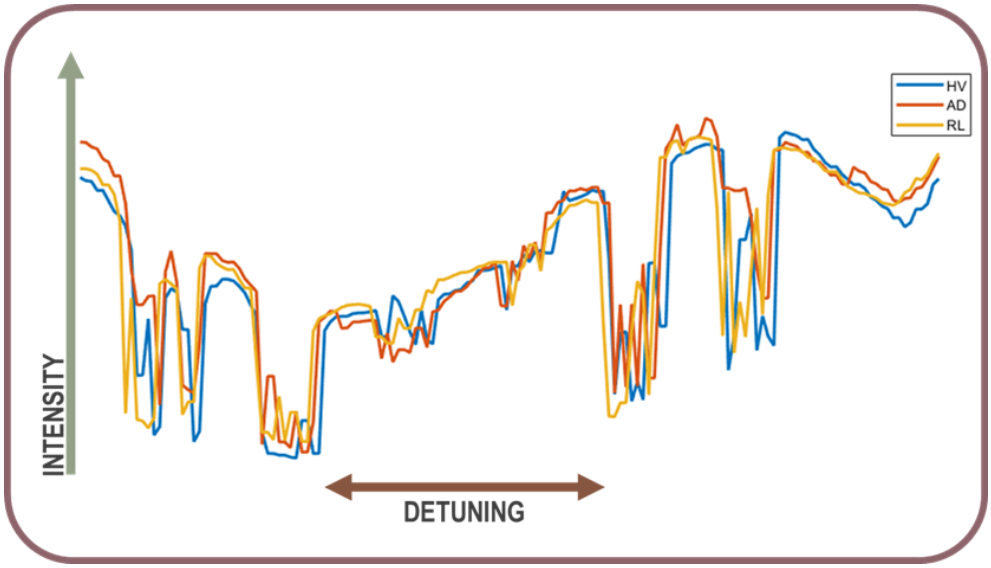

Figure 9.8: Spectra of synced videos, each measured in a different basis. Blue: HV, orange: AD, yellow: RL. The intensity is the sum of the intensity of each pixel for each frame of the video. Each video consists of multiple scans, so the start point can be adjusted so that all three videos have optimum overlap. Due to sampling error, the videos do not necessarily all feature the same transitions, this is also taken into consideration during synchronisation.

Figure 9.8 shows the spectra extracted from the videos. The signal generator that provides the triangle wave driving the laser has a lower frequency limit of 0.2 Hz, which means that for scans featuring the full spectrum a sampling error is introduced, and not all transitions are visible in each video. As each video features 2-4 scans, the frames used for later data analysis can be selected to feature the majority of the same absorption dips. Additionally, videos with a smaller scan range and hence higher spectral resolution were taken in regions of interest.

The next step in the analysis process is to crop and centre the images. As the orthogonal bases are on different areas of the screen, it is important to make sure that they perfectly overlap for later analysis. The relative centres are determined by calculating S_0 by overlapping the orthogonal bases in each of the three videos, and comparing the beam shape. If the overall intensity distribution for the unsplit beam is the same for all three, the relative centres have been found. To perfectly centre the crop of both beams, the beam is unwrapped for a range of centres. The optimal centre is chosen to be that where the radial intensity distribution is the sharpest.

The absolute centre is important here, as these beams, too, are unwrapped for analysis. A plot akin to that from figure 9.6 can be made from each of the videos, and from them, an unwrapped Stokes image for each specific detuning can be calculated.

Figure 9.9 shows the faraday rotation and polarisation dependent absorption of a sixfold beam as a function of frequency and azimuthal angle using the colourmap from chapter 1.3.2. It is visible that the σ_- transition is driven by right circularly polarised light, and the σ_+ transition is driven by left circularly polarised light. A full Faraday rotation is performed between each absorption dip. Note also that the direction of rotation is in opposite direction for σ_+

The π transition, however, behaves differently. On the right side of figure 9.9 are unwrapped plots for videos with reduced scan, so only a single block of transitions was covered. In the middle block, three such videos are stitched together, showing the area surrounding both π transitions. No Faraday rotations are observed, instead there seems to be a detuning dependence - all six areas of reduced intensity have a slight slant to them. This preliminary result warrants deeper investigation.

9.4.1 Faraday rotation as a function of focusing angle

One simplified way of thinking about strongly focused beams is as a field of local $\vec{k}$ vectors, all pointing towards the focus. Each of these vectors has a different direction, and therefore a different orientation to the magnetic field [185]. The further from the propagation axis, the stronger the tilt of the wavevector toward the focus. Due to this tilt, a mixture between Faraday and Voigt effects is seen locally. In other words, the Faraday rotation towards the outside of the beam is different from that near the inside. The data displayed in figure 9.9 was reanalysed to find initial evidence of this effect.

Figure 9.10 shows that the Faraday rotation angle depends on the beam radius. This data is early evidence to support Zhujun Ye's hypothesis [185], one of the many doors to future projects that have been opened due to the research in this thesis.

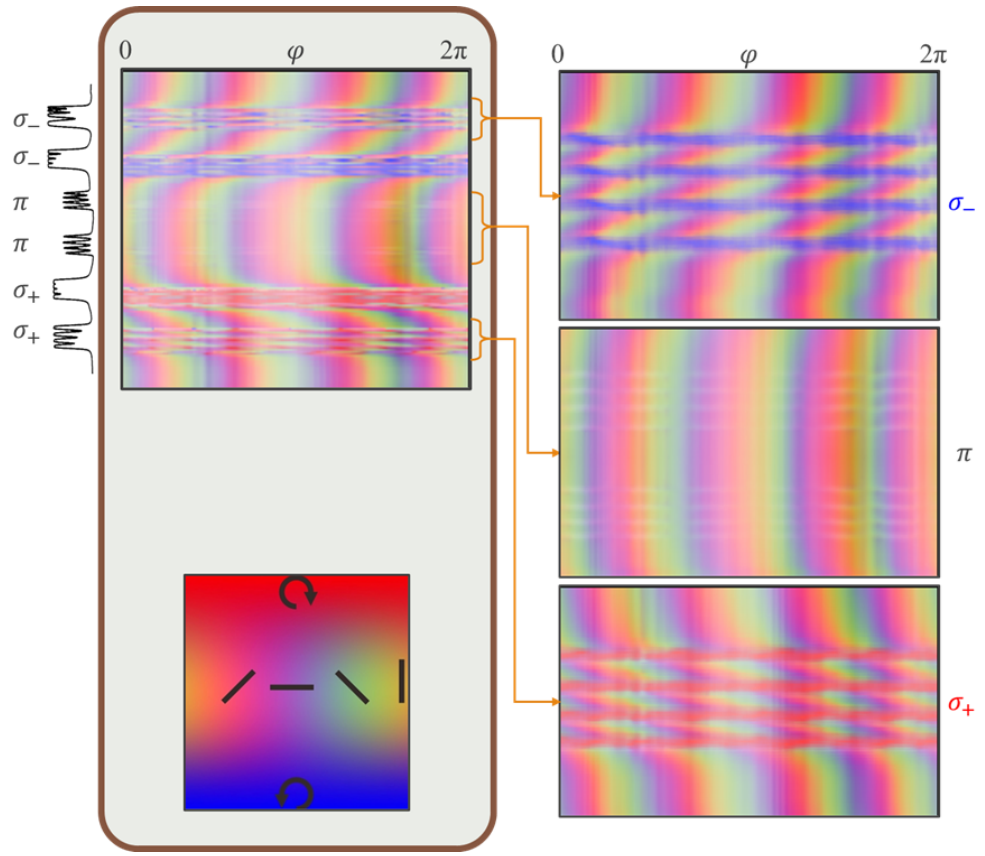

Figure 9.9: Experimental visualisation of Faraday rotation and dichroism in the hyperfine Paschen-Back regime for a sixfold beam. The vertical axis shows the laser scan, each row corresponds to a frame in the video. The horizontal axis sums radially over an area of the brightest region of the beam defined by the azimuthal angle ϕ. On the left is the full spectrum, but like all other data obtained with the camera it is susceptible to sampling bias. On the right are three videos with a smaller scan range showing (top to bottom) the outer σ_+ transition, both π transitions, and the outer σ_- transition. Between each absorption dip of the $\sigma_\pm$ transitions, the beam undergoes a full rotation. The π transition does not seem to have dispersive effects in the same way in this configuration.

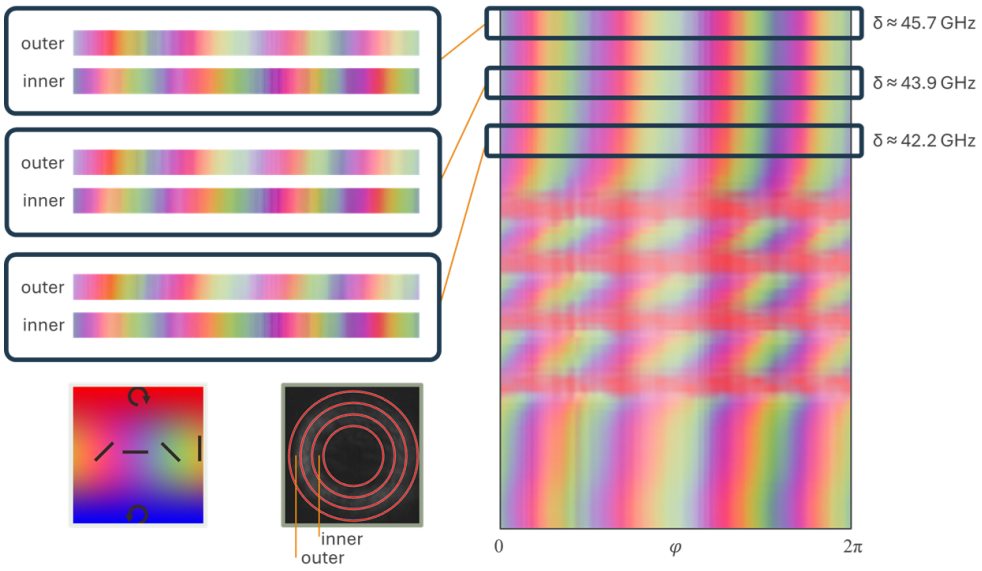

Figure 9.10: Faraday effect as a function of beam radius. The profile is split into three regions, as indicated by the rings at the bottom. On the right is a plot of the polarisation as a function of frequency and azimuthal angle near the "outer" block of sigma plus transitions. On the left are three snippets of the spectrum for the outer and inner circle only. It is visible that the Faraday rotation is stronger on the outside than the inside. Detunings are estimated by fitting the absorption curve to a theoretical spectrum, which assumes a linear scan.

conclusion of part III

In this chapter, two approaches to atom optics were discussed, each presenting a new way to measure electromagnetic effects. The cold atom experiment has a long and storied history and a high maintenance effort, but enables not only a novel way to measure magnetic field, but also makes it possible to measure optical concurrence in a single transmission image. The Durham experiment saw the first ever direct measurement of longitudinally polarised light. Both exploit the properties of the selection rules, and the influence of magnetic fields on the atom's internal states in order to measure otherwise elusive properties.

The cold atom experiment is a one-of-a-kind atomic state interferometer. In many ways, chapter 7.3 and 8 provide a complement to chapter 6, in the way that the experiment provided the inspiration for the new theoretical model and the new theoretical model makes it possible to conceptualise new measurements. As its four key parameters can be split into two groups - polarisation and magnetic field - the measurements in [12] and [1] each provide an insight into one of these parts. It was shown that the modulation of the fringes depends on the transverse component of the magnetic field as much as it does on the concurrence, and that information about the beam's structure can be read from the structure of the transmission pattern, as its alignment depends on the azimuthal angle of the magnetic field (and vice versa). The resulting spatially dependent state space not only depends on the concurrence of the beam, but is actively transferred by it. The insights into magnetism, too, have implications, but they are more practical. The Quantera V-Mag project aims to miniaturise the system in order to create a portable magnetometer using the SEIT effect for geomagnetic research.

Two optical tables over, the work uses magnetic fields that are much less commonly seen in nature (especially on this planet). Strongly focusing beams with a radial component creates light that is in part longitudinal. In the Faraday configuration, the π transition is often thought to be unavailable, as the driving polarisation cannot carry angular momentum. In chapter 9, we showed that longitudinally polarised light is capable of driving this transition, marking the first ever direct measurement of the longitudinal polarisation component.

As this effect has remained obscure for so long, much work is to be done still. Chapter 9.4.1 showed some preliminary investigations into the dispersive properties of the π transition in the Faraday configuration, and once this thesis is submitted, I will spend some more time in the lab, in order to gain more specific data.

Both experiments utilise the willingness of atoms to adjust to their surroundings in order to gain insight into the electromagnetic effects at play. Atoms provide a versatile interface between the classical and quantum worlds, both theoretically due to tools like semiclassical optics, and experimentally, due to their relative simplicity

(compared to other fundamental physics experiments). I am excited to see where both are going, and I hope that I will continue to be a part of this amazing research.

outlook

There are many options for further study and application for all four projects discussed in this thesis.

POVMs were shown to be well suited for the study of optically active samples, making it well suited for biomedical or chemical applications, where it is useful to monitor the optical effects of a sample in real time over long periods. The improved system lends itself to miniaturisation, and a modified interferometer could even be adapted to integrated optics. This would make it possible to have a standardised vector polarimeter conducting single frame measurements of Mueller matrices of any homogeneous system, even ones that are lossy or sensitive to high intensities.

The dressed state model and the cold atom experiment are inseperable at this point. The next step will likely feature the retaking of some preliminary data featuring beams with spatially varying χ, as well as refining the new model, and creating a reliable method for predicting the circumstances under which dark states form. Not only will it be conceptually interesting to investigate the patterns that lead to transparency, but it will also open the possibility of new measurements, which in turn will lead to new applications. As of writing, we are in the early stages of writing a paper about the partially dressed state model. Meanwhile, work has begun on a miniaturised version using warm atoms. The aim is to create a vector magnetometer to be used in geomagnetic observatories.

The strong focusing experiment was a success, and the paper will be submitted soon after this thesis. The next steps here are to investigate the strong focussing Faraday effect further by gathering data specifically suited to highlight the radially dependent rotation. Additionally, the strong focusing properties of other forms of vector or OAM beams have seen some theoretical investigation, which might be an interesting avenue of research.

conclusion

"ONCE YOU DO KNOW WHAT THE QUESTION ACTUALLY IS, YOU'LL KNOW WHAT THE ANSWER MEANS"
- DOUGLAS ADAMS

This thesis, like my PhD, has been quite a journey. If I have ever learned this much in this short a period in my life, it was before I learned to make permanent memories. The key theme of my work so far lies in the redefinition and specific choice of state spaces in order to reveal otherwise hidden structures. The basis dictates the effect.

Part I of this thesis was all about structured light. In the context of this thesis, light is mostly treated as a means to an end, so after introducing polarisation notations and eigenmodes of propagation and optical concurrence and longitudinal polarisation states, the focus was shifted to light matter interaction in order to measure optical elements. All optically active media can be described by a Mueller matrix, and Mueller matrices can be characterised via their effect on a known vector beam, and vector beams can be characterised in a single image using a modified Sagnac interferometer that performs POVMs on the beam. This method exploits an unusual basis to define the Poincaré sphere in fewer points, expediting the process.

The concept of such redefinitions of states is taken to its logical extreme in part II. Atomic state spaces are influenced by ambient electric and magnetic fields, and this influence can be boiled down into four parameters: The magnetic field inclination and azimuth, and the polarisation's ellipticity and orientation. As these parameters influence the splitting and hopping between the ground state of an atom in a Λ-configuration, they influence the symmetry of the state space itself. Under specific configurations of states, dark states are created, and spontaneous decay into these states renders the atom transparent to otherwise resonant light. In order for this effect to be visible in the theory, the model has to be moved into a dressed state picture capable of highlighting the interference between the atomic sublevels. The atom itself becomes an interferometer.

But this work is not purely theoretical: In part III, it is demonstrated that these effect are visible in experimentally measured absorption patterns, and in agreement with the theoretical model. Due to their optical dependence, trajectories on the Poincaré sphere can be mapped onto ultracold atoms, making it possible to measure optical concurrence in a single absorption image. But the sensing properties of atoms go even further - in the Faraday configuration, the angular momentum neutral π transition is normally considered unavailable, as paraxially polarised light is always co- or counter-rotating with the magnetic field. Longitudinally polarised light, how-

ever, is not. In the hyperfine Paschen-Back regime, the Zeeman shift exceeds the hyperfine splitting, and all available angular momentum transitions are separated in frequency space. This makes it easily measurable which transition is being driven. Using these effects, it was shown that the π transition can be driven in the Faraday configuration, but only if a longitudinal polarisation component is present. This marks the first ever direct measurement of the longitudinal polarisation component.

The full scope of the impact of the work here remains to be seen. Meanwhile, real-time Mueller matrix measurements are of interest for fields that study optically active samples (common in chemistry and biology), and a magnetometer using the atomic state interferometry is currently in development. As the theoretical model is still very young, some refinement is next in order. The paper needs to be finished and published, and we are currently looking to potentially find analytical solutions for the specific interplay between the terms. The study of longitudinal light, too, is only just beginning. There is more data than was possible to analyse on time for other effects, such as OAM beams, and there is more data to still be taken, especially regarding the strong focussing Faraday effect.

Meanwhile, this thesis is coming to an end. It has been shown in multiple different ways that sometimes science is about asking the right questions. A different perspective, a change in environment, a redefinition of state space might highlight a solution that is otherwise obscure. This has been shown to be true for light-matter interaction, but a dressed state model can be constructed in any state space. By now, it is well known that wave-particle duality is a nearly universal characteristic - depending on the reference frame, of course.

glossary of abbreviations and variables

I wanted to provide some reference for the colourmaps and abbreviations and variables I have used in this thesis. Here you go!

abbreviations

in order of appearance.

abbreviation	meaning
SAM	spin angular momentum
QWP	quarter wave plate
HWP	half wave plate
HG	Hermite Gaussian
LG	Laguerre Gaussian
OAM	orbital angular momentum
DMD	digital micromirror device
POVM	positive operator value measurement
PPBS	partially polarising beam splitter
PBS	polarising beam splitter
nPBS	non polarising beam splitter
Rb	rubidium
HPB	hyperfine Paschen-Back
MOT	magneto-optical trap
SpOT	spontaneous force dark optical trap
ECDL	external cavity diode laser
AOM	acousto-optical modulator
SLM	spatial light modulator
CCD	charge coupled device
SEIT	spatially dependent electromagnetically induced transparency
BEC	Bose-Einstein condensate
DFB	distributed feedback (laser)

variables

in order of appearance.

variable	meaning
$\vec{E}$	electric field
c	speed of light

t	time
$\vec{B}$	magnetic field
$\vec{r}$	distance
ϕ	generic phase
$\vec{k}$	wave vector
k	wave number
λ	wavelength
$\mathcal{I}$	intensity
$\vec{J}$	Jones vector
$\hat{J}$	Jones matrix
J_{ij}	Jones matrix element
θ	fast axis angle
χ	ellipticity of polarisation
ψ	orientation of polarisation
$\vec{S}$	Stokes vector
$S_{0,1,2,3}$	Stokes parameters
$\hat{M}$	Mueller matrix
M_{ij}	Mueller matrix element
u_+	left circular polarisation component
u_-	right circular polarisation component
∇^2	Laplace operator
k	eigenvalue
A	spatial wavefunction
w	beam waist
$\psi(z)$	Gouy phase
$R(z)$	Rayleigh range
m, n	Hermite polynomial orders
H_n	Hermite polynomial
$L_p^{\lvert\ell\rvert}$	Laguerre polynomial
ℓ	azimuthal LG integer
p	radial LG integer
h	Planck's constant
$\hbar$	reduced Planck's constant
ε	ellipticity of IG beam
m	topological charge
Ψ	generic wave function
ψ	generic sub wavefunction
φ	azimuthal angle on beam
s	distance from focus, or radius in spherical coordinates
g	polarisation unit vector
$\vec{a}$	vector amplitude
θ	polar angle (wave tilt)
$\hat{A}$	projection operator
λ_i	eigenvalue
$\lvert\lambda\rangle$	eigenstate
$\hat{\rho}$	density operator
ρ_{ij}	density matrix element
$\hat{P}_i$	projection operator

$P(\lambda_i)$	probability distribution
$\hat{P}_n$	projector into state n
$\hat{I}$	identity matrix
δ_{ij}	Kronecker delta
d	number of degrees of freedom
$\hat{\pi}$	POVM operator
a, b	POVM parameters
$\|\phi_{1,2,3,4}\rangle$	POVM states
Π	instrumentation matrix for converting POVM vector to Stokes
δ	phase retardance
n_o, n_e	ordinary and extraordinary refractive indexes
n	principal quantum number
l	electron orbital angular momentum
m_l	magnetic quantum number
s	electron spin
m_s	projection of spin
I	nuclear spin
m_I	projection of nuclear spin
j	electron angular momentum
m_j	projection of electron angular momentum
ω	angular frequency
a_0	atomic radius
n_L	refractive index
L	generic angular momentum
$g_l, g_I . g_s$	Landé g-factors
m_P	proton mass
m_e	electron mass
$\hat{H}$	Hamiltonian operator
Ω_L	Larmor frequency
e	fundamental charge
$\vec{\mu}$	Bohr magneton
$\vec{d}$	dipole moment
B_0	magnetic field magnitude
θ_B	polar magnetic field angle
ϕ_B	azimuthal magnetic field angle
N, M	normalisation factor
P	ellipticity
Q	linearity
$J, \bar{J}$	hopping rates
$E_{c,g,d}$	energy of ground state (relative to unshifted)
$\mathcal{J}_{cg,gd}$	hopping rates between states
γ	natural linewidth
$\hat{\Gamma}$	relaxation operator
$\hat{\Lambda}$	repopulation operator
N_g	number of ground states
v	velocity
m	diffraction order
$\mathcal{M}$	intensity pattern modulation

OD	optical density

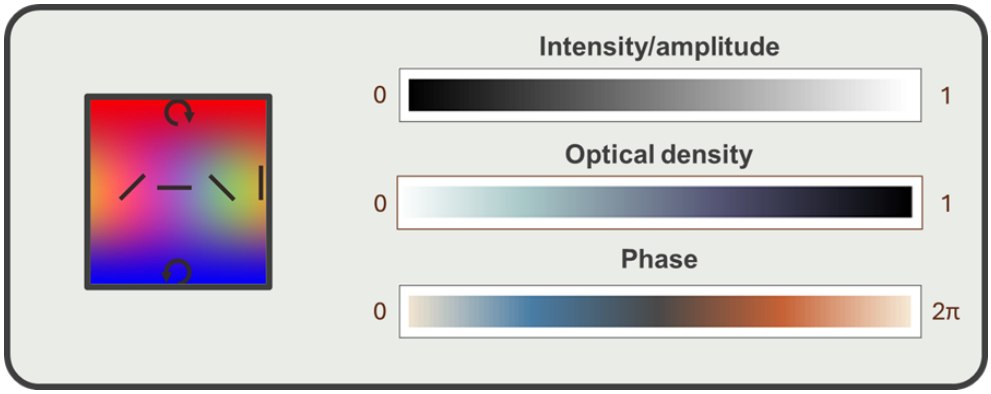

Figure 9.11: Colour maps used in this thesis. Left: Poincaré colour map for denoting polarisation. Right: Top: Greyscale colour map for intensity or electric field distribution, usually normalised. Middle: optical density colour map, always normalised. Bottom: Phase colour map for one full cycle

bibliography

1. Wang, J. *et al.* Measuring the Optical Concurrence of Vector Beams with an Atomic-State Interferometer. *Physical Review Letters* **132.** https://doi.org/10.1103/PhysRevLett.132.193803 (2024).
2. McWilliam, A., Khafaji, M. A. A., Svensson, S. J., Pádua, S. & Franke-Arnold, S. Dynamic Mueller matrix polarimetry using generalized measurements. *Optics Express* **32,** 21909. https://doi.org/10.1364/oe.521069 (2024).
3. Svensson, S. J., Higgins, C. R., Pizzey, D., Hughes, I. G. & Franke-Arnold, S. Visualizing strongly focused 3D light fields in an atomic vapor. *arXiv.* https://doi.org/10.48550/arXiv.2506.01680 (2025).
4. Franke-Arnold, S. Optical angular momentum and atoms. *Philosophical Transactions of the Royal Society A: Mathematical, Physical and Engineering Sciences* **375,** 20150435. https://doi.org/10.1098/rsta.2015.0435 (2017).
5. Richards, B. & Wolf, E. *Electromagnetic diffraction in optical systems I I. Structure of the image field in an aplanatic system* 1959. https://doi.org/10.1098/rspa.1959.0200.
6. Ludlow, A. D., Boyd, M. M., Ye, J., Peik, E. & Schmidt, P. O. Optical atomic clocks. *Rev. Mod. Phys.* **87,** 637–701. https://doi.org/10.1103/RevModPhys.87.637 (2015).
7. HosseiniArani, A. *et al.* Advances in Atom Interferometry and their Impacts on the Performance of Quantum Accelerometers On-board Future Satellite Gravity Missions. *Advances in Space Research* **74,** 3186–3200. https://doi.org/10.1016/j.asr.2024.06.055 (2024).
8. Fang, J. & Qin, J. Advances in Atomic Gyroscopes: A View from Inertial Navigation Applications. *Sensors* **12,** 6331–6346. https://doi.org/10.3390/s120506331 (2012).
9. Fang, J. *et al.* Classical and Atomic Gravimetry. *Remote Sensing* **16.** https://doi.org/10.3390/rs16142634 (2024).
10. Kitching, J., Knappe, S. & Donley, E. A. Atomic Sensors A Review. *IEEE Sensors Journal* **11,** 1749–1758. https://doi.org/10.1109/JSEN.2011.2157679 (2011).
11. Radwell, N., Clark, T. W., Piccirillo, B., Barnett, S. M. & Franke-Arnold, S. Spatially dependent electromagnetically induced transparency. *Physical Review Letters* **114.** https://doi.org/10.1103/PhysRevLett.114.123603 (2015).

12. Castellucci, F., Clark, T. W., Selyem, A., Wang, J. & Franke-Arnold, S. An atomic compass – detecting 3D magnetic field alignment with vector vortex light. *Physical Review Letters.* https://doi.org/10.1103/PhysRevLett.127.233202 (2021).

13. McWilliam, A. *et al.* Topological Approach of Characterizing Optical Skyrmions and Multi-Skyrmions. *Laser & Photonics Reviews* **17,** 2300155. https://doi.org/10.1002/lpor.202300155 (2023).

14. Selyem, A., Rosales-Guzmán, C., Croke, S., Forbes, A. & Franke-Arnold, S. Basis-independent tomography and nonseparability witnesses of pure complex vectorial light fields by Stokes projections. *Phys. Rev. A* **100,** 063842. https://doi.org/10.1103/PhysRevA.100.063842 (2019).

15. Swain, J. W. A History of Science: Ancient Science Through the Golden Age of Greece. By George Sarton. (Cambridge: Harvard University Press. 1952. Pp. xxvi, 646. $10.00.) *The American Historical Review* **58,** 585–586. https://doi.org/10.1086/ahr/58.3.585 (1953).

16. Hecht, E. *Optics Global Edition* 728. ISBN: 9781292096933. https://doi.org/ (Pearson Deutschland, 2016).

17. Mcwilliam, A. *Hidden structures within structured light Observing geometric phases and topologies for vector beams and their tomography* 2024. https://theses.gla.ac.uk/id/eprint/84594.

18. Simon, D. S. *A Guided Tour of Light Beams (Second Edition)* ISBN: 978-0-7503-3467-9. https://dx.doi.org/10.1088/978-0-7503-3467-9 (IOP Publishing, 2020).

19. Born, M. & Wolf, E. *Principles of Optics: 60th Anniversary Edition* 7th ed. ISBN: 9781108769914. https://doi.org/10.1017/9781108769914 (Cambridge University Press, 2019).

20. Crimin, F., Mackinnon, N., Götte, J. B. & Barnett, S. M. Optical Helicity and Chirality: Conservation and Sources. *Applied Sciences* **9.** https://doi.org/10.3390/app9050828 (2019).

21. Jones, R. C. A New Calculus for the Treatment of Optical SystemsI. Description and Discussion of the Calculus. *J. Opt. Soc. Am.* **31,** 488–493. https://doi.org/10.1364/JOSA.31.000488 (1941).

22. Kuan, W.-H., Lin, K.-H., Wang, C.-W. & Hung, N.-H. Generalized Jones Calculus for Vortex, Vector, and Vortex-Vector Beam Transformations. *arXiv.* https://doi.org/10.48550/arXiv.2103.13779 (2021).

23. SPIE. *Optipedia - free optics information from SPIE Publications* https://spie.org/publications/spie-publication-resources/optipedia-free-optics-information/fg05_p57-61_jones_matrix_calculus?SSO=1 (2025).

24. Marrucci, L., Manzo, C. & Paparo, D. Optical Spin-to-Orbital Angular Momentum Conversion in Inhomogeneous Anisotropic Media. *Phys. Rev. Lett.* **96,** 163905. https://doi.org/10.1103/PhysRevLett.96.163905 (2006).

25. Delaney, S., Sánchez-López, M. M., Moreno, I. & Davis, J. A. Arithmetic with q-plates. *Appl. Opt.* **56,** 596–600. https://doi.org/10.1364/AO.56.000596 (2017).

26. Poincaré, H. *Théorie mathématique de la lumiére II'* ISBN: 9781017642698 (Gauthier Villars, 1892).
27. Salazar-Ariza, K. & Torres, R. Trajectories on the Poincaré sphere of polarization states of a beam passing through a rotating linear retarder. *Journal of the Optical Society of America A* **35,** 65. https://doi.org/10.1364/josaa.35.000065 (2018).
28. Cisowski, C., Ross, C. & Franke-Arnold, S. Building Paraxial Optical Skyrmions Using Rational Maps. *Advanced Photonics Research,* 2200350. https://doi.org/10.1002/adpr.202200350 (2023).
29. McWilliam, A., Cisowski, C. M., Bennett, R. & Franke-Arnold, S. Angular momentum redirection phase of vector beams in a non-planar geometry. *Nanophotonics* **11,** 727–736. https://doi.org/10.1515/nanoph-2021-0528 (2022).
30. Stokes, G. G. in *Mathematical and Physical Papers* 233–258 (Cambridge University Press, 2009). https://doi.org/10.1017/CBO9780511702266.010.
31. Connect, F. *Mueller Matrices for Polarizing Elements* source:%20https://www.fiberoptics4sale.com/blogs/wave-optics/104730310-mueller-matrices-for-polarizing-elements (2025).
32. Rogovtsov, N. N. & Borovik, F. N. in *Light Scattering Reviews 4: Single Light Scattering and Radiative Transfer* (ed Kokhanovsky, A. A.) 347–429 (Springer Berlin Heidelberg, Berlin, Heidelberg, 2009). ISBN: 978-3-540-74276-0. https://doi.org/10.1007/978-3-540-74276-0_7.
33. Adams, C. S. & Hughes, I. G. *Optics f2f* ISBN: 9780191828980. https://doi.org/10.1093/oso/9780198786788.001.0001 (Oxford University PressOxford, 2018).
34. Saleh, B. E. A. & Teich, M. C. *Fundamentals of Photonics* https://doi.org/10.1002/0471213748 (Wiley, 1991).
35. Franke-Arnold, S. & Radwell, N. Light Served with a Twist. *Opt. Photon. News* **28,** 28–35. https://doi.org/10.1364/OPN.28.6.000028 (2017).
36. Allen, L., Beijersbergen, M. W., Spreeuw, R. J. C. & Woerdman, J. P. Orbital angular momentum of light and the transformation of Laguerre-Gaussian laser modes. *Phys. Rev. A* **45,** 8185–8189. https://doi.org/10.1103/PhysRevA.45.8185 (1992).
37. Franke-Arnold, S. 30 years of orbital angular momentum of light. *Nature Reviews Physics* **4.** https://doi.org/10.1038/s42254-022-00467-x (2022).
38. Durnin, J., Miceli, J. J. & Eberly, J. H. Diffraction-free beams. *Phys. Rev. Lett.* **58,** 1499–1501. https://doi.org/10.1103/PhysRevLett.58.1499 (1987).
39. Rosales-Guzmán, C., Ndagano, B. & Forbes, A. A review of complex vector light fields and their applications. *Journal of Optics* **20,** 123001. https://dx.doi.org/10.1088/2040-8986/aaeb7d (2018).
40. Beijersbergen, M., Allen, L., van der Veen, H. & Woerdman, J. Astigmatic laser mode converters and transfer of orbital angular momentum. *Optics Communications* **96,** 123–132. https://doi.org/10.1016/0030-4018(93)90535-D (1993).

41. Wang, J. *et al.* Exploring the ellipticity dependency on vector helical Ince-Gaussian beams and their focusing properties. *Optics Express* **30,** 24497. https://doi.org/10.1364/oe.462105 (2022).

42. Hawley, R. D. *Applications and practical considerations of polarisation structuring by a Fresnel cone* 2022. https://theses.gla.ac.uk/82650/.

43. Spreeuw, R. J. C. A Classical Analogy of Entanglement. *Foundations of Physics* **28.** https://doi.org/10.1023/A:1018703709245 (1998).

44. Hawley, R. D., Cork, J., Radwell, N. & Franke-Arnold, S. Passive broadband full Stokes polarimeter using a Fresnel cone. *Scientific Reports* **9.** https://doi.org/10.1038/s41598-019-39118-0 (2019).

45. Scheuer, J. Metasurfaces-based holography and beam shaping: engineering the phase profile of light. *Nanophotonics* **6,** 137–152. https://doi.org/10.1515/nanoph-2016-0109 (2017).

46. Dresel, T., Beyerlein, M. & Schwider, J. Design and fabrication of computer-generated beam-shaping holograms. *Appl. Opt.* **35,** 4615–4621. https://doi.org/10.1364/AO.35.004615 (1996).

47. Mitchell, K. J., Turtaev, S., Padgett, M. J., imár, T. & Phillips, D. B. High-speed spatial control of the intensity, phase and polarisation of vector beams using a digital micro-mirror device. *Opt. Express* **24,** 29269–29282. https://doi.org/10.1364/OE.24.029269 (2016).

48. Rosales-Guzmán, C. *et al.* Polarisation-insensitive generation of complex vector modes from a digital micromirror device. *Scientific Reports* **10,** 1–9. https://doi.org/10.1038/s41598-020-66799-9 (2020).

49. Selyem, A. *Three-dimensional Light Sculptures and their Interaction with Atomic Media: An experimentalist's guide* 2019. https://doi.org/10.5525/gla.thesis.74416.

50. Dada, A. C. *et al.* Optimal simultaneous measurements of incompatible observables of a single photon. *Optica* **6,** 257–263. https://doi.org/10.1364/OPTICA.6.000257 (2019).

51. Toninelli, E. *et al.* Concepts in quantum state tomography and classical implementation with intense light: a tutorial. *Adv. Opt. Photon.* **11,** 67–134. https://doi.org/10.1364/AOP.11.000067 (2019).

52. Petkovek, R., Petelin, J., Moina, J. & Bammer, F. Fast ellipsometric measurements based on a single crystal photo-elastic modulator. *Opt. Express* **18,** 21410–21418. https://doi.org/10.1364/OE.18.021410 (2010).

53. Zhang, S., Jiang, H., Gu, H., Chen, X. & Liu, S. High-speed Mueller matrix ellipsometer with microsecond temporal resolution. *Opt. Express* **28,** 10873–10887. https://doi.org/10.1364/OE.389825 (2020).

54. Dubreuil, M., Rivet, S., Jeune, B. L. & Cariou, J. Snapshot Mueller matrix polarimeter by wavelength polarization coding. *Opt. Express* **15,** 13660–13668. https://doi.org/10.1364/OE.15.013660 (2007).

55. Feng, Y. *et al.* Ultrafast Mueller matrix polarimetry with 10 nanosecond temporal resolution based on optical time-stretch. *Optics Letters* **47,** 1403. http://dx.doi.org/10.1364/OL.451766 (2022).

56. Zhang, J., Fan, F., Fu, W., Zeng, J. & Wang, J. Broadband real-time full-Stokes polarimetry by multi-tasking geometric phase element array. *Journal of Optics* **24,** 045801. https://dx.doi.org/10.1088/2040-8986/ac51b3 (2022).

57. He, J., Zhuang, J., Ding, L. & Huang, K. Optimization-free customization of optical tightly focused fields: uniform needles and hotspot chains. *Applied Optics* **60,** 3081. http://dx.doi.org/10.1364/AO.418415 (2021).

58. Ahmad, I., Khaliq, A., Iqbal, M. & Khan, S. Mueller matrix polarimetry for characterization of skin tissue samples: A review. *Photodiagnosis and Photodynamic Therapy* **30,** 101708. https://doi.org/10.1016/j.pdpdt.2020.101708 (2020).

59. Smith, M. H., Burke, P. D., Lompado, A., Tanner, E. A. & Hillman, L. W. *Mueller matrix imaging polarimetry in dermatology* in *Biomedical Diagnostic, Guidance, and Surgical-Assist Systems II* **3911** (SPIE, 2000), 210–216. https://doi.org/10.1117/12.384904.

60. Alali, S. & Vitkin, A. Polarized light imaging in biomedicine: emerging Mueller matrix methodologies for bulk tissue assessment. *Journal of Biomedical Optics* **20,** 061104. https://doi.org/10.1117/1.jbo.20.6.061104 (2015).

61. Fujiwara, H. *Spectroscopic ellipsometry: principles and applications* https://doi.org/10.1002/9780470060193 (John Wiley & Sons, 2007).

62. Suárez-Bermejo, J. C., González de Sande, J. C., Piquero, G., Failla, A. V. & Santarsiero, M. Full Poincaré Mueller Polarimetry Using a CCD Camera. *Photonics* **9,** 1–12. https://doi.org/10.3390/photonics9100702 (2022).

63. Prakash, O., Jachpure, D. & Vijaya, R. *Longitudinal Mode Control in Fiber Laser Ring Cavity Using Saturable Absorption in Erbium-Doped Fiber* in *2023 IEEE Workshop on Recent Advances in Photonics (WRAP)* (2023), 1–3. https://doi.org/10.1109/WRAP59682.2023.10712909.

64. Huang, K. *et al.* Vector-vortex BesselGauss beams and their tightly focusing properties. *Optics Letters* **36,** 888. http://dx.doi.org/10.1364/OL.36.000888 (2011).

65. Bauer, T. *et al.* Observation of optical polarization Möbius strips. *Science* **347,** 964–966. http://dx.doi.org/10.1126/science.1260635 (2015).

66. Maucher, F., Skupin, S., Gardiner, S. A. & Hughes, I. G. Creating Complex Optical Longitudinal Polarization Structures. *Physical Review Letters* **120.** http://dx.doi.org/10.1103/physrevlett.120.163903 (2018).

67. Otte, E. & Denz, C. Sculpting complex polarization singularity networks. *Optics Letters* **43,** 5821. http://dx.doi.org/10.1364/OL.43.005821 (2018).

68. Sugic, D. & Dennis, M. R. Singular knot bundle in light. *JOSA A* **35,** 1987–1999. https://doi.org/10.1364/JOSAA.35.001987 (2018).

69. Yang, Y., Yan, X., He, Y., Duan, H. & Li, L. Generating and converting special focal field patterns in a 4Pi focusing system illuminated by azimuthally polarized vortex beam. *Optical Review* **29,** 320–326. http://dx.doi.org/10.1007/s10043-022-00748-x (2022).

70. Dorn, R., Quabis, S. & Leuchs, G. Sharper focus for a radially polarized light beam. *Physical Review Letters* **91,** 233901. https://doi.org/10.1103/PhysRevLett.91.233901 (2003).

71. Chen, G., Wen, Z.-Q. & Qiu, C.-W. Superoscillation: from physics to optical applications. *Light: Science & Applications* **8.** http://dx.doi.org/10.1038/s41377-019-0163-9 (2019).

72. Kozawa, Y. & Sato, S. in *Progress in Optics* 35–90 (Elsevier, 2021). ISBN: 9780128246061. http://dx.doi.org/10.1016/bs.po.2021.01.001.

73. Wang, H., Shi, L., Lukyanchuk, B., Sheppard, C. & Chong, C. T. Creation of a needle of longitudinally polarized light in vacuum using binary optics. *Nature Photonics* **2,** 501–505. http://dx.doi.org/10.1038/nphoton.2008.127 (2008).

74. Forbes, K. A. & Green, D. Customized optical chirality of vortex structured light through state and degree-of-polarization control. *Physical Review A* **107.** http://dx.doi.org/10.1103/PhysRevA.107.063504 (2023).

75. Syubaev, S. A. *et al.* Plasmonic Nanolenses Produced by Cylindrical Vector Beam Printing for Sensing Applications. *Scientific Reports* **9.** http://dx.doi.org/10.1038/s41598-019-56077-8 (2019).

76. Hasegawa, S., Ichikawa, H. & Imura, K. Selective Excitation of Dark Plasmon Modes Using Cylindrical Vector Beams Studied by Microscopic Imaging of Nonlinear Photoluminescence. *The Journal of Physical Chemistry C* **128,** 2536–2542. https://doi.org/10.1021/acs.jpcc.3c07144 (2024).

77. Cui, Z., Sun, J., Litchinitser, N. M. & Han, Y. Dynamical characteristics of tightly focused vortex beams with different states of polarization. *Journal of Optics* **21,** 015401. http://dx.doi.org/10.1088/2040-8986/aaed91 (2018).

78. Andreev, A. V., Shoutova, O. A., Trushin, S. M. & Stremoukhov, S. Y. 3D Stokes parameters for vector focal fields. *Journal of the Optical Society of America B* **39,** 1775. http://dx.doi.org/10.1364/JOSAB.455841 (2022).

79. Martínez-Herrero, R. *et al.* Local characterization of the polarization state of 3D electromagnetic fields: an alternative approach. *Photonics Research* **11,** 1326. http://dx.doi.org/10.1364/%20PRJ.488703 (2023).

80. Aiello, A., Lindlein, N., Marquardt, C. & Leuchs, G. Transverse Angular Momentum and Geometric Spin Hall Effect of Light. *Physical Review Letters* **103.** http://dx.doi.org/10.1103/physrevlett.103.100401 (2009).

81. Neugebauer, M., Bauer, T., Aiello, A. & Banzer, P. Measuring the Transverse Spin Density of Light. *Physical Review Letters* **114.** http://dx.doi.org/10.1103/PhysRevLett.114.063901 (2015).

82. Man, Z., Xi, Z., Yuan, X., Burge, R. E. & Urbach, H. P. Dual Coaxial Longitudinal Polarization Vortex Structures. *Physical Review Letters* **124.** http://dx.doi.org/10.1103/PhysRevLett.124.103901 (2020).

83. Herrera, I. *et al.* Stokes-based analysis for the estimation of 3D dipolar emission. *Journal of the Optical Society of America. A Optics,* 41. https://hal.science/hal-04797187v1 (2024).

84. Youngworth, K. S. & Brown, T. G. Focusing of high numerical aperture cylindrical-vector beams. *Opt. Express* **7,** 77–87. https://doi.org/10.1364/OE.7.000077 (2000).

85. Krasavin, A. V. *et al.* Generalization of the optical theorem: experimental proof for radially polarized beams. *Light: Science amp; Applications* **7.** http://dx.doi.org/10.1038/s41377-018-0025-x (2018).

86. Novotny, L., Beversluis, M. R., Youngworth, K. S. & Brown, T. G. Longitudinal field modes probed by single molecules. *Physical Review Letters* **86,** 5251–5254. https://doi.org/10.1103/PhysRevLett.86.5251 (2001).

87. Lieb, M. A., Zavislan, J. M. & Novotny, L. Single-molecule orientations determined by direct emission pattern imaging. *Journal of the Optical Society of America B* **300,** 2530. https://doi.org/10.1364/JOSAB.21.001210 (2004).

88. Otte, E., Tekce, K., Lamping, S., Ravoo, B. J. & Denz, C. Polarization nanotomography of tightly focused light landscapes by self-assembled monolayers. *Nature Communications* **10.** http://dx.doi.org/10.1038/s41467-019-12127-3 (2019).

89. Bauer, T., Orlov, S., Peschel, U., Banzer, P. & Leuchs, G. Nanointerferometric amplitude and phase reconstruction of tightly focused vector beams. *Nature Photonics* **8,** 23–27. http://dx.doi.org/10.1038/nphoton.2013.289 (2013).

90. Ullah, K., Garcia-Camara, B., Habib, M., Yadav, N. & Liu, X. An indirect method of imaging the Stokes parameters of a submicron particle with sub-diffraction scattering. *Journal of Quantitative Spectroscopy and Radiative Transfer* **213,** 35–40. http://dx.doi.org/10.1016/j.jqsrt.2018.04.015 (2018).

91. Barnett, S. *Quantum Information* ISBN: 9780198527626. https://doi.org/10.1093/oso/9780198527626.001.0001 (Oxford University Press, 2009).

92. James, D. F. V., Kwiat, P. G., Munro, W. J. & White, A. G. Measurement of qubits. *Phys. Rev. A* **64,** 052312. https://doi.org/10.1103/PhysRevA.64.052312 (2001).

93. Von Neumann, J. & BEYER, R. T. *Mathematical Foundations of Quantum Mechanics: New Edition* NED - New edition. ISBN: 9780691178561. https://doi.org/10.2307/j.ctt1wq8zhp (Princeton University Press, 2018).

94. Rehacek, J., Englert, B.-G. & Kaszlikowski, D. Minimal qubit tomography. *Phys. Rev. A* **70,** 052321. https://doi.org/10.1103/PhysRevA.70.052321 (2004).

95. Bent, N. *et al.* Experimental Realization of Quantum Tomography of Photonic Qudits via Symmetric Informationally Complete Positive Operator-Valued Measures. *Phys. Rev. X* **5,** 041006. https://doi.org/10.1103/PhysRevX.5.041006 (2015).

96. Pimenta, W. M. *et al.* Minimum tomography of two entangled qutrits using local measurements of one-qutrit symmetric informationally complete positive operator-valued measure. *Phys. Rev. A* **88,** 012112. https://doi.org/10.1103/PhysRevA.88.012112 (2013).

97. Pimenta, W. M. *et al.* Minimal state tomography of spatial qubits using a spatial light modulator. *Opt. Express* **18,** 24423–24433. https://doi.org/10.1364/OE.18.024423 (2010).

98. Paiva-Sánchez, C., Burgos-Inostroza, E., Jiménez, O. & Delgado, A. Quantum tomography via equidistant states. *Phys. Rev. A* **82,** 032115. https://doi.org/10.1103/PhysRevA.82.032115 (2010).

99. Renes, J. M., Blume-Kohout, R., Scott, A. J. & Caves, C. M. Symmetric informationally complete quantum measurements. *Journal of Mathematical Physics* **45,** 2171–2180. https://doi.org/10.1063/1.1737053 (2004).

100. Al Khafaji, M. A. *et al.* Single-shot characterization of vector beams by generalized measurements. *Optics Express* **30,** 22396. https://doi.org/10.1364/oe.458352 (2022).

101. Ling, A., Soh, K. P., Lamas-Linares, A. & Kurtsiefer, C. Experimental polarization state tomography using optimal polarimeters. *Phys. Rev. A* **74,** 022309. https://doi.org/10.1103/PhysRevA.74.022309 (2006).

102. Ling, A., Soh, K. P., Lamas-Linares, A. & and, C. K. An optimal photon counting polarimeter. *Journal of Modern Optics* **53,** 1523–1528. https://doi.org/10.1080/09500340600674242 (2006).

103. Foot, C. J. *Atomic Physics* ISBN: 9780198506959. https://doi.org/10.1093/oso/9780198506959.001.0001 (Oxford University Press, 2004).

104. Cohen-Tannoudji, C. & Guéry-Odelin, D. *Advances in Atomic Physics* https://doi.org/10.1142/6631 (WORLD SCIENTIFIC, 2011).

105. Major, F. in *Atomic and Electron Physics* (eds Bederson, B. & Fite, W. L.) 1–28 (Academic Press, 1968). https://doi.org/10.1016/S0076-695X(08)60480-9.

106. Alzetta, G., Gozzini, A., Moi, L. & Orriols, G. An experimental method for the observation of r.f. transitions and laser beat resonances in oriented Na vapour. *Il Nuovo Cimento B.* https://doi.org/10.1007/BF02749417 (1976).

107. Bradley, C. C., Sackett, C. A. & Hulet, R. G. Bose-Einstein Condensation of Lithium: Observation of Limited Condensate Number. *Phys. Rev. Lett.* **78,** 985–989. https://doi.org/10.1103/PhysRevLett.78.985 (1997).

108. Akdeniz, Z., Vignolo, P. & Tosi, M. Bosonfermion demixing in a cloud of lithium atoms in a pancake trap. *Physics Letters A* **331,** 258–264. https://doi.org/10.1016/j.physleta.2004.08.054 (2004).

109. Zhu, Z., Gächter, M., Walter, A.-S., Viebahn, K. & Esslinger, T. Reversal of quantized Hall drifts at noninteracting and interacting topological boundaries. *Science* **384,** 317–320. https://doi.org/10.1126/science.adg3848 (2024).

110. Gomez, E., Orozco, L. A. & Sprouse, G. D. Spectroscopy with trapped francium: advances and perspectives for weak interaction studies. *Reports on Progress in Physics* **69,** 79. https://dx.doi.org/10.1088/0034-4885/69/1/R02 (2005).

111. BIPM. *SI base unit: second (s)* https://www.bipm.org/en/si-base-units/second.

112. Arnold, A. S., Garvie, C. S. & Riis, E. Large magnetic storage ring for Bose-Einstein condensates. *Physical review. A, Atomic, molecular, and optical physics* **73.** https://doi.org/10.1103/PhysRevA.73.041606 (2006).

113. Georgescu, I. 25 years of BEC. *Nature Reviews Physics.* https://doi.org/10.1038/s42254-020-0211-7 (2020).

114. Lemke, N. D. *et al.* Measurement of Optical Rubidium Clock Frequency Spanning 65 Days. *Sensors* **22.** https://doi.org/10.3390/s22051982 (2022).

115. Ebert, M., Kwon, M., Walker, T. G. & Saffman, M. Coherence and Rydberg Blockade of Atomic Ensemble Qubits. *Physical Review Letters* **115.** https://doi.org/10.1103/PhysRevLett.115.093601 (2015).

116. Budker, D. & Romalis, M. Optical magnetometry. *Nature Physics* **3.** https://doi.org/10.1038/nphys566 (2007).

117. Franke-Arnold, S. & Arnold, A. Twisting light to trap atoms. *American Scientist* **96,** 226–233. https://doi.org/10.1511/2008.71.226 (2008).

118. Wang, J. *et al.* Optically spatial information selection with hybridly polarized beam in atomic vapor. *Photonics Research* **6,** 451–456. https://doi.org/10.1364/PRJ.6.000451 (2018).

119. Norcia, M. A. *et al.* Frequency Measurements of Superradiance from the Strontium Clock Transition. *Phys. Rev. X* **8,** 021036. https://doi.org/10.1103/PhysRevX.8.021036 (2018).

120. Franzen, T. *et al.* Observation of magnetic Feshbach resonances between Cs and Yb 173. *Physical Review Research* **4.** https://doi.org/10.1103/PhysRevResearch.4.043072 (2022).

121. Steck, D. A. *Rubidium 87 D Line Data* 2001. http://steck.us/alkalidata,.

122. Higgins & Clare, R. *Durham E-Theses Quantum optics with 87Rb vapour in the hyperne Paschen-Back regime* http://etheses.dur.ac.uk/14829/http://etheses.dur.ac.uk.

123. Clark, T. W. *SCULPTING SHADOWS: On the Spatial Structuring of Fields Atoms: A Tale of Light and Darkness* 2016. https://theses.gla.ac.uk/id/eprint/8029.

124. Toll, J. S. Causality and the Dispersion Relation: Logical Foundations. *Phys. Rev.* **104,** 1760–1770. https://doi.org/10.1103/PhysRev.104.1760 (1956).

125. Perram, G. Blue and IR alkali lasers pumped by multiphoton absorption. *Spie Newsroom.* https://doi.org/10.1117/2.1201002.002558 (2010).

126. Cohen-Tannoudji, C., Diu, B. & Laloë, F. *Quantum mechanics; 1st ed.* Trans. of : Mécanique quantique. Paris : Hermann, 1973. https://cds.cern.ch/record/101367 (Wiley, New York, NY, 1977).

127. Schmiegelow, C. T. *et al.* Transfer of optical orbital angular momentum to a bound electron. *Nature Communications* **7,** 1–6. https://doi.org/10.1038/ncomms12998 (2016).

128. Westerberg, N., Svensson, S. J. & Franke-Arnold, S. *Cold Atom theory meeting* Private conversation. 2024.

129. Faraday, M. I. Experimental researches in electricity.Nineteenth series. *Phil. Trans. R. Soc. L.,* 1–20. https://doi.org/10.1098/rstl.1846.0001 (1846).

130. Trénec, G., Volondat, W., Cugat, O. & Vigué, J. Permanent magnets for Faraday rotators inspired by the design of the magic sphere. *Applied optics* **50,** 4788–4797. https://doi.org/10.1364/AO.50.004788 (2011).

131. Yang, X. *et al.* An inverse Faraday effect generated by linearly polarized light through a plasmonic nano-antenna. *Nanophotonics* **12,** 687–694. https://doi.org/10.1515/nanoph-2022-0488 (2023).

132. Happer, W. & Mathur, B. S. Off-Resonant Light as a Probe of Optically Pumped Alkali Vapors. *Phys. Rev. Lett.* **18,** 577–580. https://doi.org/10.1103/PhysRevLett.18.577 (1967).

133. Zhang, L. *et al.* A review on magneto-optical ceramics for Faraday isolators. *Journal of Advanced Ceramics* **12,** 873–915. https://doi.org/10.26599/JAC.2023.9220742 (2023).

134. Trénec, G., Volondat, W., Cugat, O. & Vigué, J. Permanent magnets for Faraday rotators inspired by the design of the magic sphere. *Appl. Opt.* **50,** 4788–4797. https://doi.org/10.1364/AO.50.004788 (2011).

135. Kiefer, W., Löw, R., Wrachtrup, J. & Gerhardt, I. Na-Faraday rotation filtering: The optimal point. *Scientific Reports* **4,** 2045–2322. https://doi.org/10.1038/srep06552 (2014).

136. Dawes, A. M. C., Illing, L., Greenberg, J. A. & Gauthier, D. J. All-optical switching with transverse optical patterns. *Phys. Rev. A* **77,** 013833. https://doi.org/10.1103/PhysRevA.77.013833 (2008).

137. Siddons, P., Adams, C. S. & Hughes, I. G. Optical control of Faraday rotation in hot Rb vapor. *Phys. Rev. A* **81,** 043838. https://doi.org/10.1103/PhysRevA.81.043838 (2010).

138. Abel, R. P., Krohn, U., Siddons, P., Hughes, I. G. & Adams, C. S. Faraday dichroic beam splitter for Raman light using an isotopically pure alkali-metal-vapor cell. *Opt. Lett.* **34,** 3071–3073. https://doi.org/10.1364/OL.34.003071 (2009).

139. Budker, D., Kimball, D., Rochester, S., Yashchuk, V. & Zolotorev, M. Sensitive magnetometry based on nonlinear magneto-optical rotation. *Physical Review A* **62,** 043403. https://doi.org/10.1103/PhysRevA.62.043403 (2000).

140. Marchant, A. L. *et al.* Off-resonance laser frequency stabilization using the Faraday effect. *Opt. Lett.* **36,** 64–66. https://doi.org/10.1364/OL.36.000064 (2011).

141. Zentile, M. A. *et al.* The hyperfine Paschen-Back Faraday effect. *Journal of Physics B: Atomic, Molecular and Optical Physics* **47.** https://doi.org/10.1088/0953-4075/47/7/075005 (2014).

142. Higgins, C., Pizzey, D. & Hughes, I. Fine-structure changing collisions in Rb upon D2 excitation in the hyperfine Paschen-Back regime. *Journal of Physics B: Atomic, Molecular and Optical Physics* **57.** https://doi.org/10.1088/1361-6455/ad8ab0 (2024).

143. Griffiths, D. J. & Schroeter, D. F. *Introduction to Quantum Mechanics* 3rd ed. ISBN: 9781107189638. https://doi.org/10.1017/9781316995433 (Cambridge University Press, 2018).

144. Stenholm, S. *Foundations of Laser Spectroscopy* ISBN: 9780486150376 (Dover Publications, 2012).

145. Budker, D. *et al.* Resonant nonlinear magneto-optical effects in atoms. *Reviews of Modern Physics* **74,** 1153. https://doi.org/10.1103/RevModPhys.74.1153 (2002).

146. Cohen, I. B. *The Newtonian Revolution* https://doi.org/10.1017/CBO9780511665370 (Cambridge University Press, 1981).

147. Vernier, A. *Phase Dependent Atom Optics* 2011. https://theses.gla.ac.uk/id/eprint/2560.

148. Grumbling, E. & Horowitz, M. in, 212–225 (2019). https://doi.org/10.17226/25196.

149. Saywell, J. C. *et al.* Enhancing the sensitivity of atom-interferometric inertial sensors using robust control. *Nature Communications* **14.** https://doi.org/10.1038/s41467-023-43374-0 (2023).

150. Wu, S., Su, E. & Prentiss, M. Demonstration of an Area-Enclosing Guided-Atom Interferometer for Rotation Sensing. *Phys. Rev. Lett.* **99,** 173201. https://doi.org/10.1103/PhysRevLett.99.173201 (2007).

151. Debs, J. E. *et al.* Cold-atom gravimetry with a Bose-Einstein condensate. *Phys. Rev. A* **84,** 033610. https://doi.org/10.1103/PhysRevA.84.033610 (2011).

152. Ghosh, S., Graham, E., Getz, S., Giman, A. & Maruyama, R. *Advancing Rydberg atom-based axion detection* in *Quantum Sensing, Imaging, and Precision Metrology II* (eds Scheuer, J. & Shahriar, S. M.) **12912** (SPIE, 2024), 129120E. https://doi.org/10.1117/12.3012355.

153. Of Chemistry, R. S. *Periodic Table: Rubidium* https://www.rsc.org/periodic-table/element/37/rubidium.

154. Balabas, M. V. *et al.* High quality anti-relaxation coating material for alkali atom vapor cells. *Opt. Express* **18,** 5825–5830. https://doi.org/10.1364/OE.18.005825 (2010).

155. Garraway, B. M. & Minogin, V. G. Theory of an optical dipole trap for cold atoms. *Physical Review A* **62.** https://doi.org/10.1103/PhysRevA.62.043406 (2000).

156. Pagano, A., Jaschke, D., Weiss, W. & Montangero, S. Optimal control transport of neutral atoms in optical tweezers at finite temperature. *Phys. Rev. Res.* **6,** 033282. https://doi.org/10.1103/PhysRevResearch.6.033282 (2024).

157. Xie, W. *et al.* A cold cesium beam source based on a two-dimensional magneto-optical trap. *AIP Advances* **12,** 075124. https://doi.org/10.1063/5.0099415 (2022).

158. Bordé, C. J. Atomic clocks and inertial sensors. *Metrologia* **39,** 435. https://dx.doi.org/10.1088/0026-1394/39/5/5 (2002).

159. Wildermuth, S. *et al.* Sensing electric and magnetic fields with Bose-Einstein condensates. *Applied Physics Letters* **88,** 264103. https://doi.org/10.1063/1.2216932 (2006).

160. Nshii, C. C. *et al.* A surface-patterned chip as a strong source of ultracold atoms for quantum technologies. *Nature Nanotechnology* **8.** https://doi.org/10.1038/nnano.2013.47 (2013).

161. Radwell, N., Walker, G. & Franke-Arnold, S. Cold-atom densities of more than 1012 cm-3 in a holographically shaped dark spontaneous-force optical trap. *Physical Review A - Atomic, Molecular, and Optical Physics* **88.** https://doi.org/10.1103/PhysRevA.88.043409 (2013).

162. Ramakrishna, S. *et al.* Interaction of vector light beams with atoms exposed to a time-dependent magnetic field. *Phys. Rev. A.* https://doi.org/10.1103/PhysRevA.110.043101 (2024).

163. Arnold, A. S., Wilson, J. S. & Boshier, M. G. A simple extended-cavity diode laser. *Review of Scientific Instruments* **69,** 1236–1239. https://doi.org/10.1063/1.1148756 (1998).

164. Castellucci, F. *Novel applications of structured light in the field of atom optics. Imagining optical magnetometry with images* 2022. https://theses.gla.ac.uk/id/eprint/82732.

165. Budker, D. & Romalis, M. Optical magnetometry. *Nature Physics* **3,** 227–234. https://doi.org/10.1038/nphys566 (2007).

166. Thiele, T., Lin, Y., Brown, M. O. & Regal, C. A. Self-calibrating vector atomic magnetometry through microwave polarization reconstruction. *Physical Review Letters* **121,** 153202. https://doi.org/10.1103/PhysRevLett.121.153202 (2018).

167. Affolderbach, C., Stähler, M., Knappe, S. & Wynands, R. An all-optical, high-sensitivity magnetic gradiometer. *Applied Physics B* **75,** 605–612. https://doi.org/10.1007/s00340-002-0959-8 (2002).

168. Smith, A., Anderson, B. E., Chaudhury, S. & Jessen, P. S. Three-axis measurement and cancellation of background magnetic fields to less than 50 μG in a cold atom experiment. *Journal of Physics B: Atomic, Molecular and Optical Physics* **44,** 205002. https://doi.org/10.1088/0953-4075/44/20/205002 (2011).

169. Kominis, I., Kornack, T., Allred, J. & Romalis, M. V. A subfemtotesla multichannel atomic magnetometer. *Nature* **422,** 596–599. https://doi.org/10.1038/nature01484 (2003).

170. Pyragius, T., Florez, H. M. & Fernholz, T. Voigt-effect-based three-dimensional vector magnetometer. *Physical Review A* **100,** 023416. https://doi.org/10.1103/PhysRevA.100.023416 (2019).

171. Patton, B., Zhivun, E., Hovde, D. & Budker, D. All-optical vector atomic magnetometer. *Physical Review Letters* **113,** 013001. https://doi.org/10.1103/PhysRevLett.113.013001 (2014).

172. Wang, T. *et al.* Pulsed vector atomic magnetometer using an alternating fast-rotating field. *Nature Communications* **16.** https://doi.org/10.1038/s41467-025-56668-2 (2025).

173. Lenci, L. *et al.* Vectorial atomic magnetometer based on coherent transients of laser absorption in Rb vapor. *Physical Review A* **89,** 043836. https://doi.org/10.1103/PhysRevA.89.043836 (2014).

174. Ingleby, S. J., O'Dwyer, C., Griffin, P. F., Arnold, A. S. & Riis, E. Vector Magnetometry Exploiting Phase-Geometry Effects in a Double-Resonance Alignment Magnetometer. *Physical Review Applied* **10.** https://doi.org/10.1103/physrevapplied.10.034035 (2018).

175. Yudin, V. *et al.* Vector magnetometry based on electromagnetically induced transparency in linearly polarized light. *Physical Review A* **82,** 033807. https://doi.org/10.1103/PhysRevA.82.033807 (2010).

176. Qiu, S. *et al.* Visualization of magnetic fields with cylindrical vector beams in a warm atomic vapor. *Photonics Research* **9,** 2325–2331. https://doi.org/10.1364/PRJ.418522 (2021).

177. Zhang, D. *et al.* Ground-state phase diagram of a spin-orbital-angular-momentum coupled Bose-Einstein condensate. *Physical Review Letters* **122,** 110402. https://doi.org/10.1103/PhysRevLett.122.110402 (2019).

178. Henderson, G. W., Robb, G. R. M., Oppo, G.-L. & Yao, A. M. Control of light-atom solitons and atomic transport by optical vortex beams propagating through a Bose-Einstein Condensate. *Physical Review Letters* **129,** 073902. https://doi.org/10.1103/PhysRevLett.129.073902 (2022).

179. Li, J.-Z. *et al.* Synthetic Topological Vacua of Yang-Mills Fields in Bose-Einstein Condensates. *Physical Review Letters* **129,** 220402. https://doi.org/10.1103/PhysRevLett.129.220402 (2022).

180. Torgerson, J. R., Schauer, M. M., Lamoreaux, S. K. & Gleyzes, S. Single-ion magnetic compass. *JOSA B* **22,** 72–76. https://doi.org/10.1364/JOSAB.22.000072 (2005).

181. Stopp, F. *et al.* Coherent Transfer of Transverse Optical Momentum to the Motion of a Single Trapped Ion. *Physical Review Letters* **129,** 263603. https://doi.org/10.1103/PhysRevLett.129.263603 (2022).

182. Ye, L., Yang, L., Zheng, X. & Mukamel, S. Enhancing circular dichroism signals with vector beams. *Physical Review Letters* **126,** 123001. https://doi.org/10.1103/PhysRevLett.126.123001 (2021).

183. Zhang, Y. *et al.* Theoretical investigation on asymmetrical spinning and orbiting motions of particles in a tightly focused power-exponent azimuthal-variant vector field. *Optics Express* **26,** 4318. http://dx.doi.org/10.1364/oe.26.004318 (2018).

184. Sargsyan, A., Momier, R., Leroy, C. & Sarkisyan, D. Saturated absorption technique used in potassium microcells for magnetic field sensing. *Laser Physics* **32,** 105701. https://doi.org/10.1088/1555-6611/ac8c42 (2022).

185. Ye, Z. *Optical Skyrmions andPolarizations of Highly FocusedStructured Light* unpublished thesis.